

THE UNIVERSITY OF CALGARY

PETROLOGY OF NEPHELINITES AND ASSOCIATED ULTRAMAFIC
NODULES OF VOLCANO MOUNTAIN, YUKON TERRITORY

by

Sabrina Trupia

A THESIS SUBMITTED TO THE FACULTY OF GRADUATE STUDIES IN
PARTIAL FULFILLMENT OF THE REQUIREMENTS FOR THE
DEGREE OF MASTER OF SCIENCE

DEPARTMENT OF GEOLOGY AND GEOPHYSICS

CALGARY, ALBERTA

APRIL, 1992

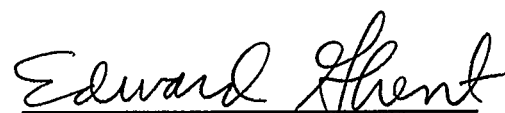
© Sabrina Trupia 1992

THE UNIVERSITY OF CALGARY
FACULTY OF GRADUATE STUDIES

The undersigned certify that they have read, and recommend to the Faculty of Graduate Studies for acceptance, a thesis entitled "Petrology of nephelinites and associated ultramafic nodules of Volcano Mountain, Yukon Territory" submitted by Sabrina Trupia, in partial fulfillment of the requirements for the degree of Master of Science.



Supervisor,
Dr. J.W. Nicholls
Geology and Geophysics



Dr. E.D. Ghent
Geology and Geophysics



Dr. T.M. Gordon
Geology and Geophysics



Dr. W.G. Laidlaw
Chemistry

April 24, 1992.

ABSTRACT

Nephelinites from Volcano Mountain, Yukon Territory, contain olivine, Ti-rich diopside, ulvöspinel, nepheline, leucite, traces of calcite, and residual glass with varying compositions. Mass balance calculations suggest that these compositional differences are due to different fractionation paths; a conclusion consistent with the observed mineral abundances near the glasses. Pearce Element Ratios show that at least one of the lava flows sampled is not comagmatic with the others.

Thermodynamic modeling of silicate melts and textural observations indicate that the pressure-temperature path of fractionation was polybaric, and that the minimum depth of melt separation from the source rocks was 60 km.

The volcanic rocks host dunite and lherzolite nodules consisting of diopside and hypersthene, olivine and chromian spinel. Deformation textures and mineral compositions are different from other occurrences in western North America.

Geothermometry on the xenoliths provide temperature estimates between 930°C and 1350°C. The range of equilibrium pressures for the nodules is estimated from phase equilibria at 20 to 45 kilobars.

ACKNOWLEDGEMENTS

My first thanks are to Jim Nicholls, the best of all possible supervisors, for teaching me how to be a good scientist, for providing continuing support (moral and material) through all stages of my thesis, and for the chemical analyses.

I also wish to thank the people who helped me in this study: Mavis Stout and John Machachek, for advice on collecting probe data and for being extremely patient when I messed up; Andrea Harris for the indefatigable assistance in the field; and the members of my defense committee, Drs. Ed Ghent, Terry Gordon and Bill Laidlaw, for reminding me that this thesis is only a starting point.

Last but not least, thanks to you all fifth floor weasels for keeping me sane (albeit a bit cranky) with incessant and mindless banter (and you guys thought you would not be in the acknowledgements....).

TABLE OF CONTENTS

APPROVAL PAGE	ii
ABSTRACT	iii
ACKNOWLEDGEMENTS	iv
TABLE OF CONTENTS	v
LIST OF TABLES	viii
LIST OF FIGURES	x
LIST OF PLATES	xii
SECTION 1	1
1.1 Objectives	1
1.2 Geologic setting	2
SECTION 2	11
2.1. PETROGRAPHY	11
2.1.1. Host lavas	11
2.1.2 Ultramafic xenoliths	16
2.2 MINERALOGY	18
2.2.1 Host lavas	23
OLIVINE	23
PYROXENE	23
NEPHELINE	28
LEUCITE	30
OXIDES	33
RESIDUAL GLASS	33
2.2.2 Xenoliths	43
OLIVINE	43

PYROXENE	43
SPINEL	44
SECTION 3	59
3.1 P-T CONDITIONS AND PHASE EQUILIBRIA OF ULTRAMAFIC XENOLITHS	59
3.1.1 Thermometry	59
3.1.2. Phase equilibria	64
3.2 CLASSIFICATION AND COMPARISON OF ULTRAMAFIC XENOLITHS	65
3.2.1 Textural comparison	66
3.2.2 Compositional comparison	68
3.2.3 Discussion.	70
SECTION 4	72
4.1 CLASSIFICATION OF VOLCANO MOUNTAIN LAVAS ...	72
4.2 CHEMICAL VARIATION OF LAVAS AND RESIDUAL GLASSES: PEARCE ELEMENT RATIOS.	77
4.2.1 Introduction	77
4.2.2 Whole rock plots.	81
4.2.3 Residual glass plots.	85
4.1.3. Discussion	88
SECTION 5	90
INTRODUCTION	90
5.1 CRYSTALLIZATION HISTORY OF VOLCANO MOUNTAIN LAVAS	91
5.1.2. Crystal fractionation	91
5.1.3 Liquid lines of descent	95
5.1.4 P-T paths.	98
5.2 DEPTH OF MELT SEPARATION	106

SECTION 6 109
 6.1 CONCLUSIONS 109

REFERENCES CITED 111

APPENDIX A 123

LIST OF TABLES

Table 2.1	Modal composition of nephelinites	13
Table 2.2	Modal composition of ultramafic xenoliths	13
Table 2.3	Average microprobe analyses of olivine in nephelinites	19
Table 2.4	Average microprobe analyses of pyroxene in nephelinites	24
Table 2.5	Average microprobe analyses of nepheline in nephelinites	31
Table 2.6	Average microprobe analyses of leucite in nephelinites	32
Table 2.7	Averaged microprobe analyses of ulvospinel/magnetite in nephelinites	34
Table 2.8	Microprobe analyses of residual glass spots in nephelinites	37
Table 2.9	Averaged microprobe analyses of olivine in ultramafic xenoliths	48
Table 2.10	Averaged microprobe analyses of pyroxenes in ultramafic xenoliths	52

Table 2.11	Averaged microprobe analyses of chromian spinel in ultramafic xenoliths	57
Table 3.1	Equilibrium temperatures of ultramafic xenoliths	59
Table 4.1	Whole rock analyses and normative compositions of Volcano Mountain lava flows	73
Table 4.2	Phase composition matrix	81
Table 5.1	Results of mass balance subtraction calculations for sample VM 6C	93
Table 5.1(a)	Estimated modal distribution of mineral phases near residual glass patches	94
Table 5.2	Mole fraction of forsterite in three nephelinites	100
Table 5.3	Observed and calculated pyroxene compositions in terms of mole fraction of diopside	101

LIST OF FIGURES

Figure 1.1 Map of the Yukon Territory.	3
Figure 1.2 Topographic map of Volcano Mountain.	8
Figure 2.1 Ternary classification diagram for ultramafic rocks.	14
Figure 2.2 Pyroxene quadrilateral.	29
Figure 2.3 Compositional range of the oxide phase in Volcano Mountain nephelinites.	36
Figure 2.4 Alkali versus silica plot of the residual glass from the Volcano Mountain nephelinites.	42
Figure 2.5 Pyroxene quadrilateral showing the compositional range of the xenolithic pyroxenes.	46
Figure 2.6 Ternary diagram showing the compositional range of the chromian spinels in the ultramafic nodules from Volcano Mountain.	47
Figure 3.1 Two-pyroxene geothermometer by Lindsley (1983), at 15 kbar.	62
Figure 3.2 Position in P-T space of the reaction curves modeled in the CMAS system.	63
Figure 4.1 Analyses of Volcano Mountain lava flows.	74
Figure 4.2 Classification of Na-rich alkaline rocks (after Irvine and Baragar, 1971).	75
Figure 4.3 Mg-number ($MgO/(0.8998Fe_2O_3+FeO+MgO)$) versus total alkali (Na_2O+K_2O) diagram.	76
Figure 4.4 Phase displacement vector.	80
Figure 4.5 Crystal differentiation plots (whole rocks).	83
Figure 4.6 Crystal differentiation plots (residual glasses: VM 01 XE 05).	86
Figure 4.7 Crystal differentiation plot (residual glass: VM 6C).	87

Figure 5.1 Liquid lines of descent modeled with the program MARK (Nicholls, 1991).	96
Figure 5.2 Variation diagram of total alkali ($\text{Na}_2\text{O}+\text{K}_2\text{O}$), total iron ($0.899\text{Fe}_2\text{O}_3+\text{FeO}$), and magnesium.	97
Figure 5.3 P-T curves constraining the crystallization path of Volcano Mountain nephelinites.	99
Figure 5.4 Expected compositions of olivine phenocrysts.	102
Figure 5.5 Olivine + high calcium pyroxene + plagioclase cotectic for melts at one atmosphere or 8-30 kbars (after Sack <i>et al.</i> , 1987).	105
Figure 5.6 Log a_{SiO_2} versus temperature diagrams (after Ghiorso and Carmichael, 1990).	

LIST OF PLATES

		107
Plate 1	a) xenocrystic olivine phenocryst; b) intratelluric olivine phenocryst.	4
Plate 2	a) contact between olivine and lavas; b) contact between pyroxene and lavas	6

Suddenly Christopher Robin began to tell Pooh about some things: People called Kings and Queens, and something called Factors, and a place called Europe, and an island in the middle of the sea where no ships came, and how to make a Suction Pump (if you want to), and when Knights were Knighted, and what comes from Brazil. And Pooh said "Oh!" and "I didn't know", and thought how wonderful it would be to have a Real Brain which could tell you Things.

A.A.Milne

SECTION 1

1.1 Objectives

The purpose of this study is primarily to describe the mineralogy and petrology of a suite of rocks consisting of nephelinitic samples from three Recent flows and their associated ultramafic xenoliths.

Three nodule-bearing lava flows from Volcano Mountain were sampled. Nine samples from the lava flows were analyzed: VM 01 and XE 02 from the oldest flow, VM 2C, VM 3C, VM 6C, and VM 7C from the youngest flow, and XE 11 from the middle flow. Sample VM 4S was collected from a flow in the southern part of Volcano Mountain. Twenty-five xenoliths were collected and eight of them were analyzed: XE 01, XE 02, which belong to the oldest lava flow, XE 03, XE 06, XE 12B, XE 15, AND XE 25, which were collected from the middle flow (which is the richest in xenoliths), and VM 7C which was found within one of the samples of the youngest flow (tables 2.9-2.11). The geographic location of the flows and their field relationships are shown in figure 1.1 and 1.2. Figure 1.2 also shows the positions in the flows the samples were collected from. The samples collected were analyzed with the methods described in section 2. The pressure-temperature conditions of both have been investigated through thermodynamic modeling of the lavas, and geothermobarometry based on mineral assemblages in the xenoliths, to better understand their provenance

and their relationship to each other.

The rocks from Volcano Mountain were chosen for this study because there is no previous description for them other than routine descriptions in reconnaissance mapping by the Geological Survey of Canada (Bostock, 1936, Sinclair *et al.*, 1977), and because of their unusual composition. The importance of describing and studying the petrology of the cinder cones in Northern Yukon and Alaska becomes clear when their occurrence and unusual composition are put in a regional tectonic context with the distribution of Recent volcanoes occurring from the Cascades to the Aleutians.

1.2 Geologic setting

The morphology of Volcano Mountain and its most recent eruptions have been described by Jackson and Stevens (1992); the dates reported in the legend of figure 1.2 are also based on the work of Jackson and Stevens (1992). According to the palynological and dendrochronological studies, the age of the lowermost flow sampled is about 7500 years, the middle flow is 1500-3000 years, and the youngest is 1000 years old or younger. The eruption that produced the oldest flow seems to have been the most violent, causing the collapse of the northeastern flank of the cone structure. The other two flows appear to have been more restricted in extent, and perhaps

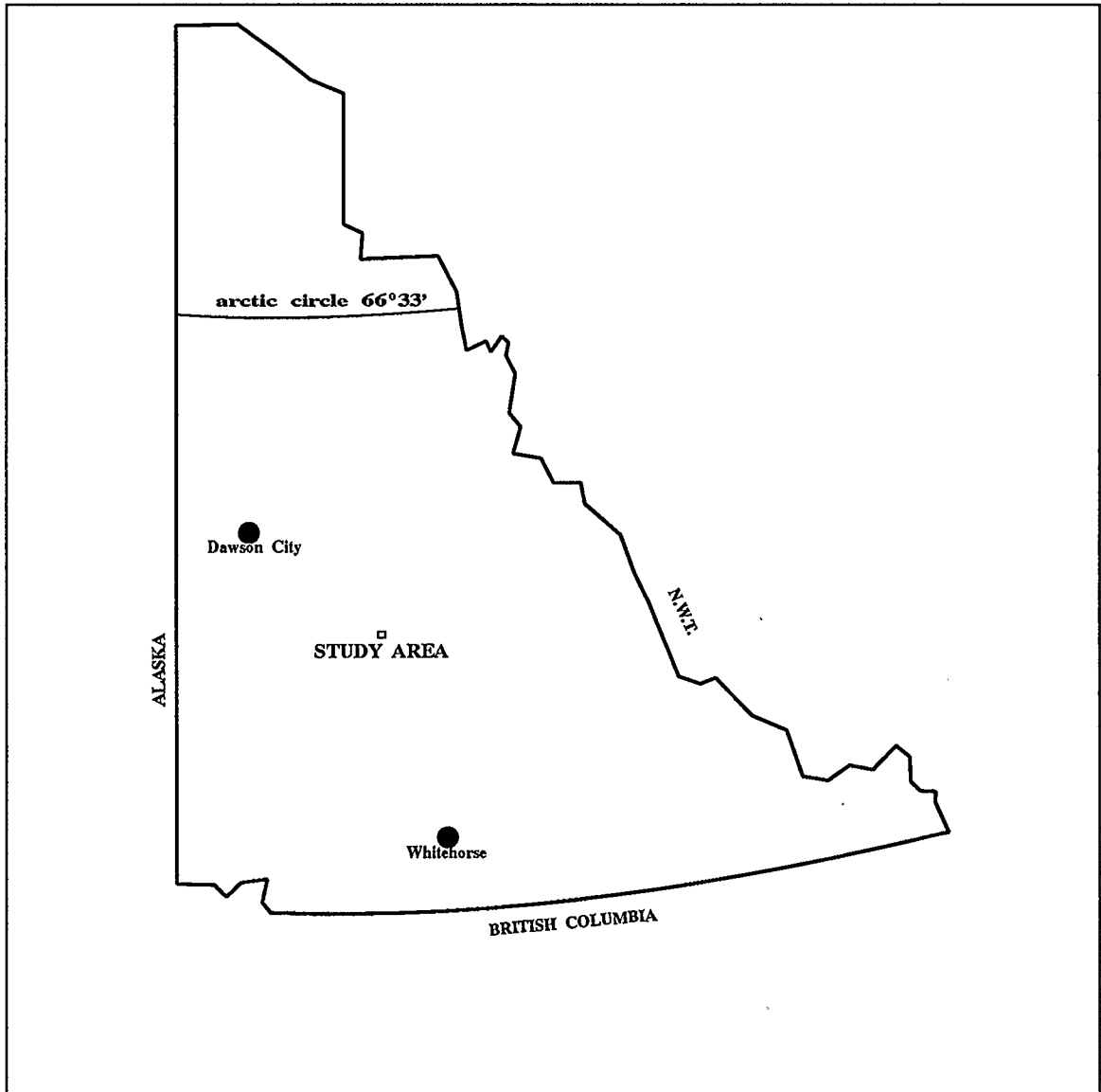
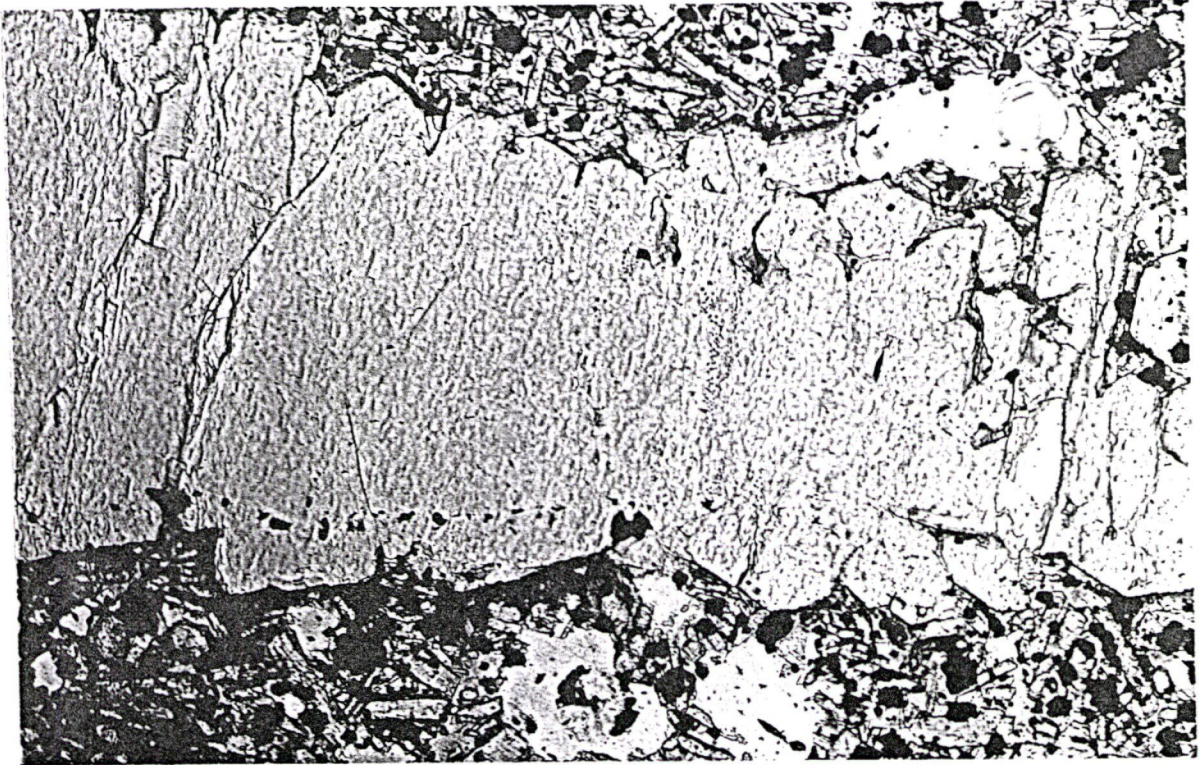


Figure 1.1
Map of the Yukon Territory, showing the location of the study area.

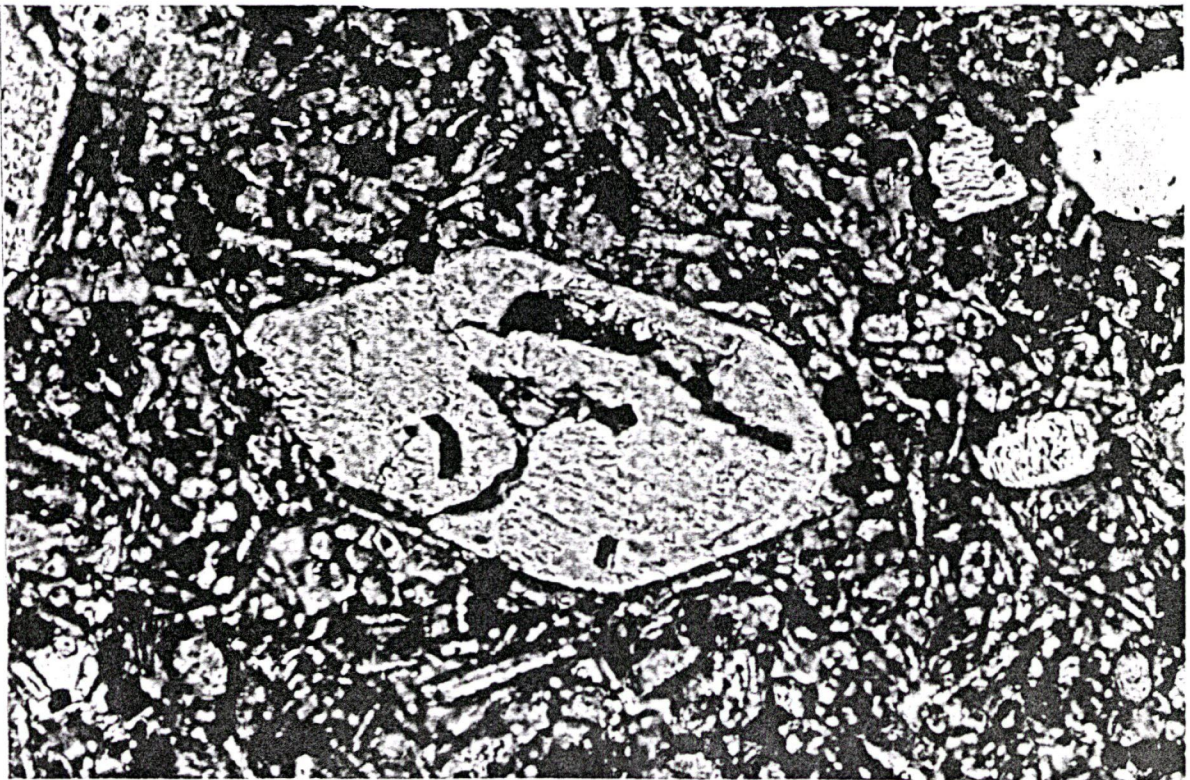
Plate 1

a) Xenocrystic olivine phenocryst, with characteristic euhedral overgrowths and glassy rims. Field of view is 0.5 mm wide.

b) Intratelluric olivine phenocryst showing resorption features. Field of view is 0.5 mm wide.



a)

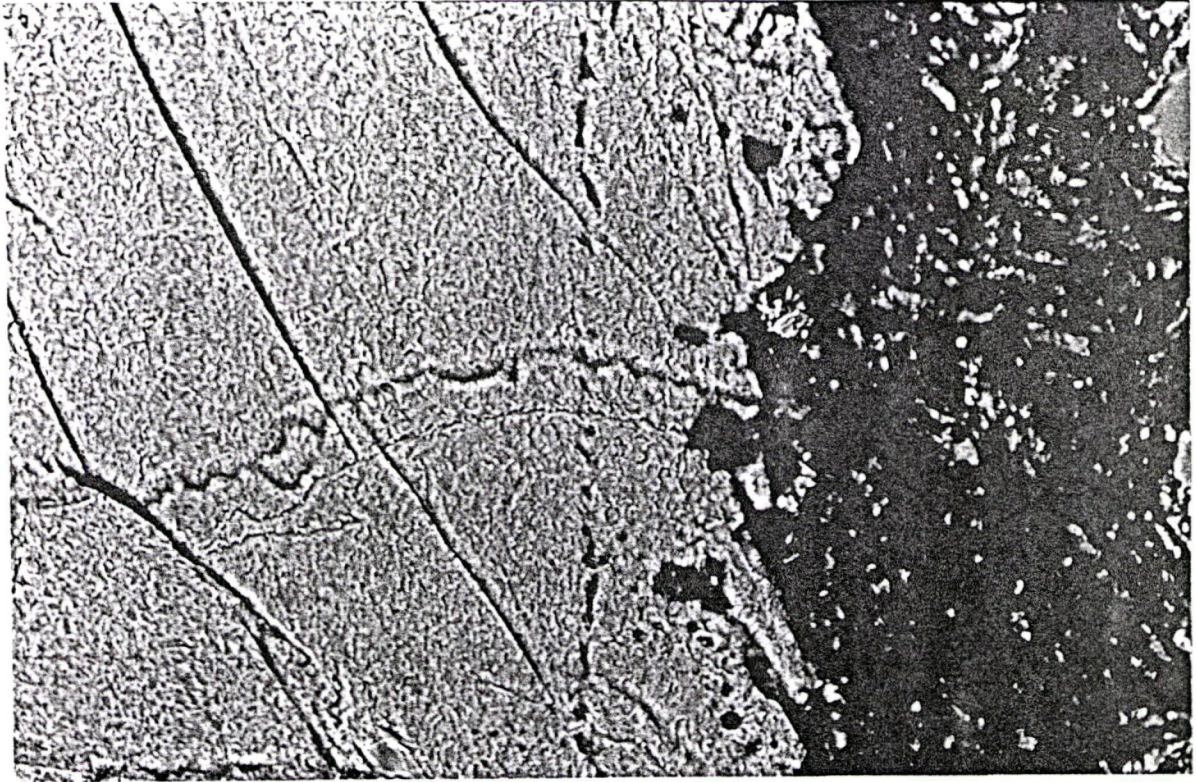


b)

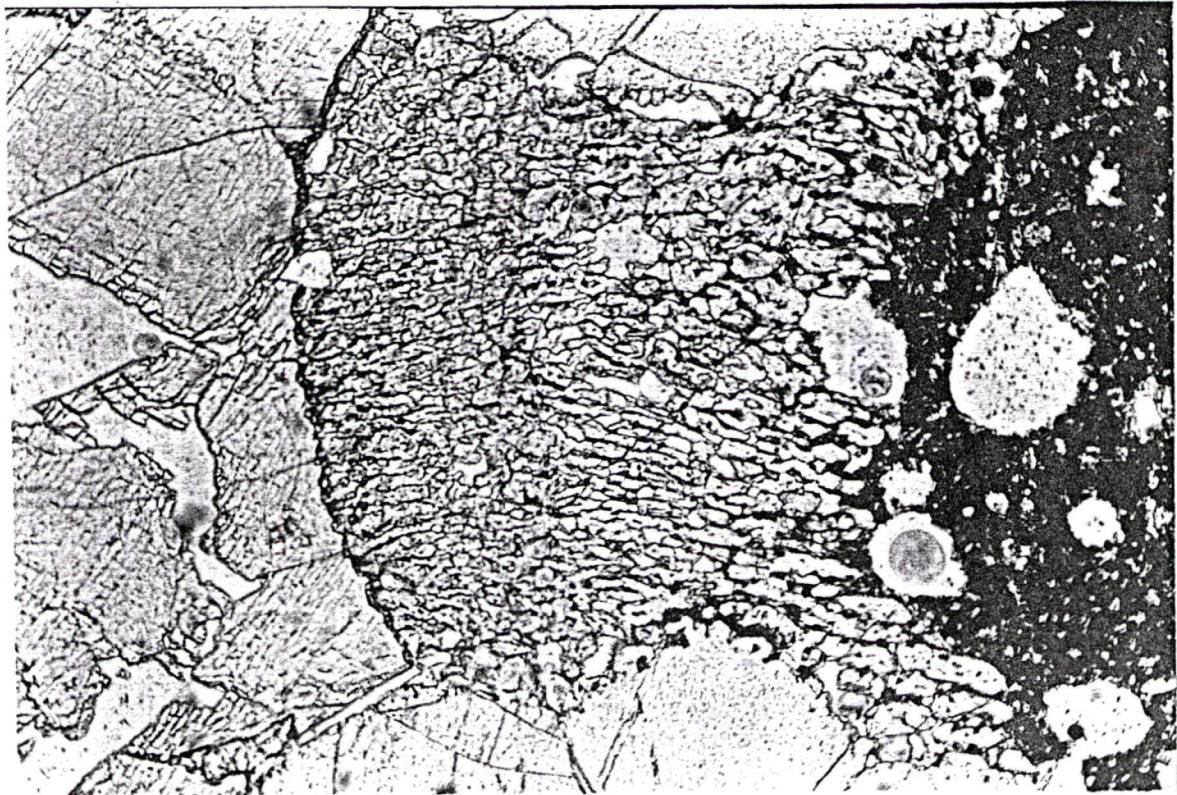
Plate 2

a) Contact between olivine and lavas in the xenoliths. Field of view: 0.6 mm wide.

b) Gradational contact between pyroxene (extreme left) and lavas (extreme right). Field of view: 0.6 mm wide.



a)



b)

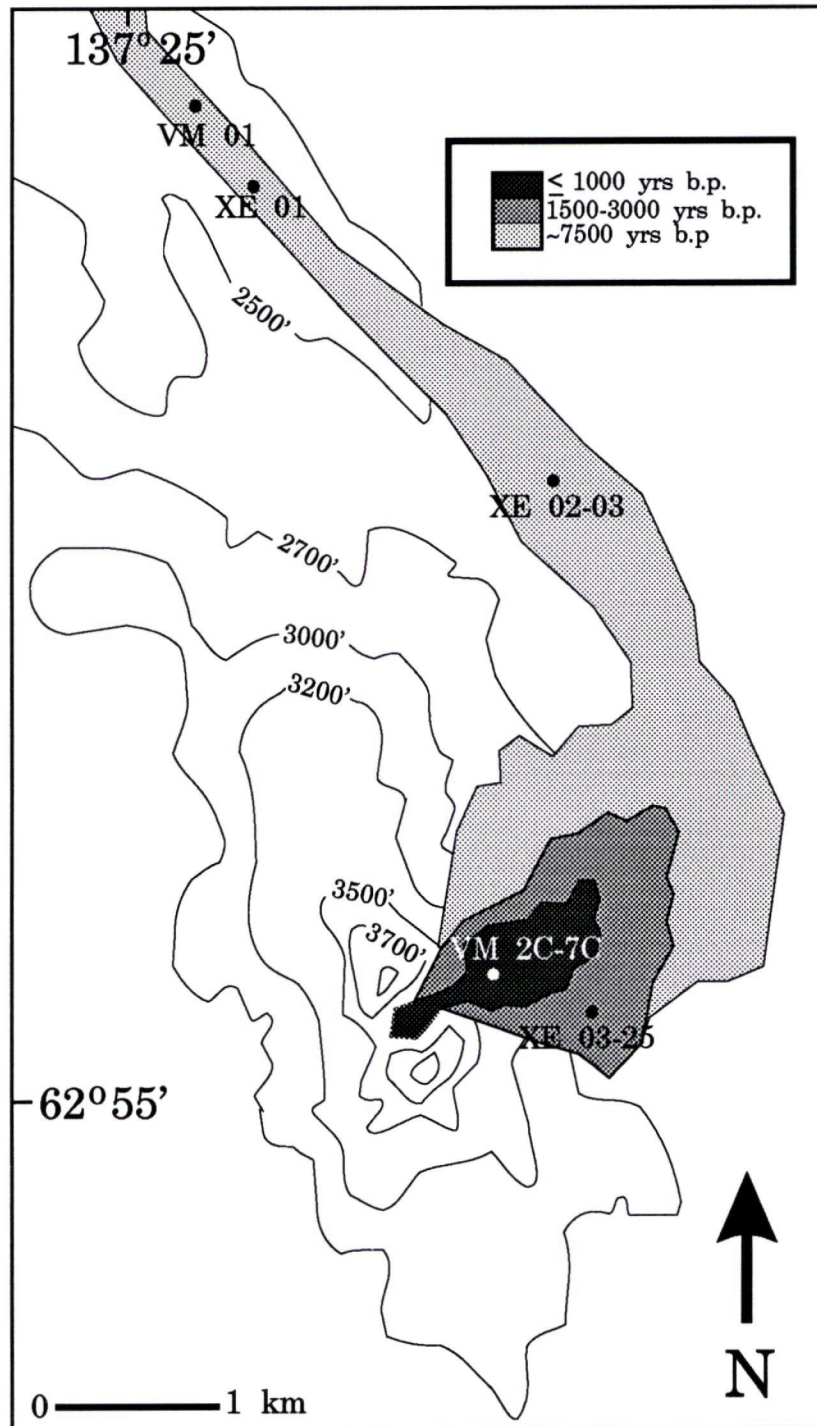


Figure 1.2

Topographic map of Volcano Mountain, showing field relationship between flows, and the sample locations. The different shades of gray represent different flows. Ages are indicated in the box (years before present).

not as violent.

The lavas considered here, as well as other small cinder cones in the area (such as the one described by Sinclair *et al.*, 1977) belong to the Selkirk series (Bostock, 1936), which comprises Quaternary to Recent basaltic/picritic volcanics, volcanic breccias and tuffs, and some rare occurrences of andesites. Below the volcanic rocks, still in the Selkirk series, lie unconsolidated glacial gravels and loess; Sinclair *et al.* (1977) estimated the ages of the lowermost Selkirk flows to postdate the Reid-Nisling glacial advance and perhaps, to be coeval with the McConnell glaciation. The Selkirk Series overlies the Late Tertiary Carmacks Volcanics, a set of vesicular basalt flows forming a large plateau similar in appearance to the columnar basalt flows at Miles Canyon near Whitehorse. Late Jurassic intrusives and gneisses of the Yukon Group form the basement to the younger volcanics and glacial sediments (Bostock, 1936).

On a regional scale, Volcano Mountain is part of the set of Quaternary-to-Recent cinder cones which occur throughout British Columbia trending North-South, the Yukon, and parts of Alaska, where the trend changes to East-West.

The distribution of Tertiary volcanics is generally interpreted as the result of magmatic activity associated with terrane accretion and subduction at the edge of the Intermontane Belt during Late Tertiary (Armstrong, 1988). The regional significance of the Recent volcanics is more enigmatic.

The paucity of deep crustal and mantle data from the Yukon makes it harder to correlate the petrologic information available and formulate a regional interpretation. The silica-poor compositions of the lavas from this study would suggest, according to seismic imaging of the upper mantle from B.C. (Nicholls *et al.*, 1982) a shallower low-velocity zone. An analogous setting of Quaternary Volcanics in central B.C. has been interpreted to represent a zone of crustal weakness, possibly the site of a hot spot, or incipient rifting (Brearley *et al.*, 1982).

SECTION 2

2.1. PETROGRAPHY

Modal compositions of lavas and ultramafic nodules are shown in tables 2.1 and 2.2. Modes were determined by point counting polished sections with an ARL-SEM-Q electron microprobe. Counting time was 1 second and the spacing between spots was 200-250 micrometers for the lavas, 300 micrometers for the xenoliths; the total number of spots analysed varied between 2000 and 7000, depending on the size of the thin section. The probe data was then reduced with CLEAN and MODE programs (Nicholls and Stout, 1986), to obtain modal abundances in the samples.

2.1.1. Host lavas

The lava flows from Volcano Mountain are dark gray to black, ranging from massive to highly vesicular. Vesicles, often elongated, define flow banding, visible at outcrop, hand sample and sometimes thin section scale.

Textures are porphyritic to microporphyritic. The phenocryst assemblage consists almost exclusively of olivine; pyroxene is the most abundant groundmass phase and it also occurs as microphenocrysts (0.5mm in the longest dimension or smaller). In addition to acicular pyroxene, the groundmass consists of olivine, nepheline, leucite, oxides, and patches of clear to dark brown residual glass; the average diameter of the groundmass grains

is 0.003 mm. The glassy patches rarely appear isotropic because they contain microlitic inclusions of nepheline or leucite, or very small oxide grains.

	XE 02	VM 2C	VM 6C	VM 4S
pyx	57.30	46.63	65.53	48.78
oli	23.42	18.49	25.36	23.99
oxi	6.08	3.62	5.56	7.85
lc	8.55	9.52	--	--
ne	2.89	--	1.77	--
glass	1.76	21.74	1.78	19.38
	100.00	100.00	100.00	100.00

Table 2.1

Modal compositions of some of the nephelinites from Volcano Mountain. Abbreviations: pyx: pyroxene; oli: olivine; oxi: oxides; lc: leucite; ne:nepheline.

	XE 03	VM 7C	XE 13	XE 17	XE 20	XE 25	XE 06	XE 12A
oli	96.09	94.35	96.83	90.08	88.25	98.47	99.84	98.80
opx	1.15	0.35	0.95	0.98	5.22	0.44	0.08	0.33
cpx	1.18	1.71	0.81	6.97	5.02	1.09	0.00	0.87
spl	1.58	3.59	1.42	1.97	1.51	0.00	0.08	0.00

Table 2.2

Modal composition of ultramafic nodules in lava flows from Volcano Mountain.

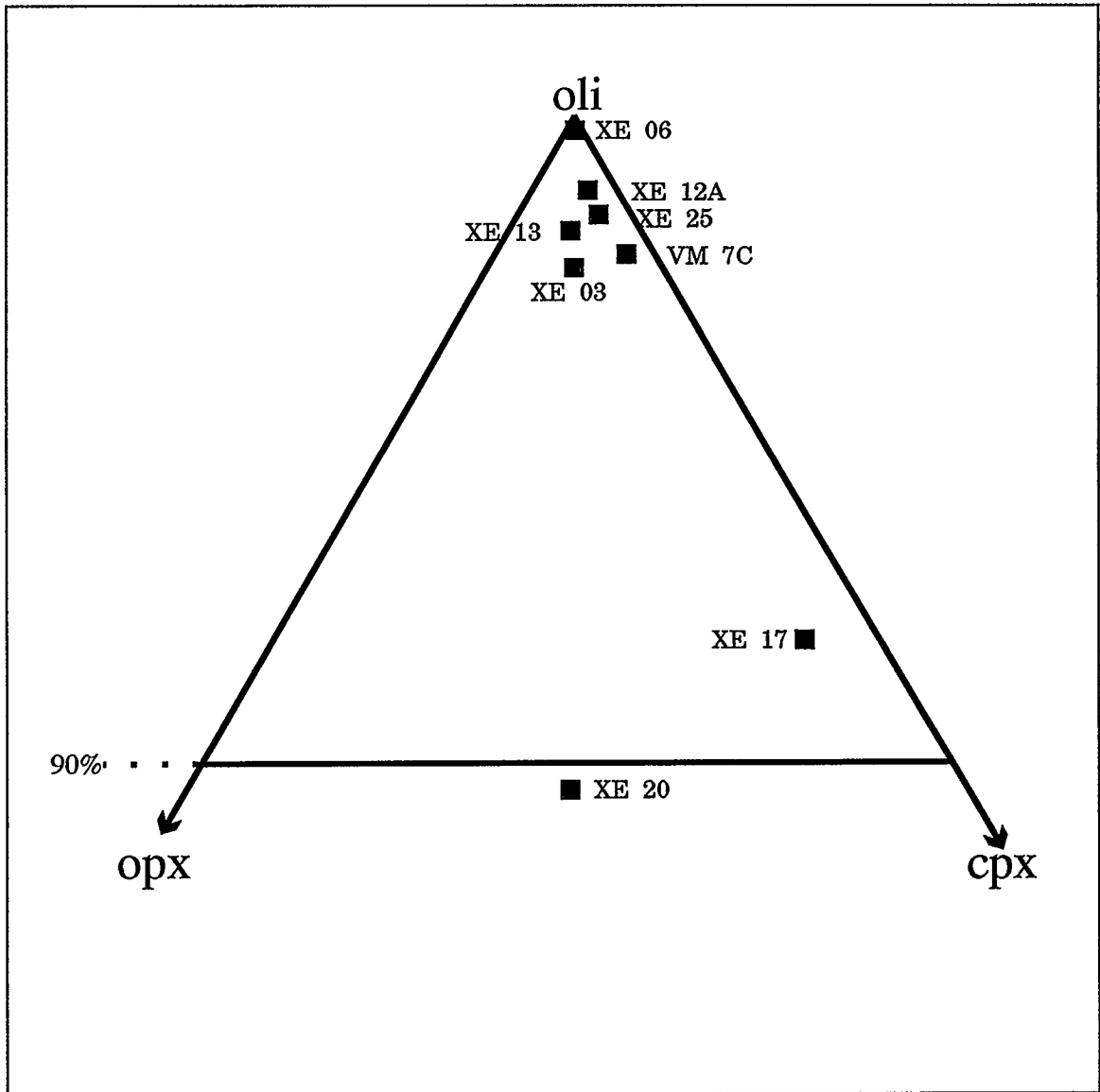


Figure 2.1

Ternary classification diagram for ultramafic rocks: 90% marks the boundary between dunites and olivine-lherzolites. Modal compositions shown in table 2.2 plot in the dunites field with the exception of XE 20, which is classified as a lherzolite.

Olivine diameters range from 0.005 mm in the groundmass to 1 cm for some phenocrysts. The olivine phenocrysts can be divided into two populations: intratelluric and xenocrystic.

Xenocrystic olivine is by far the most abundant phenocryst type. It has characteristics typical of the olivine found in the xenoliths: deformation features such as kink bands and sub-grain boundaries, large (3mm in diameter and up) anhedral shapes, high magnesium content (Fo_{87-90}), no zoning, and low CaO (<0.2 wt%), typical of olivines of plutonic origin (Simkin and Smith, 1966). In addition, the xenocrysts have euhedral overgrowths bordered by glassy rims separating the original grain from the overgrowth (plate 1 a)); these overgrowths are compositionally distinct from the rest of the grain, and are optically discontinuous with respect to the core. For these reasons, xenocrysts probably represent fragments of olivine whose provenance is the same or similar to that of the ultramafic nodules described in section 2.1.2.

Intratelluric olivine phenocrysts are euhedral, often resorbed or embayed (plate 1 b)); they are 1-2mm in maximum diameter, are compositionally zoned, becoming more Fe-rich at the rims and have a higher CaO content (>0.2 wt%) than the xenocrystic olivine.

Pyroxene phenocrysts consist of euhedral to subhedral microphenocrysts, which average 0.5 to 0.1 mm in the long direction. In the groundmass, pyroxene is acicular. Often these microphenocrysts may show simple twinning, sometimes they have dark reaction rims, but very seldom do

they show the resorption or embayment features common in olivine. Compositional zoning was observed in the microphenocrysts of samples VM 6B VM 7C, XE 02, and VM 2C. In plane light the body colour of pyroxenes is light tan or yellow.

Leucite and/or nepheline are present in the groundmass of samples VM 6B, VM 7C, XE 02, VM 2C, XE 05 and XE 11. Leucite is anhedral or euhedral, often rimming larger ulvöspinel grains; nepheline is rarely euhedral and does not appear to occur preferentially near any of the other minerals. In sample XE 11 nepheline occurs as microphenocrysts as well.

Ulvöspinel is the only oxide phase present and consists of equant, sometimes euhedral grains 0.05 to 0.1 mm in diameter.

Residual glass occurs in discrete, isolated patches, often roughly circular and approximately 10 to 20 micrometers in diameter, although larger patches (~100 μ m) can be sporadically observed. These patches usually surround groundmass grains or microphenocrysts. Glassy patches are dark brown to colourless, varying from sample to sample, and within samples, from glassy pocket to glassy pocket.

Calcite occurs very sporadically in the groundmass. Its size is approximately 1 or 2 μ m.

2.1.2 Ultramafic xenoliths

The xenoliths collected for this study are unweathered, subrounded to subangular nodules 2.5 to 10 cm in diameter.

All ultramafic nodules can be classified as dunites (figure 2.1, table 2.1), as they contain more than 90% olivine, with the exception of XE 20, which just falls within the lherzolite field.

The overall texture of these nodules is granoblastic, with equant grains of clinopyroxene, orthopyroxene and olivine, approximately 3-5 mm in diameter. Spinel occurs as elongate fingerlike grains, interstitial to clinopyroxene or orthopyroxene, seldom to olivine. Reaction rims usually surround spinel grains. The size of the spinel is generally smaller than that of the pyroxene and olivine, usually 1-2 mm. in length. The xenoliths do not show any obvious compositional layering, although pyroxene grains often occur together in clusters.

Contacts between the xenoliths and their host are of two types: if olivine is in contact with the lava, then it exhibits overgrowths of more Fe-rich olivine bordered by thin glassy outlines, similar to those observed in the xenocrysts and shown on plate 2 (a). Alternatively, if pyroxene is the mineral in contact with the host picrite, the contact is gradational from the lavas to the xenolith, in a reaction rim containing glass, olivine and pyroxene. This type of contact becomes finer grained towards the lava, and can be several millimeters thick (plate 2 (b)).

Spinel was not observed at the contacts between the xenoliths and the lavas.

Similarly to the olivine xenocrysts, olivine in the xenoliths shows kink-banding, undulose extinction, and sub-grain boundaries, but not much fracturing, except in sample XE 25. The sub-grains sizes in olivine range from 0.5 to 2 mm in diameter.

Xenolithic pyroxenes may show exsolution features, and they tend to be highly fractured; exsolution lamellae or patches are very thin, approximately on the order of 2 to 10 micrometers. Exsolved pyroxenes are usually surrounded by olivine-pyroxene reaction rims. In plane-polarized light, clinopyroxenes are faintly pleochroic, pale green to yellow, orthopyroxenes are colourless.

Spinels are dark brown in plane-polarized light, have dark coronas and sometimes also finer grained reaction rims consisting of glass, olivine and pyroxene suggesting textural disequilibrium with the other mineral phases.

2.2 MINERALOGY

Mineral phases in the xenoliths and the host lavas, and residual glasses were analyzed with an ARL SEMQ electron microprobe. Under present operating conditions (Nicholls and Stout, 1986) the spectra for nine different elements can be collected by nine wavelength-dispersive spectrometers. Phases which required more than nine elements for a complete analysis such as oxides or residual glasses, were analyzed in a double run using an automated stage drive to relocate the same spots. Analyses of V_2O_5 were corrected for TiO_2 interference.

Table 2.3

Average microprobe analyses, number of ions and endmember mole fraction of olivine from Volcano mountain nephelinites. 2.3 (a): average groundmass composition; 2.3(b): average composition of cores in phenocrysts and microphenocrysts; 2.3(c): average composition of rims in olivine phenocrysts and microphenocrysts. Analyses in weight percent.

Table 2.3 (a)					
	VM3C	X02	VM01	VM4S	VM2C
SiO ₂	40.83	41.14	40.31	40.32	40.57
TiO ₂	0.05	0.06	0.04	0.04	0.05
Al ₂ O ₃	<0.04	<0.04	<0.04	<0.04	<0.04
FeO	16.56	16.33	14.72	14.87	17.70
MgO	41.79	42.76	42.71	42.98	41.32
CaO	0.37	0.34	0.28	0.27	0.32
Cr ₂ O ₃	0.04	0.05	0.04	0.03	0.03
total	99.73	100.7	98.13	98.55	100.02
number of ions based on 4 oxygens					
Si	1.03	1.02	1.02	1.02	1.03
Fe+2	0.35	0.34	0.31	0.32	0.37
Mg	1.57	1.59	1.62	1.63	1.56
Ca	0.01	0.00	0.00	0.01	0.01
sum	2.96	2.97	2.97	2.97	2.97
mol% endmembers					
Fo	81.81	82.35	83.79	83.74	80.62
Fa	18.19	17.65	16.21	16.26	19.38

Table 2.3 (b)

	VM3C	X02	VM01
SiO2	41.15	42.11	40.84
TiO2	0.02	--	0.02
Al2O3	0.05	--	<0.04
FeO	15.04	8.47	12.00
MgO	43.43	48.73	44.67
CaO	0.32	0.04	0.18
Cr2O3	0.02	0.03	0.03
total	100.05	99.39	97.78
number of ions based on 4 oxygens			
Si	1.03	1.03	1.03
Fe+2	0.31	0.17	0.25
Mg	1.62	1.77	1.68
Ca	0.01	0.00	0.01
sum	2.97	2.97	2.97
mol % endmembers			
Fo	83.73	91.11	86.90
Fa	16.27	8.89	13.10

Table 2.3 (b) (cont'd)

	VM2C	VM7C	VM6C
SiO ₂	40.16	40.19	39.44
TiO ₂	0.04	0.03	0.03
Al ₂ O ₃	<0.04	<0.04	<0.04
FeO	18.64	15.10	16.03
MgO	40.99	44.13	43.89
CaO	0.33	0.24	0.28
Cr ₂ O ₃	0.03	0.03	0.03
total	100.22	99.78	99.75
number of ions based on 4 oxygens			
Si	1.02	1.01	1.00
Fe ⁺²	0.39	0.32	0.34
Mg	1.55	1.65	1.655
Ca	0.01	0.01	0.01
sum	2.98	2.99	3.00
mol % endmembers			
Fo	79.67	83.89	82.99
Fa	20.33	16.11	17.01

Table 2.3 (c)

	VM3C	X02	VM2C	VM7C	VM6C
SiO2	38.83	41.06	40.45	39.27	38.13
TiO2	0.05	0.04	0.05	0.08	0.06
Al2O3	<0.04	0.07	<0.04	<0.04	0.04
FeO	21.93	17.88	20.18	20.46	22.18
MgO	37.22	40.65	39.13	39.27	38.62
CaO	0.44	0.27	0.40	0.40	0.44
Cr2O3	0.03	0.03	0.03	0.04	0.02
total	98.51	100.04	100.30	99.58	99.52
number of ions based on 4 oxygens					
Si	1.02	1.04	1.03	1.01	1.00
Fe+2	0.48	0.38	0.43	0.44	0.48
Mg	1.45	1.53	1.49	1.51	1.50
Ca	0.01	0.01	0.01	0.01	0.01
sum	2.97	2.96	2.96	2.98	2.99
mol % endmembers					
Fo	74.96	80.20	77.56	77.38	75.63
Fa	25.04	19.80	22.44	22.62	24.37

Data was processed with SLAVE programs (Nicholls *et al.*, 1977) which include Bence-Albee (1968) correction methods. Detection limits are given in Appendix A.

2.2.1 Host lavas

OLIVINE

The compositions, number of ions based on 4 oxygens and molar percent endmember content of olivine in the groundmass and phenocrysts (cores and rims) are reported on tables 2.3 (a) through (c). Groundmass composition ranges between Fo₈₃ and Fo₈₀; phenocrysts and microphenocrysts are normally zoned with compositions in the core ranging between Fo₉₁ and Fo₇₉, and in the rims between Fo₈₀ and Fo₇₄. The largest compositional difference in olivine occurs in the end member content of the phenocrysts cores. This could be due to the different types of phenocrysts (xenocrystic and intratelluric) averaged in the analyses of the cores. Samples XE 02 and VM 01 have a more typical xenocrystic composition, with low CaO, which indicates crystallization under plutonic conditions (Simkin and Smith, 1966), whereas the rest seem to be predominantly intratelluric.

PYROXENE

Average microprobe analyses, number of ions based on 6 oxygens and molar percent end member contents of pyroxene are shown in table 2.4. The

Table 2.4

Average microprobe analyses (in weight percent), number of ions and mole fraction endmembers of pyroxene from Volcano mountain nephelinites. The number of ions and endmember composition were calculated with the program PX (rel. 3.0, Cebria, 1990). The reported endmember compositions are according to the I.M.A. classification (Morimoto, 1989).

	VM7C	VM7C	VM6C	VM6C
	(a)	(b)	(a)	(b)
SiO ₂	45.29	48.53	45.59	48.30
TiO ₂	3.80	2.51	3.69	2.55
Al ₂ O ₃	7.99	5.20	6.59	4.40
FeO	8.52	7.67	8.61	7.83
MgO	11.78	13.24	12.16	13.53
CaO	21.49	21.94	22.30	22.59
Na ₂ O	0.93	0.69	0.66	0.58
total	99.82	99.80	99.65	99.82
number of ions based on 6 oxygens				
Si	1.69	1.81	1.71	1.80
Ti	0.11	0.07	0.10	0.07
Al	0.35	0.23	0.29	0.19
Fe ⁺³	0.12	0.07	0.13	0.11
Fe ⁺²	0.15	0.17	0.14	0.13
Mg	0.66	0.73	0.68	0.75
Ca	0.86	0.87	0.90	0.90
Na	0.07	0.05	0.05	0.04
sum	4.00	4.00	4.00	4.00
mol % endmembers				
Wo	48.27	47.34	48.55	47.76
En	36.80	39.74	36.82	39.79
Fs	14.94	12.92	14.63	12.45

Table 2.4 (cont'd)

	VM4S	VM4S	XE02
	(a)	(b)	
SiO ₂	43.94	47.52	44.89
TiO ₂	4.26	2.67	3.69
Al ₂ O ₃	8.64	5.43	7.85
FeO	8.77	8.03	8.43
MgO	11.56	13.24	11.94
CaO	21.95	22.18	21.99
Na ₂ O	0.78	0.58	0.74
total	99.93	99.69	99.54
number of ions based on 6 oxygens			
Si	1.64	1.77	1.68
Ti	0.12	0.08	0.10
Al	0.38	0.24	0.35
Fe ⁺³	0.15	0.11	0.14
Fe ⁺²	0.13	0.14	0.13
Mg	0.64	0.74	0.67
Ca	0.88	0.89	0.88
Na	0.06	0.04	0.05
sum	4.00	4.00	4.00
mol % endmembers			
Wo	48.92	47.73	48.68
En	35.83	39.64	36.76
Fs	15.25	12.62	14.56

Table 2.4 (cont'd)

	VM3C	VM3C	VM1	VM1
	(a)	(b)	(a)	(b)
SiO ₂	43.25	44.39	44.98	46.54
TiO ₂	4.44	2.66	3.80	2.96
Al ₂ O ₃	9.34	5.23	7.01	5.14
FeO	9.26	8.18	8.77	8.12
MgO	10.93	13.27	12.24	13.07
CaO	21.31	22.37	22.17	22.89
Na ₂ O	1.00	0.61	0.75	0.63
total	99.54	100.15	99.76	99.39
number of ions based on 6 oxygens				
Si	1.63	1.70	1.68	1.74
Ti	0.13	0.08	0.11	0.08
Al	0.41	0.24	0.31	0.22
Fe+3	0.16	0.25	0.17	0.16
Fe+2	0.14	0.01	0.11	0.09
Mg	0.61	0.76	0.68	0.73
Ca	0.86	0.92	0.89	0.92
Na	0.07	0.05	0.05	0.05
sum	4.00	4.00	4.00	3.99
mol % endmembers				
Wo	48.72	48.94	48.35	49.08
En	34.76	40.38	37.13	38.98
Fs	16.52	10.68	14.52	11.94

Table 2.4 (cont'd)

	VM2C	VM2C
	(a)	(b)
SiO ₂	45.52	49.45
TiO ₂	3.88	2.33
Al ₂ O ₃	8.03	4.11
FeO	8.58	8.20
MgO	11.87	13.38
CaO	21.79	22.25
Na ₂ O	0.91	0.87
total	100.63	100.61

number of ions based on 6
oxygens

Si	1.69	1.83
Ti	0.11	0.07
Al	0.35	0.18
Fe+3	0.12	0.10
Fe+2	0.14	0.15
Mg	0.66	0.74
Ca	0.87	0.88
Na	0.07	0.06
sum	4.00	4.00

mol % endmembers

Wo	48.43	47.08
En	36.69	39.38
Fs	14.88	13.54

endmember compositions which are also plotted on a pyroxene quadrilateral (figure 2.2), are based on the I.M.A. classification, and were calculated using the program PX (rel. 3.0, Cebria, 1990).

Two different clinopyroxenes are found in samples VM 6C, VM 4S, VM 3C, VM 2C, and VM 01: the pyroxene labeled (a) in table 2.4 has higher Ti, Fe, Na and Al; the pyroxene labeled (b) in table 2.4 has higher Si, Mg, and generally Ca. The microlitic pyroxene of the groundmass is of type (a), and this is the only type of pyroxene present in sample XE 02 which does not contain any pyroxene microphenocrysts. In the larger zoned phenocrysts, composition (a) seems more common in zones near the edges of the grains, but can also occur in the cores or in the middle.

All pyroxenes were classified as titaniferous diopsides (Morimoto, 1989) and their compositional range is $Wo_{47-49}En_{34-40}Fs_{10-16}$. These compositions almost fall on the Diopside-Hedenbergite join (figure 2.2).

NEPHELINE

The average compositions and number of ions (based on 32 oxygens) for samples VM 6C, VM 7C, XE 02, and XE 11 are shown on table 2.5.

The main characteristic of all nephelines analyzed is the high SiO_2 (43-52 wt%) and lower Al_2O_3 content (31-26 wt%) with respect to other reported occurrences of nepheline worldwide (Deer *et al.*, 1963), which average respectively about 43 and 33 percent in weight.

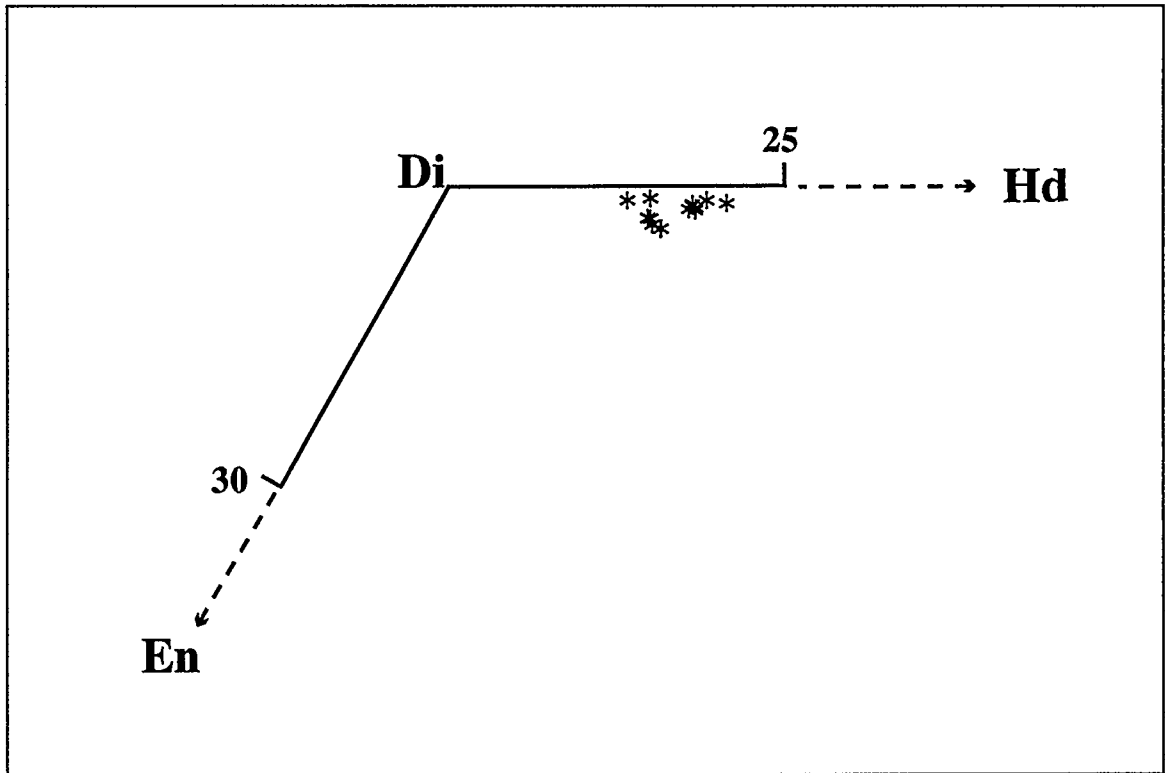
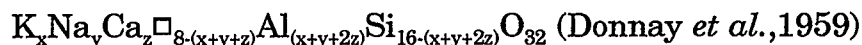


Figure 2.2

Pyroxene quadrilateral illustrating the compositional range of the pyroxenes in Volcano Mountain nephelinites.

It has been recognized for some time that in naturally occurring nephelines the Si:Al ratio is rarely 1:1. Furthermore, vacant sites are usually occupied by Fe, and a small amount of Mg, Mn or Ti can substitute in the alkali site (Hahn and Buerger, 1955). The general formula for nepheline is commonly expressed as



where □ represents the vacant sites. Using this formula, and taking into account all the allowed substitutions, the nephelines analyzed are stoichiometric.

LEUCITE

Leucite occurs in samples VM 7C, XE 02 and VM 2C. The averaged compositions and number of ions based on 6 oxygens are reported on table 2.6.

The SiO₂ content of leucite in the samples analysed is lower than that of other leucites reported in the literature (for example in Deer *et al.*, 1963); however, experimental studies (Bowen, 1928; Fudali, 1963) show that SiO₂ content in leucites can be as low as about 30 percent by weight, depending on presence of other components, and temperature or pressure conditions of crystallization. By contrast, the amount of TiO₂, FeO and MgO appears quite high, but this can be attributed partly to the small grain size of leucite and its occurrence within glassy patches, which contain a fair amount of mafic components. In any case, the calculated cation contents show the stoichiometry to be consistent with the leucite formula.

Table 2.5

Average microprobe analyses (in weight percent) and number of ions of nepheline in Volcano mountain nephelinites.

	VM6C	VM7C	XE02	XE11
SiO ₂	52.81	48.96	54.13	43.03
TiO ₂	0.16	0.15	0.20	0.08
Al ₂ O ₃	27.37	30.36	26.91	31.23
FeO	0.85	0.79	1.53	1.15
MgO	0.10	0.14	0.37	0.23
CaO	0.21	0.88	1.16	3.09
Na ₂ O	15.27	15.19	15.58	15.83
K ₂ O	2.10	2.89	1.79	5.12
TOTAL	98.93	99.37	101.67	99.92
number of ions based on 32 oxygens				
Si	9.85	9.20	9.87	8.36
Ti	0.02	0.02	0.03	0.01
Al	6.02	6.73	5.78	7.15
Fe+2	0.13	0.12	0.23	0.19
Mg	0.03	0.04	0.10	0.07
Ca	0.04	0.18	0.23	0.64
Na	5.52	5.53	5.51	5.96
K	0.50	0.69	0.42	1.27

Table 2.6

Averaged microprobe analyses (in weight percent) and number of ions of leucite in Volcano mountain nephelinites.

	VM7C	XE02	VM2C
SiO ₂	53.83	50.59	54.87
TiO ₂	0.81	1.34	0.47
Al ₂ O ₃	21.73	22.02	22.68
FeO	2.20	5.96	1.22
MgO	0.28	0.22	0.10
CaO	0.59	0.16	0.56
Na ₂ O	0.26	1.29	0.25
K ₂ O	20.02	16.02	20.68
TOTAL	99.79	97.60	100.84

number of ions based on 6 oxygens

Si	1.98	1.91	1.99
Ti	0.02	0.04	0.01
Al	0.94	0.98	0.97
Fe+2	0.07	0.19	0.04
Mg	0.01	0.01	0.01
Ca	0.02	0.01	0.02
Na	0.02	0.09	0.02
K	0.94	0.77	0.95
sum	4.01	4.01	4.00

OXIDES

Average compositions and mole fraction of magnetite-ulvöspinel were calculated with the program OXIDE (Ghiorso, 1979) and are shown on table 2.7. The ulvöspinel endmember in table 2.7 actually represents the mole fraction of all +2 metal ions in the fourfold site. Figure 2.3 shows the position of the oxides in a mole per cent diagram in the system $\text{FeO-Fe}_2\text{O}_3\text{-TiO}_2$, with tie lines representing the main solid solution series (after Buddington and Lindsley, 1964). Only one oxide phase is present in the host lavas, and as shown on figure 2.3, it belongs to the magnetite-ulvöspinel (Mt-Usp) solid solution series.

All analyses cluster around $\text{Mt}_{35-40}\text{Usp}_{60-65}$, except sample VM3C which possesses two oxide populations, one with a larger component of magnetite (about 74% mole fraction).

RESIDUAL GLASS

Residual glass occurs in all the samples analyzed, with the exception of XE-11 although its modal abundance varies from sample to sample (table 2.2). Compositions of each individual patch of residual glass within each sample are shown on table 2.8; no average glass values are reported due to the great compositional diversity between patches even within the same sample. A plot of alkali versus silica (figure 2.4, after Irvine and Baragar, 1972) shows the silica content to be essentially constant, whereas the amount of total alkali varies within each sample as well as between samples.

Table 2.7

Averaged microprobe analyses (in weight percent) and mole fraction of ulvöspinel/magnetite (usp, mt) solid solution in Volcano mountain nephelinites.

	VM01	VM3C	VM3C
SiO ₂	0.00	0.42	0.00
TiO ₂	16.49	5.07	7.15
Al ₂ O ₃	3.78	4.11	7.87
V ₂ O ₃	0.67	1.29	0.73
Cr ₂ O ₃	3.67	0.21	18.75
FeO	39.90	26.31	28.24
Fe ₂ O ₃	30.88	54.55	29.42
MnO	0.55	0.57	0.62
MgO	4.25	6.08	6.68
CaO	0.22	0.42	0.07
Total	100.50	99.00	99.53
mol % endmembers			
mt	0.4149	0.7389	0.3845
usp	0.5851	0.2611	0.6155

Table 2.7 (cont'd)

	VM2C	XE02	VM7C	VM6C
SiO ₂	0.19	0.45	0.00	0.00
TiO ₂	18.17	17.61	20.20	20.93
Al ₂ O ₃	2.68	2.56	2.83	2.95
V ₂ O ₃	0.97	0.97	0.37	0.78
Cr ₂ O ₃	0.09	0.92	2.06	0.54
FeO	40.18	40.86	42.87	45.47
Fe ₂ O ₃	30.34	29.62	25.63	25.59
MnO	0.64	0.62	0.65	0.63
MgO	4.32	3.65	4.01	2.99
CaO	0.50	0.60	0.22	0.26
Total	98.07	97.86	98.81	100.12
mol % endmembers				
mt	0.4200	0.4058	0.3519	0.3495
usp	0.5783	0.5942	0.6481	0.6505

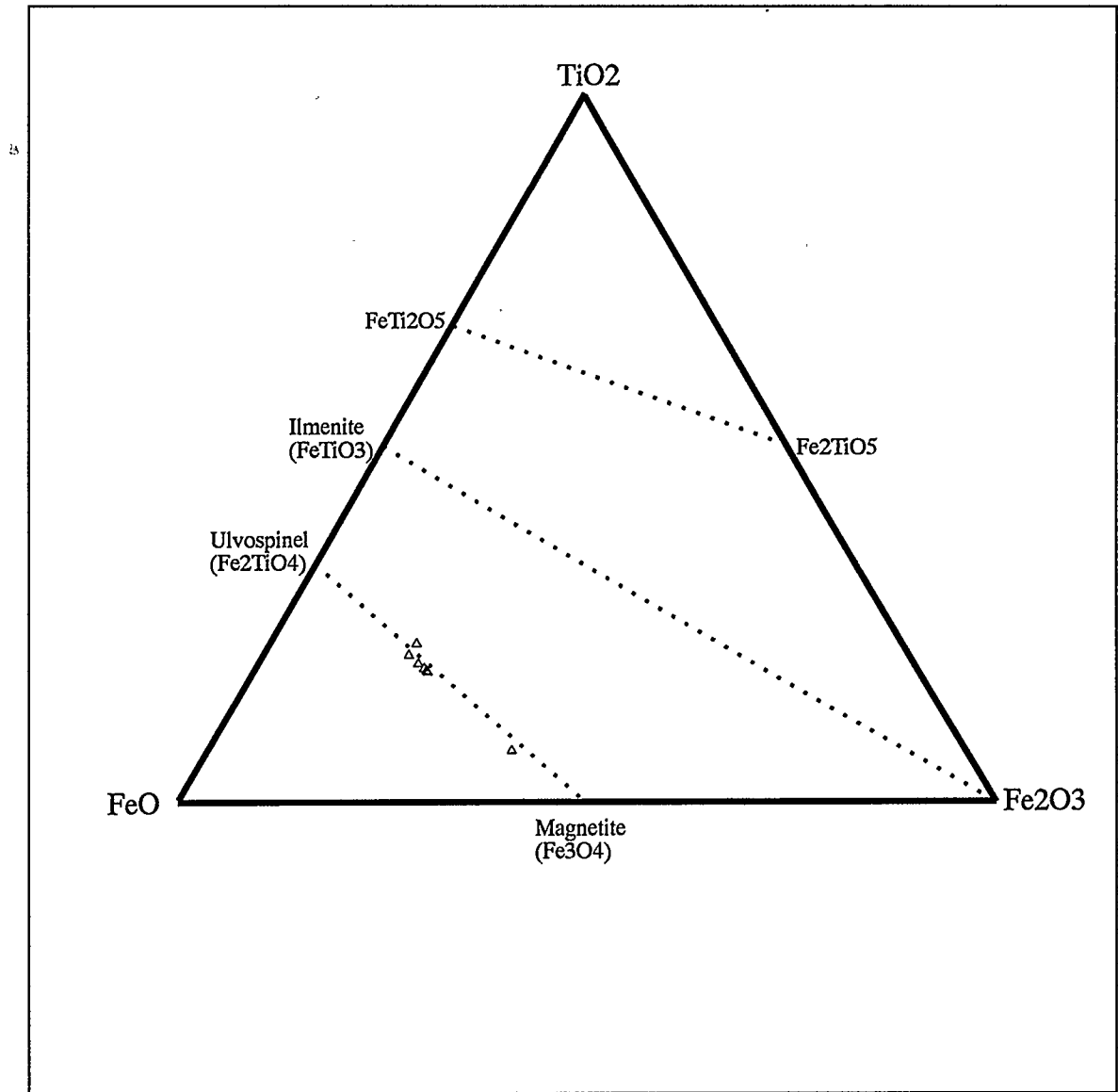


Figure 2.3

Compositional range of the oxide phase in Volcano Mountain nephelinites. The ternary diagram is after Buddington and Lindsley (1964).

Table 2.8

Microprobe analyses of volcanic glass spots from the Volcano mountain nephelinites.

	SiO2	TiO2	Al2O3	FeO	MgO	CaO	Na2O	K2O	P2O5	F	total
VM6C	54.33	0.37	24.57	1.75	0.21	0.17	13.97	2.98	0.33	0.00	98.68
VM6C	56.23	0.67	20.88	2.50	0.35	0.34	8.77	6.37	0.72	0.00	96.83
VM6C	54.47	0.33	25.67	1.24	0.12	0.21	14.35	2.63	0.72	0.01	99.75
VM6C	53.72	0.15	27.55	0.67	0.08	0.14	13.77	1.68	0.10	0.05	97.91
VM6C	55.99	0.15	27.45	0.83	0.09	0.22	9.80	2.52	0.11	0.02	97.18
VM3C	56.38	1.38	21.10	2.16	0.55	1.58	5.20	6.61	2.71	0.07	97.74
VM3C	56.53	1.31	21.04	2.16	0.58	1.32	5.44	6.66	5.57	0.11	100.72
VM3C	55.57	1.30	22.34	2.77	0.47	1.00	6.65	6.44	0.49	0.02	97.05
VM3C	56.58	1.34	22.22	2.59	0.47	0.94	6.41	6.48	1.14	0.03	98.20
VM3C	58.97	2.00	20.90	3.34	0.57	0.67	3.95	5.64	5.21	0.04	101.29
VM3C	56.38	1.70	22.42	2.75	0.51	0.50	5.35	5.84	3.70	0.00	99.15
VM3C	56.17	1.06	22.52	2.40	0.59	0.63	6.10	6.56	1.48	0.08	97.59
VM4S	49.09	2.08	19.30	9.35	1.71	3.79	7.78	4.78	1.33	0.02	99.23
VM4S	49.68	1.99	19.57	9.17	1.71	3.80	7.72	4.79	1.44	0.16	100.03
VM4S	49.19	1.94	18.27	8.48	1.34	3.33	7.34	5.19	1.33	0.06	96.47
VM4S	49.63	2.03	18.59	8.39	1.35	3.37	7.10	5.17	1.46	0.09	97.18
VM4S	49.46	2.04	19.83	6.32	0.93	4.38	8.26	4.66	1.48	0.12	97.48
VM4S	49.04	1.88	19.34	8.11	1.79	4.29	7.47	4.67	1.52	0.06	98.17
VM4S	50.04	1.85	19.40	8.95	1.84	3.71	7.53	4.81	1.48	0.03	99.64
VM4S	50.99	1.60	20.61	6.70	1.20	3.07	7.78	5.35	1.51	0.14	98.95

Table 2.8

	SiO2	TiO2	Al2O3	FeO	MgO	CaO	Na2O	K2O	P2O5	F	total
VM7C	56.46	1.18	21.61	3.26	0.76	1.50	9.13	2.46	0.50	0.07	96.93
VM7C	58.30	0.97	23.00	2.85	0.50	0.73	11.56	1.27	0.47	0.06	99.71
VM7C	57.64	0.52	24.58	1.53	0.33	1.24	12.83	0.65	0.98	0.10	100.40
VM7C	56.19	0.89	23.58	2.36	0.32	0.30	9.29	3.04	0.38	0.10	96.45
VM7C	57.58	1.04	21.85	3.18	0.52	0.54	9.81	1.25	0.34	0.00	96.11
VM7C	46.83	0.20	30.58	0.87	0.42	1.78	14.67	3.06	0.24	0.00	98.65
VM7C	60.09	1.01	22.42	2.02	0.29	0.75	6.54	1.22	0.70	0.06	95.10
VM7C	56.41	0.95	21.87	2.47	0.41	0.29	7.63	7.51	0.40	0.05	97.99
VM7C	55.57	0.92	22.87	2.08	0.34	1.55	14.56	0.51	0.49	0.05	98.94
VM7C	46.08	0.13	29.23	0.85	0.11	2.77	14.14	3.05	2.02	0.12	98.50
VM7C	55.44	0.53	24.85	1.70	0.89	0.40	13.32	0.95	0.75	0.00	98.83
VM7C	57.39	1.32	22.55	2.86	0.37	0.62	9.72	3.32	0.44	0.05	98.64
VM7C	57.30	1.17	22.65	2.18	0.26	2.02	9.80	2.54	0.38	0.03	98.33
VM7C	54.62	0.91	24.08	2.73	1.56	0.90	12.96	0.94	0.50	0.00	99.20
VM7C	55.02	1.38	23.26	2.21	0.28	0.49	14.10	1.10	0.49	0.02	98.35
VM1	50.45	1.11	21.51	4.88	0.84	1.04	11.59	6.01	1.28	0.04	98.75
VM1	50.89	0.95	24.39	3.52	0.69	0.71	14.57	3.31	1.03	0.02	100.08
VM1	50.57	1.02	22.35	4.81	1.16	1.33	12.19	4.37	0.96	0.01	98.77
VM1	48.83	1.44	21.99	4.47	1.56	2.58	13.76	3.15	1.28	0.03	99.09
VM1	48.60	0.94	21.65	5.95	0.93	2.44	12.05	4.91	0.84	0.05	98.36

Table 2.8 (cont'd)

	SiO2	TiO2	Al2O3	FeO	MgO	CaO	Na2O	K2O	P2O5	F	total
VM1	49.36	0.98	22.38	4.30	0.91	3.02	14.24	3.56	1.18	0.05	99.98
VM1	49.47	1.28	21.28	5.94	1.10	1.94	12.09	5.45	1.06	0.00	99.61
VM1	49.48	1.53	23.88	3.95	0.82	0.90	14.68	3.64	0.66	0.00	99.54
VM1	48.50	1.52	20.22	6.70	1.19	2.23	12.50	4.45	1.87	0.06	99.24
VM1	48.54	1.20	20.37	5.66	1.29	2.21	9.07	9.29	0.90	0.06	98.59
VM1	48.55	1.60	20.08	5.63	4.72	2.12	13.77	1.29	1.29	0.05	99.10
VM2C	50.37	0.15	29.70	1.00	0.06	0.68	16.17	2.48	0.25	0.01	100.87
VM2C	57.38	0.96	22.61	2.25	0.42	0.50	7.15	6.40	0.76	0.08	98.51
VM2C	57.59	1.09	21.99	2.44	0.35	0.47	8.25	6.38	0.82	0.01	99.39
VM2C	57.01	1.17	22.83	2.58	0.44	0.48	7.50	6.17	0.43	0.00	98.61
VM2C	51.31	1.05	20.08	2.97	0.34	6.70	6.53	5.45	2.03	0.25	96.71
VM2C	56.83	1.10	22.03	2.61	0.35	0.61	7.45	6.35	0.81	0.00	98.14
XE02	52.93	0.56	22.81	3.02	1.08	3.06	13.49	3.36	0.58	0.03	100.92
XE02	51.94	0.15	26.88	1.42	0.44	1.73	15.87	2.66	2.33	0.05	103.47
XE02	52.60	0.55	22.62	2.83	0.56	3.53	13.22	3.04	0.24	0.10	99.29
XE02	49.33	1.54	16.47	5.82	2.10	6.78	12.21	2.01	0.59	0.13	96.98

Table 2.8 (cont'd)

	SiO2	TiO2	Al2O3	FeO	MgO	CaO	Na2O	K2O	P2O5	F	total
XE05	51.64	1.89	17.92	7.70	1.24	0.46	5.44	9.67	0.92	0.00	96.88
XE05	51.92	1.64	19.38	4.76	0.54	2.23	7.11	9.72	1.33	0.06	98.69
XE05	53.15	2.06	19.05	7.20	1.03	0.40	6.06	9.30	1.09	0.01	99.35
XE05	49.13	2.32	17.74	8.22	2.50	3.96	5.74	8.11	1.09	0.03	98.84
XE05	53.38	0.36	25.28	2.07	0.60	0.55	16.19	2.14	1.21	0.01	101.79
XE05	52.59	1.77	18.34	5.95	1.25	1.24	5.96	10.28	0.96	0.04	98.38
XE05	52.17	1.68	19.18	6.56	0.87	0.52	9.72	7.42	0.73	0.03	98.88
XE05	54.54	2.20	16.72	7.15	0.96	0.55	5.34	10.06	0.80	0.01	98.33
XE05	53.04	1.97	19.99	5.45	0.81	0.31	6.85	9.39	1.22	0.02	99.05
XE05	51.43	1.60	19.79	5.70	0.93	0.35	6.68	10.95	1.08	0.00	98.51
XE05	53.01	1.58	21.57	5.16	1.00	0.30	14.43	2.69	0.09	0.02	99.85

Table 2.8 (cont'd)

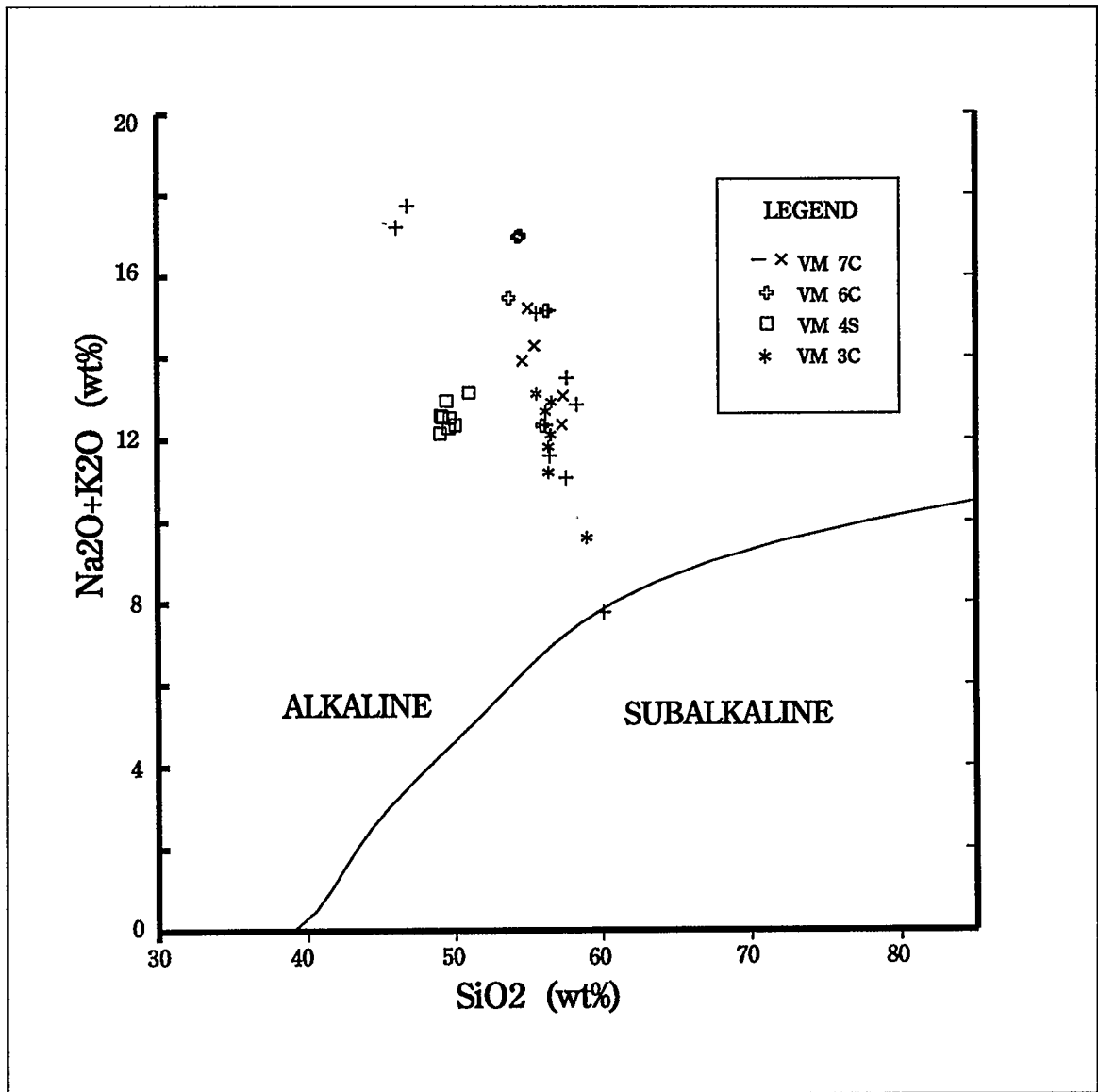


Figure 2.4

Alkali versus silica plot of the residual glass from the Volcano Mountain nephelinites, showing the chemical variation of the glasses consists mainly in the varying amounts of alkali.

The larger glassy pockets do not appear to have continuous compositional gradients near or away from microphenocrysts contained within them.

2.2.2 Xenoliths

OLIVINE

Xenolithic olivine compositions and number of ions based on 4 oxygens are reported on table 2.9 (a); compositions of the overgrowths at the edges of xenoliths are shown on table 2.9 (b).

Compositions are fairly constant, ranging between Fo_{90} and Fo_{87} ; CaO content is between 0.02 and 0.11 wt%. The olivine overgrowths of the grains Fo_{80} , and CaO ranges between 0.35 to 0.98 wt%.

PYROXENE

Two pyroxenes are present in all the xenoliths: diopsidic clinopyroxene and enstatitic orthopyroxene; an exsolved pyroxene was also observed in samples VM 7C, XE 25, XE 12A and XE 03. The compositions, number of ions based on 6 oxygens, and mole % end member contents are reported on table 2.10. Number of ions and end member contents were calculated using the program PX (rel. 3.0, Cebria, 1990), and the reported values for the end members are those based on the scheme by Lindsley and Andersen (1983). The values thus obtained were plotted on a pyroxene quadrilateral (figure 2.5) together with the compositional domain of pyroxenes from similar xenoliths

from San Carlos, Arizona. The composition of clinopyroxenes from the Skärgeard intrusion is also shown on figure 2.5 for reference.

The clinopyroxene is classified as diopside (Morimoto et al., 1990), and its composition is $Wo_{31-38}En_{59-61}Fs_{2-6}$. The orthopyroxene is enstatite (Morimoto et al., 1990) and its composition is $Wo_{0.9-1.4}En_{88-93}Fs_{5-10}$. The compositions of the two most abundant pyroxenes do not seem to change dramatically between samples; also, there is no compositional zoning within each grain in any sample.

The exsolved pyroxene observed in samples VM 7C, XE 25, XE 12A and XE 03 generally has diopside lamellae in an enstatite-rich host, although in XE-12A one grain had a diopsidic host and enstatite-rich lamellae. The range of compositions of the lamellae falls within that of the pyroxenes described above .

SPINEL

Brown, chromian spinel is present in these xenoliths. Average analyses and number of ions (based on 4 oxygens) are shown on table 2.11.

The Cr_2O_3 content ranges between 34 and 8.6 weight percent (table 2.11), and appears to be inversely proportional to the amount of Al_2O_3 present. Figure 2.6 illustrates where these samples plot in an Al, Cr+3, Fe+3 ternary diagram, as well as the domain of other spinel occurrences in ultramafic xenoliths from Western North America. The diagram in figure 2.6 was

generated with the program ANAL34 (Roeder, 1989). For the spinels in this study and in the reported samples from the literature (shown in figure 2.6) where the weight percent of Fe_2O_3 was not available, it was calculated with the program OXIDE (Ghiorso and Carmichael, 1980).

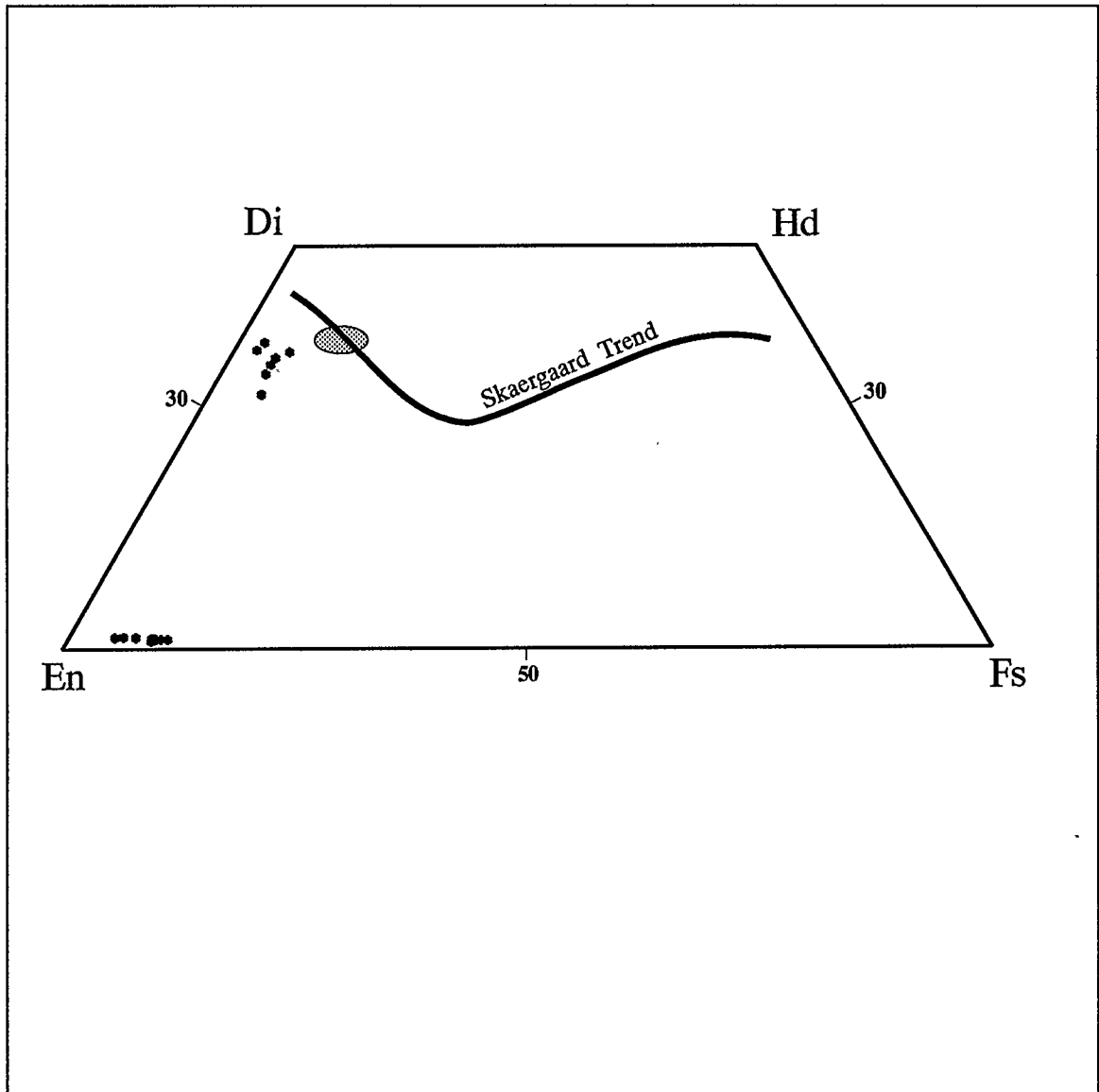


Figure 2.5

Pyroxene quadrilateral showing the compositional range of the xenolithic pyroxenes together with the compositional domain of the pyroxenes from the San Carlos lherzolites (Wilshire *et al.*, 1988). Endmember compositions were calculated according to the classification scheme by Linsley and Andersen (1983). The trend of the Skaergaard clinopyroxenes is also shown for comparison.

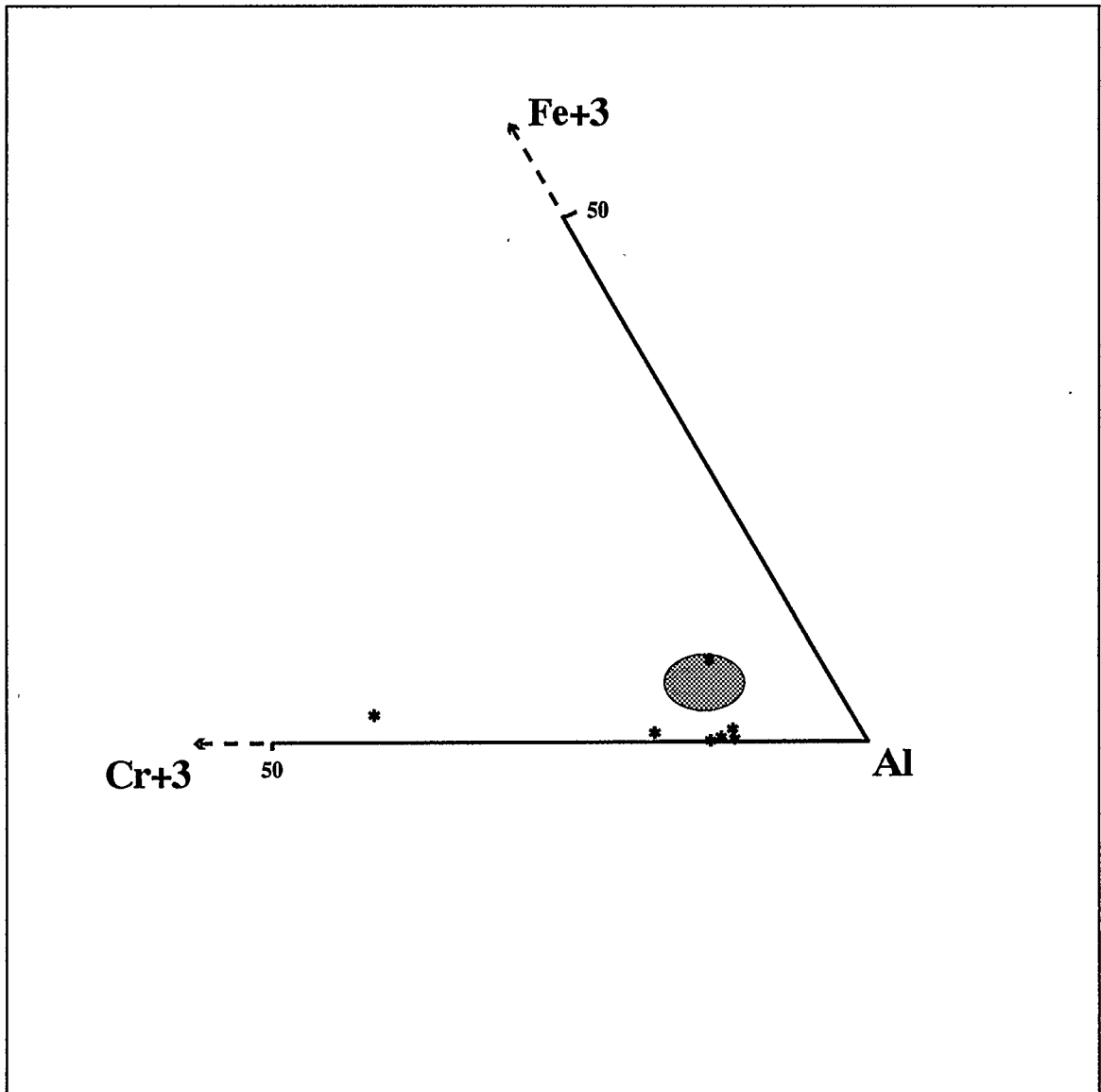


Figure 2.6

Ternary diagram showing the compositional range of the chromian spinels in the ultramafic nodules from Volcano Mountain. The diagram was generated by ANAL34 (Roeder, 1989).

2.9(a): Averaged microprobe analyses (in weight percent), number of ions and molar percent endmembers of olivines from ultramafic nodules; 2.9 (b): averaged microprobe analyses, number of ions and molar percent endmember compositions of olivine overgrowths around the nodules.

Table 2.9 (a)

	XE 01	XE 02	XE 03
SiO ₂	40.52	41.31	41.20
TiO ₂	<0.02	<0.02	<0.02
Al ₂ O ₃	<0.04	<0.04	<0.04
FeO	10.62	10.21	10.57
MgO	48.33	48.66	48.50
CaO	<0.01	0.02	0.03
Cr ₂ O ₃	<0.03	<0.03	<0.03
TOTAL	99.47	100.20	100.30

Number of ions based on 4 oxygens

Si	1.00	1.01	1.01
Fe+2	0.22	0.21	0.22
Mg	1.78	1.77	1.77
Sum	3.00	2.99	2.99

mol % endmembers

Fo	89.02	89.47	89.10
Fa	10.98	10.53	10.90

Table 2.9 (a) (cont'd)

	XE 06	XE 12B	XE 15
SiO ₂	41.03	41.06	41.28
TiO ₂	<0.02	<0.02	<0.02
Al ₂ O ₃	<0.04	<0.04	<0.04
FeO	10.01	9.64	10.57
MgO	49.23	49.08	48.50
CaO	0.08	0.03	0.02
Cr ₂ O ₃	<0.03	n.a.	<0.03
TOTAL	100.35	99.78	100.37

Number of ions based on 4 oxygens

Si	1.002	1.00	1.01
Fe+2	0.20	0.19	0.22
Mg	1.79	1.79	1.77
Sum	3.00	2.99	2.99

mol % endmembers

Fo	89.76	90.07	89.10
Fa	10.24	9.93	10.90

Table 2.9 (a)(cont'd)

	XE 25	VM 7C
SiO ₂	40.81	40.54
TiO ₂	<0.02	<0.02
Al ₂ O ₃	<0.04	<0.04
FeO	10.54	11.84
MgO	48.65	47.14
CaO	0.05	0.11
Cr ₂ O ₃	n.a.	<0.03
TOTAL	100.05	99.63

Number of ions based on 4 oxygens

Si	1.00	1.00
Fe ⁺²	0.21	0.24
Mg	1.78	1.74
Sum	3.00	2.99

mol % endmembers

Fo	89.16	87.65
Fa	10.84	12.35

Table 2.9 (b)

	VM7C	XE01
SiO ₂	38.76	39.21
TiO ₂	0.06	0.08
Al ₂ O ₃	0.17	0.08
FeO	20.74	17.36
MgO	39.02	42.44
CaO	0.51	0.41
Cr ₂ O ₃	0.03	0.06
Total	99.29	99.64
Number of ions based on 4 oxygens		
Si	1.01	1.00
Fe ⁺²	0.45	0.37
Mg	1.51	1.61
Ca	0.01	0.01
Sum	2.99	3.00
mol % endmembers		
Fo	77.04	81.31
Fa	22.96	18.69

Table 2.10

Composition (in weight percent), number of ions (based on 6 oxygens) and Wo-En-Fs endmember fractions of orthopyroxenes and clinopyroxenes from ultramafic nodules.

	XE 01		XE 02		XE 03	
	opx	cpx	opx	cpx	opx	cpx
SiO ₂	55.30	52.37	55.30	52.05	55.09	51.76
TiO ₂	0.11	0.58	0.09	0.59	0.13	0.51
Al ₂ O ₃	4.17	5.60	4.30	7.23	4.76	7.10
FeO	6.24	2.61	6.86	2.79	6.99	3.29
MgO	33.85	15.54	33.42	14.78	32.46	16.81
CaO	0.68	20.56	0.45	20.77	0.55	18.78
Na ₂ O	0.07	1.68	0.02	1.64	0.01	1.21
Cr ₂ O ₃	0.40	0.92	0.23	0.69	0.34	0.71
TOTAL	100.82	99.86	100.67	100.54	100.33	100.17
Number of ions based on 6 oxygens						
Si	1.89	1.90	1.90	1.87	1.90	1.86
Ti	0.00	0.02	0.00	0.02	0.00	0.01
Al iv	0.10	0.10	0.10	0.13	0.01	0.14
Al vi	0.06	0.14	0.07	0.18	0.09	0.16
Fe+2	0.18	0.08	0.20	0.08	0.20	0.10
Mg	1.73	0.84	1.71	0.79	1.67	0.90
Ca	0.02	0.88	0.02	0.80	0.02	0.72
Na	0.005	0.12	0.00	0.11	0.00	0.08
Cr	0.01	0.03	0.01	0.02	0.01	0.02
Sum	4.01	3.99	4.00	3.99	3.99	3.98

	XE01		XE02		XE03	
mol % endmembers						
Wo	1.42	37.87	0.93	35.91	1.15	31.35
En	91.46	59.32	90.04	59.12	88.20	62.94
Fs	7.12	2.82	9.03	4.97	10.66	5.71

Table 2.10 (cont'd)

	XE 06		XE 12B		XE 15	
	opx	cpx	opx	cpx	opx	cpx
SiO ₂	54.64	52.05	54.90	51.87	54.72	52.22
TiO ₂	0.10	0.46	0.10	0.48	0.10	0.49
Al ₂ O ₃	4.39	5.97	4.72	7.26	4.92	7.13
FeO	6.26	2.75	6.15	2.54	6.92	3.00
MgO	33.95	16.05	33.03	15.01	32.95	15.21
CaO	0.68	20.38	0.60	19.89	0.59	20.42
Na ₂ O	0.06	1.46	0.02	1.74	0.05	1.60
Cr ₂ O ₃	0.40	0.72	0.44	1.13	0.30	0.87
TOTAL	100.48	99.84	99.96	99.92	100.55	100.94

number of ions based on 6 oxygens

Si	1.88	1.88	1.89	1.87	1.89	1.87
Ti	0.00	0.01	0.00	0.01	0.00	0.01
Al iv	0.12	0.11	0.10	0.13	0.11	0.13
Al vi	0.06	0.14	0.08	0.18	0.08	0.17
Fe+2	0.18	0.08	0.18	0.07	0.20	0.09
Mg	1.74	0.87	1.70	0.81	1.69	0.81
Ca	0.02	0.79	0.02	0.77	0.02	0.78
Na	0.00	0.10	0.00	0.12	0.00	0.11
Cr	0.01	0.02	0.01	0.03	0.01	0.02
Sum	4.01	3.99	3.99	3.97	4.00	3.98

	XE06		XE12B		XE15	
mol % endmembers						
Wo	1.45	36.90	1.25	33.91	1.25	35.03
En	92.78	60.63	89.61	61.17	89.86	60.11
Fs	5.78	2.47	9.14	4.92	8.89	4.86

Table 2.10 (cont'd)

	XE 25		VM 7C	
	opx	cpx	opx	cpx
SiO ₂	56.37	53.46	55.58	51.87
TiO ₂	0.07	0.20	0.06	0.48
Al ₂ O ₃	2.76	4.24	3.87	7.26
FeO	6.61	3.06	6.45	2.54
MgO	33.25	16.03	33.09	15.01
CaO	0.60	20.62	0.55	19.89
Na ₂ O	0.06	1.22	0.14	1.74
Cr ₂ O ₃	0.38	1.36	0.45	1.13
TOTAL	100.10	100.19	100.19	99.92
number of ions based on 6 oxygens				
Si	1.94	1.93	1.92	1.87
Ti	0.00	0.00	0.00	0.01
Al iv	0.06	0.07	0.08	0.13
Al vi	0.06	0.11	0.07	0.18
Fe+2	0.19	0.09	0.19	0.08
Mg	1.71	0.86	1.70	0.81
Ca	0.02	0.80	0.02	0.77
Na	0.00	0.08	0.01	0.12
Cr	0.01	0.04	0.01	0.03
Sum	3.98	3.96	3.99	3.97
mol % endmembers				
Wo	1.19	36.64	1.13	33.91
En	88.89	57.24	89.49	61.17
Fs	9.92	6.13	9.38	4.92

Table 2.11

Average microprobe analyses (in weight percent) and number of ions (based on 4 oxygens) of chromian spinel from ultramafic nodules.

	XE 01	XE 02	XE 03	XE 06
TiO ₂	0.11	0.09	0.10	0.14
Al ₂ O ₃	56.99	59.32	57.74	56.36
FeO	10.55	10.93	11.76	10.14
MgO	20.65	20.60	20.51	20.54
Cr ₂ O ₃	11.56	8.62	9.25	10.73
TOTAL	99.86	99.56	99.36	97.91

number of ions based on 4
oxygens

Al	1.74	1.80	1.77	1.75
Fe+2	0.23	0.24	0.26	0.22
Mg	0.80	0.79	0.80	0.81
Cr	0.24	0.18	0.19	0.22
Sum	3.01	3.01	3.02	3.01

Table 2.11 (cont'd)

	XE 12B	XE 15	XE 25	VM 7C
TiO ₂	0.12	0.08	0.13	0.06
Al ₂ O ₃	52.19	57.87	34.52	53.17
FeO	10.86	11.33	15.11	12.10
MgO	20.11	20.57	16.86	19.80
Cr ₂ O ₃	15.20	10.62	34.01	14.89
TOTAL	98.48	100.47	100.63	100.02

number of ions based on 4
oxygens

Al	1.65	1.76	1.76	1.66
Fe+2	0.24	0.24	0.24	0.26
Mg	0.80	0.79	0.79	0.78
Cr	0.32	0.22	0.22	0.31
Sum	3.01	3.01	3.01	3.01

SECTION 3

3.1 P-T CONDITIONS AND PHASE EQUILIBRIA OF ULTRAMAFIC XENOLITHS

3.1.1 Thermometry

Three published geothermometers for spinel lherzolite assemblages usually applied to ultramafic nodules were used in this study to estimate the equilibrium temperature of the xenoliths. Two of the geothermometers use the Fe-Mg partitioning in coexisting pyroxenes in the reaction $Mg_2Si_2O_6$ (opx) \rightarrow $Mg_2Si_2O_6$ (cpx) (Wells, 1977, Mori, 1977), or between olivine and spinel, in $Mg_2Si_2O_6 + MgAl_2O_4 \rightarrow MgAl_2SiO_6 + Mg_2SiO_4$ (Mori, 1977); the third is an experimentally calibrated geothermometer by Lindsley (1983), shown in figure 3.1, which correlates the occurrence of orthopyroxene and clinopyroxene with temperature. Temperatures obtained are given below in table 3.1.

Wells (1977)	Mori (1977)	Lindsley (1983)
930°C	940°C (1) 1450°C (2)	900°-1100°C (see fig. 3.1)

Table 3.1.

Equilibrium temperatures of ultramafic xenoliths. The values reported represent an average of values obtained for each of the samples. All calibrations are $\pm 50^\circ\text{C}$. (1) indicates the temperature of the 2-pyroxene Fe-Mg exchange, and (2) is the cpx+spl \rightarrow oli+spl equilibrium temperature. Values obtained with Lindsley's geothermometer were calculated at a pressure of 15 kilobars.

These geothermometers were chosen because they employ different thermodynamic properties of the mineral phases or different univariant reactions to obtain the equilibrium temperature; this should theoretically yield a small temperature range which would constrain the equilibrium position of the xenoliths in P-T space given the mineral assemblage. However, the temperature range is wider than expected. The presence of a range in temperatures can be linked to problems in each of the geothermometers. The Wells geothermometer is the one most commonly used in the literature, and the values it yields are similar to published values for the Northern B.C. xenoliths (Nicholls *et al.*, 1982). However, the Fe-Mg exchange in pyroxenes, if there are other phases (for example oxides) that partition temperature-sensitive elements, is probably not the only factor to be affected by temperature, so a value obtained using a two-pyroxene geothermometer might not reflect exactly the equilibrium temperature for the entire assemblage. In addition, there have been no experimental calibrations of the Fe-Mg exchange which has had problems with its theoretical treatment (Fuji and Scarfe, 1982).

The first temperature listed using Mori's calibrations is essentially the same as the one obtained with Wells' calibration; however, the $\text{cpx} + \text{spl} \rightarrow \text{oli} + \text{spl}$ equilibrium calculation yields a much higher temperature, even though the two values should be similar if the mineral assemblage was in equilibrium. The textural disequilibrium observed in the spinel would indicate that at least between this phase and olivine it is not possible to make such an assumption,

and therefore the second value in Mori's geothermometer is not likely to reflect the equilibrium temperature at the mantle level where the xenoliths originated. Furthermore, this thermometer was calibrated using 'green' spinel (Mg-Al), whereas the rocks studied possess a more chromian ('brown') variety, and it involves the use of Al exchange, which is not a good indicator of temperature, unless the pressure is already known (Nicholls, 1977).

The range of values obtained with Lindsley's experimental two-pyroxene geothermometer was estimated from plotting the compositions of pyroxenes on the diagram in figure 3.1. The lines in this diagram mark the boundary of fields which describe the composition and presence of one or more pyroxenes for any given temperature as shown in figure 3.1(a). The temperature range was estimated to be above 900° but no higher than 1100°C, because the diopsides, although showing a wide range in composition, plot well within the 1100° and the 900°C fields, but the composition of the enstatites all fall between the 900°C boundary and the 1100°C boundary.

The samples do not contain any garnet or plagioclase in their mineral assemblage. This brackets the depth at which they were formed between 50 and 150 kilometers below the surface (equivalent to approximately 15 to 45 kilobars). For this depth the estimated isotherms of, respectively, a 'warm' and a 'cold' mantle range between 1250 and 800 degrees Celsius (Wyllie, 1984), which is within the range of temperatures obtained by using all three geothermometers.

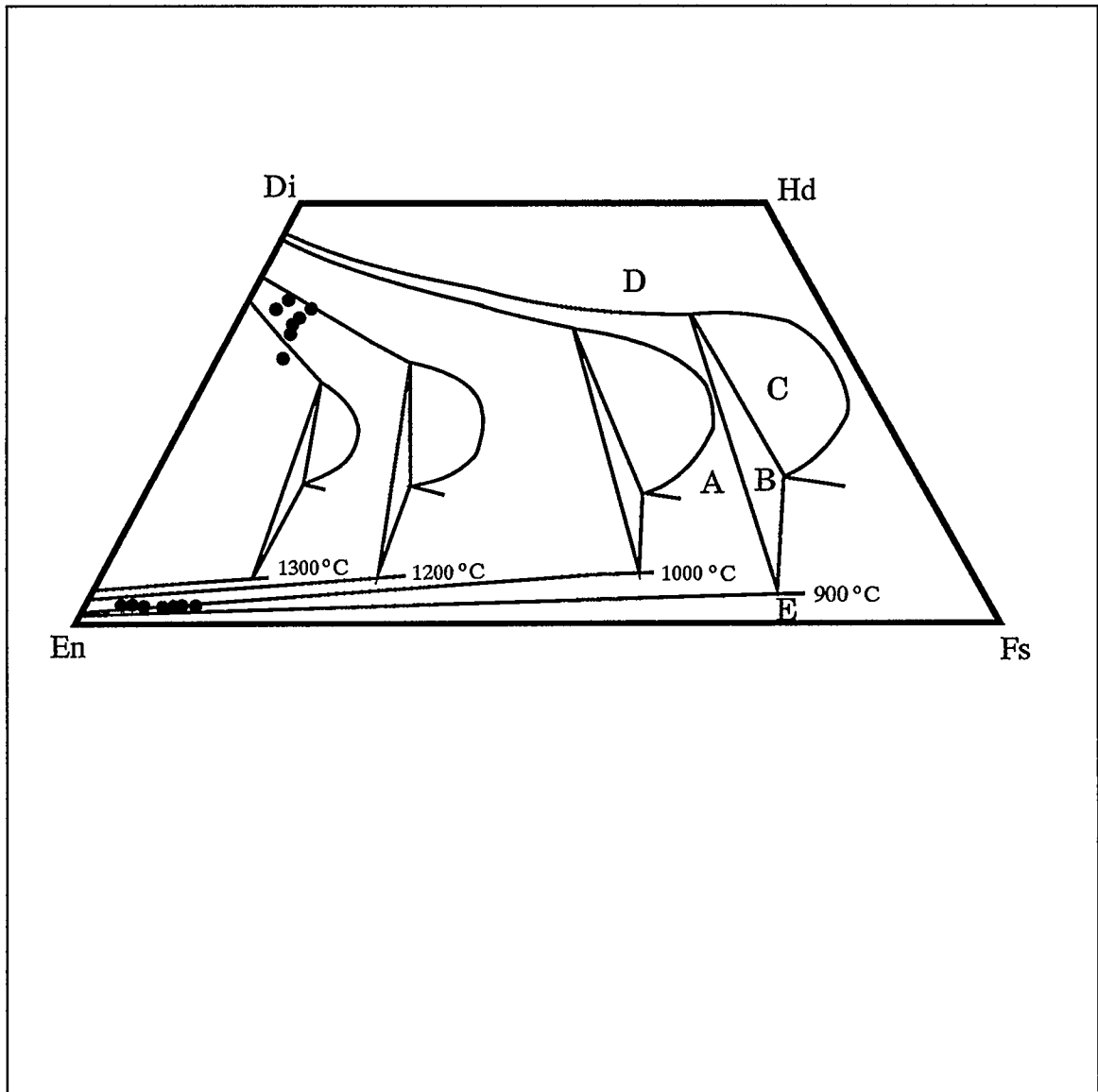


Figure 3.1

Two-pyroxene geothermometer by Lindsley (1983), at 15 kbar. The position of the xenolithic pyroxenes is shown by the filled circles. The five fields outlined by the curves, and shown for a temperature of 900°C, are as follows: A: augite + orthopyroxene; B: three pyroxenes; C: augite + pigeonite; D: augite only; E: orthopyroxene.

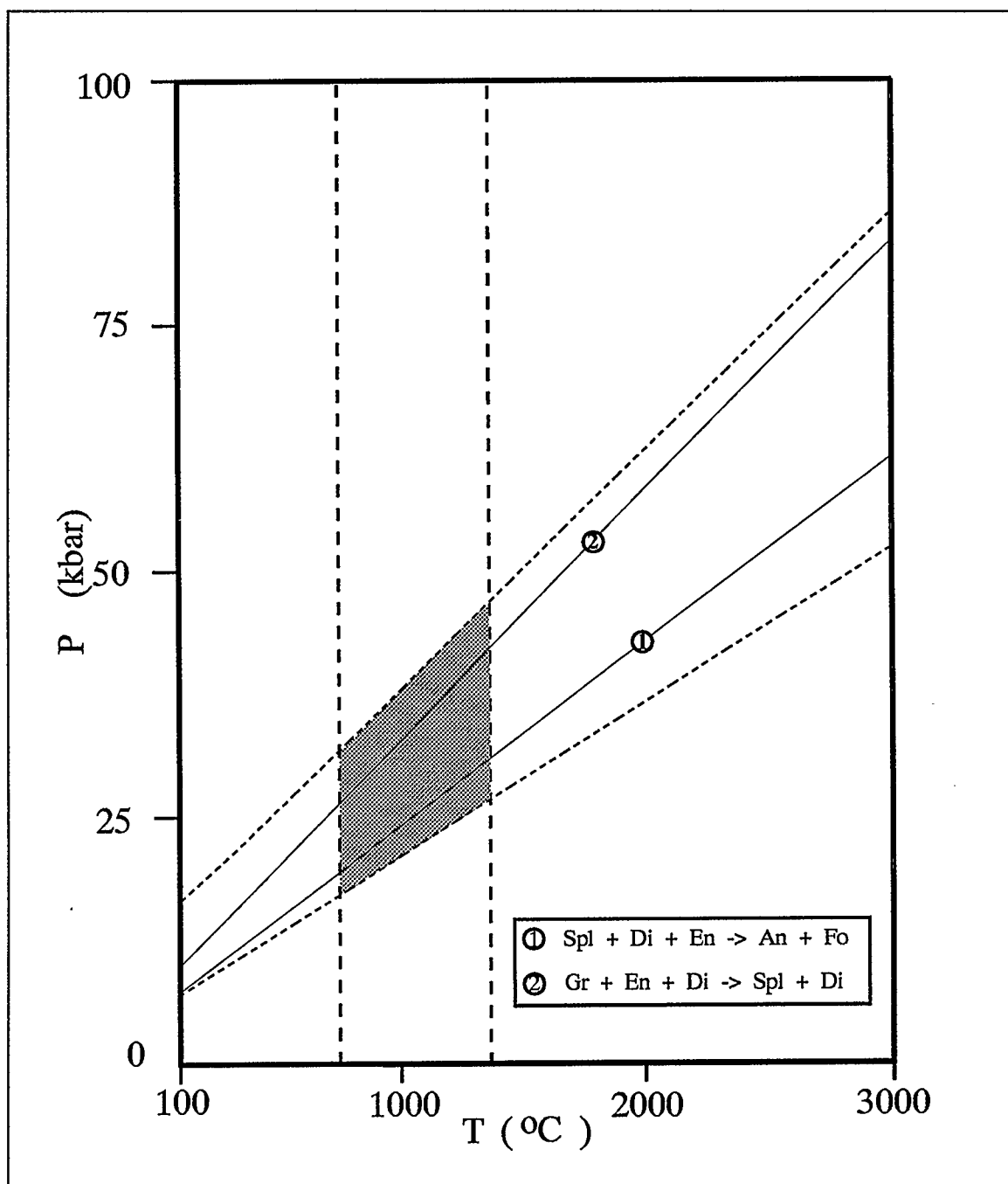


Figure 3.2

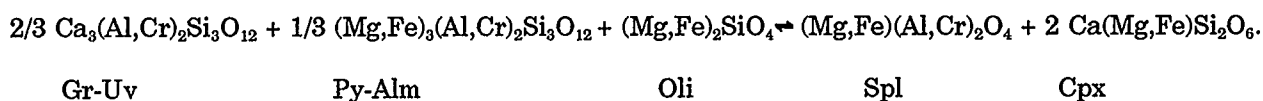
Position in P-T space of the reaction curves modeled in the CMAS system, as outlined in the text. The vertical dotted lines represent the temperature estimates from the geothermometry calculations. The finer dashed lines show the position of the curves for $\ln K = 0.87$ for the reactions, assuming ideal mixing for these phases.

3.1.2. Phase equilibria

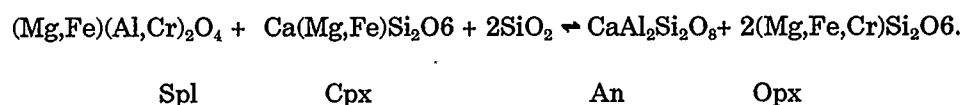
Chromian spinel often appears to be in textural disequilibrium with the other phases and to be found mainly in the vicinity of pyroxene grains, rather than olivine which seems to occur only as reaction rims around some spinel grains. This textural evidence suggests that chromian spinel is probably a product of the response of the system to changes in P-T conditions.

The lack of either garnet or plagioclase in the mineral assemblage would indicate that these xenoliths belong to P-T conditions within the spinel peridotite field (figure 3.2).

A balanced reaction which from garnet and olivine produces spinel and clinopyroxene, and which involves all the phases present can be written as follows:



An analogous reaction can be written for spinel and clinopyroxene to produce plagioclase and orthopyroxene, if introduction of SiO_2 is assumed, as follows:



Since thermodynamic data are more readily available for the Mg-rich endmembers, univariant curves defining the stability fields of anorthite, forsterite, spinel, enstatite, diopside and grossular were modeled in the system $\text{CaO-MgO-Al}_2\text{O}_3\text{-SiO}_2$ (CMAS). The position in P-T space of the equilibrium curves in the CMAS system were calculated using thermodynamic data from

Berman (1988). A slight shift of the curves has to be allowed for, due to the Fe-Mg exchange in the olivine and pyroxene solid solutions. Figure 3.2 illustrates the position of these curves; the vertical dotted lines represent the temperature range obtained from geothermometry in section 3.1.1; the finer dashed lines are the positions of the curves when the natural logarithm of K, the reaction constant, is equal to 0.87, assuming ideal mixing for the phases considered.

The field of stability of spinel + 2 pyroxenes in fig 3.2 appears to span quite a wide range of pressures and temperatures, but if the temperature range obtained from the geothermometry is acceptable, it restricts the pressure range approximately to between 20 and 45 kilobars, as indicated by the shaded area between the two vertical lines. This range of pressures would agree with experimental results obtained for phase assemblage transitions with changing pressure in peridotitic rocks (MacGregor, 1967, fig.12.1). Once the pressure range has been defined, it is possible to better constrain the temperature of the xenoliths by using the pressure range and the phase assemblage. This locates the position of the Yukon xenoliths in the divariant field in P-T space, shown as the shaded area on figure 3.2.

3.2 CLASSIFICATION AND COMPARISON OF ULTRAMAFIC XENOLITHS

Samples were compared for textures and composition to xenolithic nodules of similar provenance from the Canadian Cordillera (Fuji and Scarfe, 1982; Nicholls *et al.*, 1982; Ross, 1983) and San Carlos, Arizona (Wilshire *et al.*,

1988) in order to determine if the xenoliths in this study represent mantle conditions more similar to the B.C. or the Arizona samples, because the samples from Volcano Mountain can be considered as part of the same trend in Western North America. San Carlos diopsidic lherzolites are often found in association with or cut by 'composite' xenoliths, veins and patches of pyroxenites or pyroxene-rich lherzolites. The pyroxenites contain hydrous minerals, usually taken as evidence for the passage of metasomatic fluids (Ulmer *et al.*, 1987). Hydrous phases and similar cross-cutting relationships were not observed in the xenoliths from this study, and only one occurrence of amphibole has so far been cited in xenoliths from Western Canada (Brearley, 1982).

3.2.1 Textural comparison

The xenoliths from Volcano Mountain show features which would suggest solid state flow in the portion of the upper mantle where they originated: exsolution lamellae in pyroxenes, undulose extinction, sub-grain polygonal boundaries, curvilinear grain boundaries and kink bands in olivine. This reflects a greater textural and deformational similarity to the San Carlos lherzolites than to the Western Canadian xenoliths.

A study by Ross (1983) on the stress regime of the upper mantle in the Canadian Cordillera identifies four different types of textures occurring in the xenoliths throughout Western Canada, based on increasing deformation, which

translates into decreasing grain size and generally decreasing temperatures: protogranular, porphyroclastic, equigranular, and poikiloblastic. These textures correspond to different stress-temperature regimes and are interpreted to represent different parts of a mantle plume convecting through a stratified mantle section underneath the Canadian Cordillera.

The type of texture that would match the xenoliths described in this study is the "protogranular" texture. However, the grain size of the Yukon xenoliths is somewhat smaller than that reported by Ross for protogranular rocks elsewhere in British Columbia. Furthermore, the exsolution lamellae in pyroxenes of other Canadian localities seem to occur only in highly sheared rocks.

Xenolithic samples from a nearby cinder cone in the Yukon River valley are reported to have mostly protogranular texture, although in some samples the texture grades to porphyroclastic. Temperatures given by Ross (1983) for the xenoliths are obtained using stress regimes and an estimate of the location of isotherms at depth. The protogranular xenoliths from the Yukon River in Ross' study fall between the 1300° and 1000°C (50-80 km.) isotherms. Such a temperature range, although it overlaps that found for the xenoliths by geothermometry in section 3.1, it extends to temperatures that seem anomalously high given the mineral assemblage for the Volcano Mountain samples.

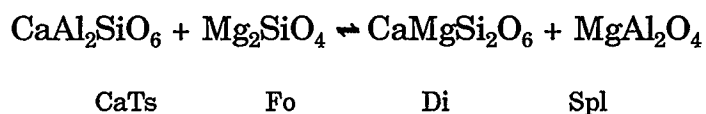
Of the two sets of xenoliths they were compared to, those from San Carlos show similar protogranular texture and grain size, although the deformation in the latter samples can also be more intense (Wilshire *et al.*, 1988); samples from Western Canada appear to be mostly finer grained (equigranular to poikiloblastic) and to have preferred orientation of mineral grains (Ross, 1983).

The textural disequilibrium features observed at the rims of spinel grains have not yet been described for either the San Carlos xenoliths, or for any nodule occurrence in British Columbia, although symplectic overgrowths of pyroxene and spinel have been reported (Ross, 1983).

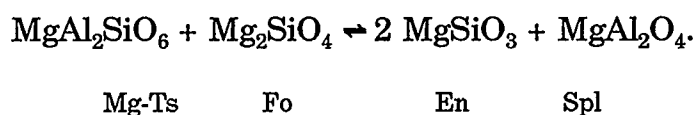
3.2.2 Compositional comparison

Analyses of the mineral phases were compared, with particular attention to any variations of the components that could be an indication of equilibration under different P-T conditions.

Lower aluminium content in pyroxenes can be taken as an indication of a lower pressure regime, if the activity of silica and the temperature are constant (Nicholls, 1977). Solution of Al_2O_3 in pyroxenes of a four-phase spinel peridotite in the SiO_2 -CaO-MgO- Al_2O_3 system can be thought of as the result of a combination of the following reactions, which proceed to the right with increasing pressure, everything else being constant (Wyllie, 1970, Herzberg, 1983):



and



As mentioned, pressure is not the only factor contributing to a change in Al_2O_3 in pyroxenes and spinel: temperature or bulk composition variations could also affect the solubility of Al_2O_3 in pyroxenes. In any case, a different Al_2O_3 content would suggest differences in the P-T-X regime of the xenoliths in this study and between these and the other two sets of xenoliths examined.

The major components of olivine, pyroxenes and spinel, SiO_2 , FeO , MgO and CaO are very similar between all groups. There does not appear to be any significant difference in Al_2O_3 content of pyroxenes between the xenoliths from the Yukon and the samples from B.C. The San Carlos xenoliths have considerably lower Cr_2O_3 in both pyroxenes than any of the B.C. or the Yukon samples, and since Cr_2O_3 and Al_2O_3 can substitute for one another as endmembers of a solid solution, a comparison for Al_2O_3 between pyroxenes with different Cr_2O_3 content is not completely legitimate.

The Cr_2O_3 and TiO_2 content in pyroxenes and chromian spinels is more similar to the samples from Atlin Lake and Northern Itcha Mountains

(Nicholls *et al.*, 1982) than those from San Carlos. The difference is especially pronounced between this study's and San Carlos' Cr_2O_3 content in diopside and spinel, the Arizona samples being richer in TiO_2 . The abundance of Cr in these rocks seems to be related to a deep-seated origin, as chromium content usually decreases with decreasing depth (Ross, 1983).

A possible explanation of the discrepancy between the Cr_2O_3 and TiO_2 distribution could be given by invoking inhomogeneity in mantle fluid distribution with respect to these minor components, perhaps reflecting either a different oxidation state, or the presence, in the San Carlos xenoliths, of metasomatic fluids, enriched in TiO_2 . Differences in mantle fluids composition would be a consistent hypothesis with the large geographic distance between the sample locations.

3.2.3 Discussion

Similarities were found between the xenoliths in this study and the two sets used for comparison: the texture resembles that of the San Carlos xenoliths, but the chemical composition shows more affinities with the samples from Western Canada. Neither of these common traits alone, however, is sufficient to unequivocally compare the Yukon xenoliths to one or the other occurrence. The mineral assemblage in these xenoliths also seems to be different, in that they do not possess garnet, like the Arizona samples, and the composition of the spinel present is far more chromian than any of the other

samples, including the chemically more similar samples from British Columbia. For these reasons, and because of the estimated pressure and temperature values given in section 3.1, it is possible that the ultramafic nodules from Volcano Mountain may represent a different portion of the upper mantle than that sampled in the Arizona or the B.C. nodules.

It is not possible, given the paucity of data on composition and properties of the upper mantle, to say with certainty whether the difference in the xenoliths studied here is merely due to a variation in depth or temperature, or if it is legitimate to interpret such a diversity as the result of large-scale mantle inhomogeneity such as a plume. In any case, the fact remains that the Yukon xenoliths appear to be chemically, texturally and mineralogically dissimilar from the other occurrences reported in the literature.

SECTION 4

4.1 CLASSIFICATION OF VOLCANO MOUNTAIN LAVAS

Bulk rock wet chemical analyses of four lavas were done by J. Nicholls. Their weight percent normative compositions are reported on table 4.1. The lavas analyzed were chosen to be representative of the three flows mapped and shown on figure 1.2.

The whole rock chemistry and normative compositions are very similar in all samples, thus in the bulk rock, the chemical diversity is less than in the residual glasses. A plot of the bulk rock analyses in the MacDonald and Katsura (1970) diagram for the classification of volcanic rock suites shows the decidedly alkaline character of the lavas (Figure 4.1). Their most striking feature is revealed in the normative composition as the overwhelming abundance of nepheline, which, when plotted on the Irvine and Baragar (1971) classification diagram for Na-rich alkaline volcanic rocks, places the samples well into the nephelinite field (fig. 4.2). All the samples have quite high amounts of Fe_2O_3 , which enhances the abundance of nepheline in the norm calculations. Another distinctive feature of the lava flows from Volcano Mountain is their low MnO content, uncommon for such oxidized samples. Phosphorus values are also quite high when considering the apparent lack of apatite.

The whole rock analyses from Volcano Mountain were compared to nephelinite basanites and basalts from Hawaii (Winchell, 1948) and to the

SAMPLE	VM 01	VM 6C	XE 05	XE 11
SiO ₂	41.16	41.95	40.40	40.30
TiO ₂	3.04	2.92	3.08	3.08
Al ₂ O ₃	10.84	11.28	10.58	10.58
Fe ₂ O ₃	4.31	3.82	4.86	4.73
FeO	8.96	9.10	9.06	9.07
MnO	0.02	<0.01	0.03	0.04
MgO	11.59	11.31	11.60	11.84
CaO	8.97	8.98	8.77	8.49
Na ₂ O	4.87	4.61	4.84	4.99
K ₂ O	2.21	1.67	2.31	2.32
P ₂ O ₅	1.26	1.04	1.22	1.29
TOTAL	97.47	97.01	97.33	97.18
Or	13.06	9.87	13.65	13.71
Ab	2.05	7.69	0.55	0.08
An	1.19	5.15	0.32	0.00
Ne	21.21	16.96	21.89	22.44
Ac	0.00	0.00	0.00	0.63
Wo	14.65	13.47	14.70	14.07
En	10.47	9.42	10.59	10.10
Fs	2.87	2.92	2.78	2.71
Fo	12.89	13.14	12.82	13.59
Fa	3.89	4.49	3.71	4.02
Mt	6.25	5.54	7.05	6.54
Il	5.77	5.55	5.85	5.85
Ap	2.98	2.46	2.89	3.06

Table 4.1

Whole rock analyses and CIPW normative compositions of the Volcano Mountain lava flows.

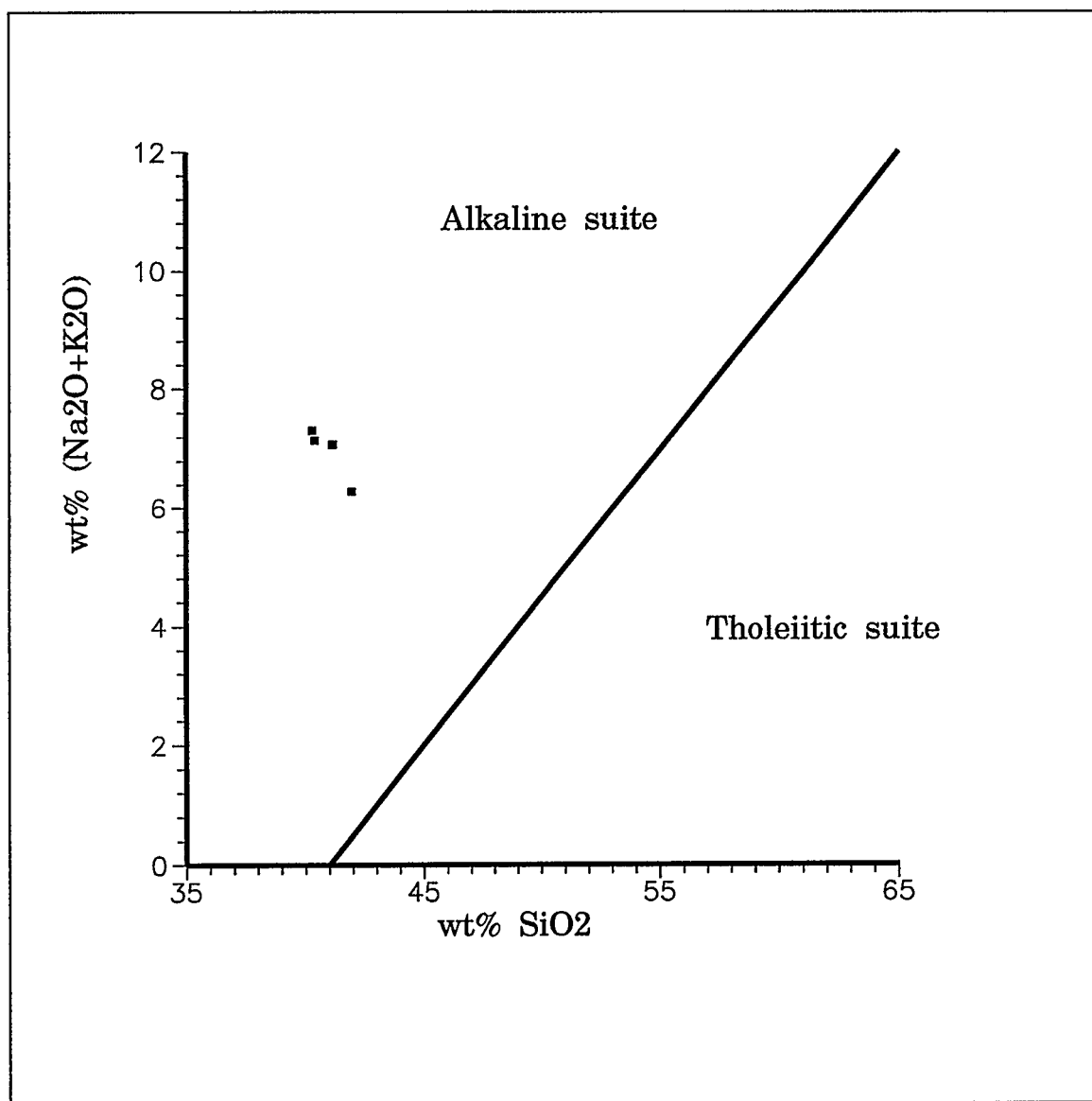


Figure 4.1

Analyses of Volcano Mountain lava flows (black squares) plotted on MacDonald and Katsura's (1962) alkali versus silica diagram for tholeiitic and alkaline rocks.

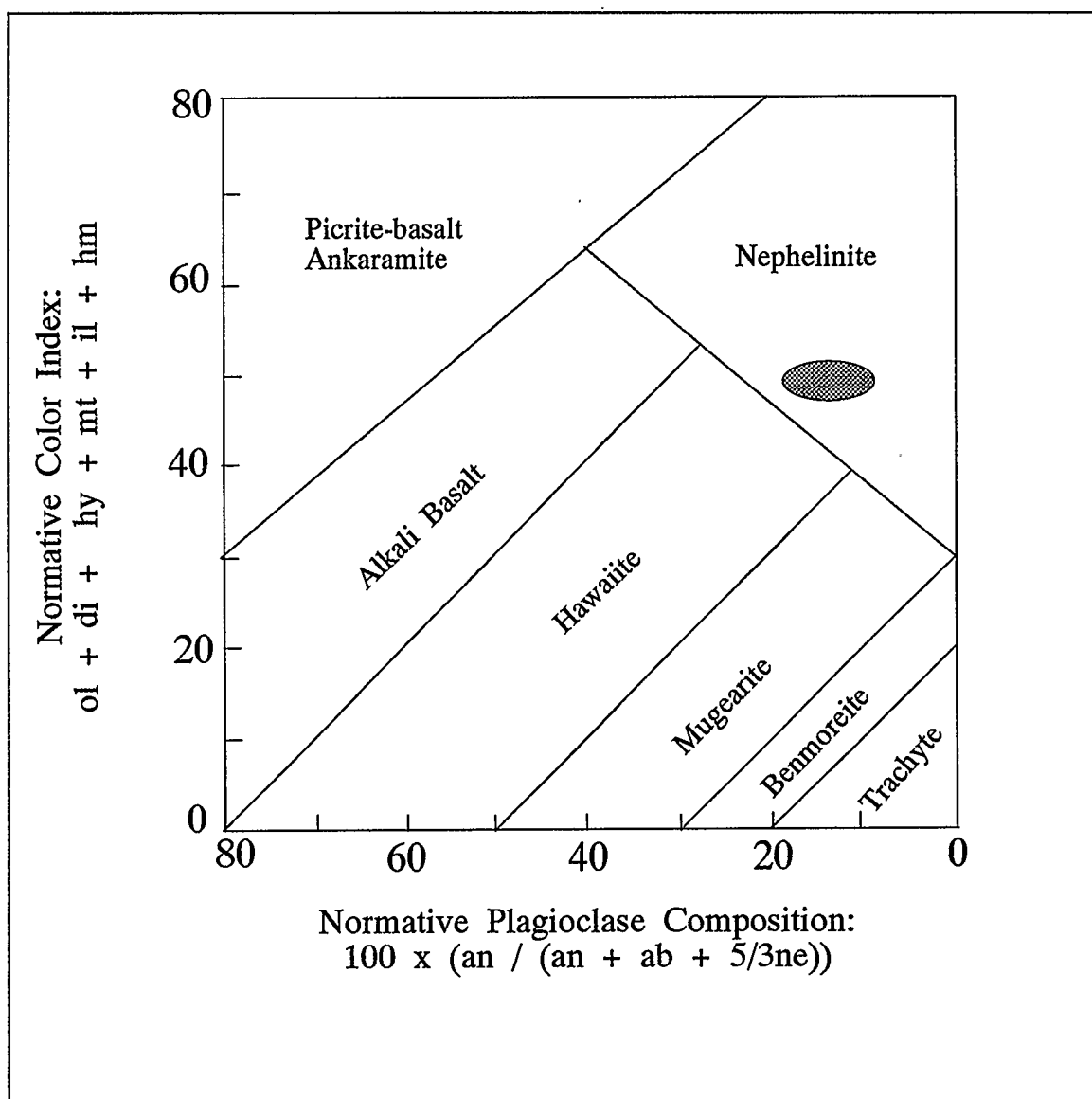


Figure 4.2

Classification of Na-rich alkaline rocks (after Irvine and Baragar, 1971) showing the compositional domain for the lavas from Volcano Mountain. Normative compositions are given in mole percent.

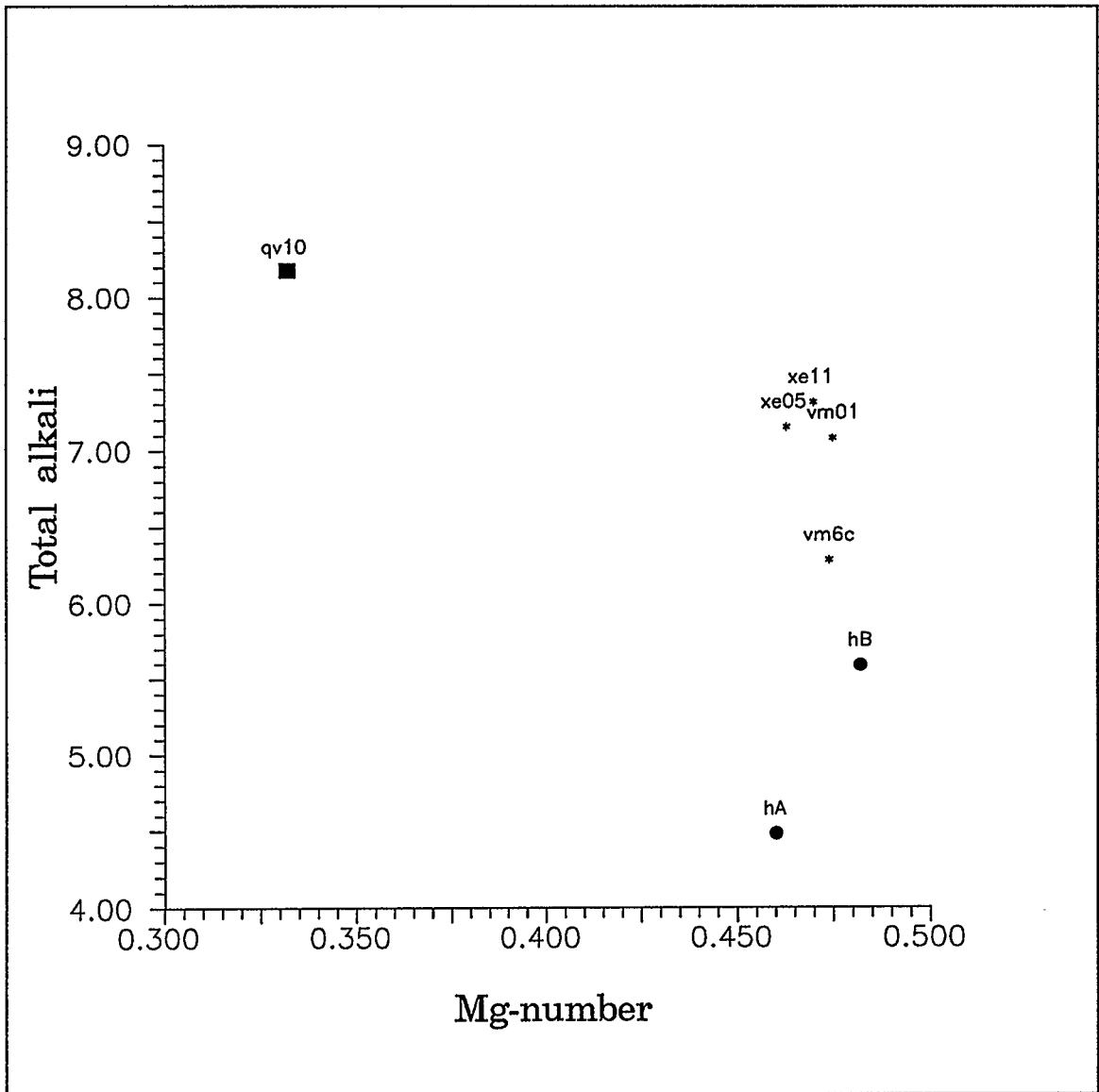


Figure 4.3

Mg-number ($\text{MgO}/(0.8998\text{Fe}_2\text{O}_3+\text{FeO}+\text{MgO})$) versus total alkali ($\text{Na}_2\text{O}+\text{K}_2\text{O}$) diagram, showing the position of the Volcano Mountain lavas relative to the nephelinite (gv-10) described by Fiesinger (1975), shown as the filled square, and to the nepheline basanite (hA) and nepheline basalt (hB) from Hawaii (Winchell, 1948), shown as filled circles.

other occurrence of nephelinites in the Canadian Cordillera (Fiesinger, 1975). The Mg-number ($\text{MgO}/(0.8998\text{Fe}_2\text{O}_3+\text{FeO}+\text{MgO})$) was plotted versus total alkali ($\text{Na}_2\text{O}+\text{K}_2\text{O}$) for this comparison, and the plot is shown on figure 4.3. The nephelinites from Volcano Mountain are more alkaline than the Hawaiian samples even though they have similar Mg-numbers.

4.2 CHEMICAL VARIATION OF LAVAS AND RESIDUAL GLASSES: PEARCE ELEMENT RATIOS.

4.2.1 Introduction

Element variation diagrams provide a relatively quick and easy visual method to estimate chemical changes caused by differentiation in rock suites and within rocks of the same suite.

Harker-type diagrams are the most widely used, but since they plot oxide concentrations directly against each other (intensive variables), the correlation between weight percent and mineral phases is not immediately obvious and does not necessarily reflect in a straight forward manner the chemical variations in terms of observed petrologic characteristics.

Pearce plots, because they use ratios of elements in the rocks, are equivalent to comparing masses of oxides (extensive variables) to each other and thus they provide a more powerful tool for characterizing the chemical changes and explain them in terms of mineral chemistry (Russell and Nicholls, 1988). Tests for comagmatism in members of the same rock suite, and chemical

variations due to the crystallization of one or more mineral phases in basaltic rocks are the most common uses of Pearce Element Ratios (for example, Russell and Nicholls, 1988). Other hypotheses that can be tested are rock alteration processes (Fowler, 1990), and trace element test of comagmatism (Russell and Halleran, 1990). To test all these hypotheses it is necessary to determine: a) the presence of one or more conserved element(s) (*ie.* the element(s) that did not take part in the sorting process), and b) the element coefficients that best represent the stoichiometry of the mineral phases present in the rocks studied. The conserved element is the denominator in Pearce diagrams, and usually the sum of two or more 'non-conserved' elements constitute the numerators.

A comagmatic origin for rocks in the same suite (or between different rock suites) can be recognized in two ways: if the rock suite has more than 2 conserved elements (for example K, P, and Ti), then a plot of the ratios of two of these elements over a common denominator (the third conserved element) yields a tight cluster if the rocks came from the same magma batch (Russell and Nicholls, 1988, fig 2), since the conserved element ratios are constant. For non-comagmatic rock suites, the clusters plot in different parts of the diagram. If there are less than three conserved elements, then a crystal differentiation diagram (Russell and Nicholls, 1988, fig.3) will show non-comagmatic suites as points on different lines of equal slope (provided they crystallized a common phase assemblage) but different, non-zero intercepts. If the comagmatic

hypothesis cannot be rejected, then it is meaningful to examine what phases affected crystallization in the suite. Stanley and Russell (1989) have established a methodology based on matrix algebra to select the axes coefficients that reflect crystallized phases in the rocks. A set of computer programs (PRATIO, PEARCE* and AXIS*), based on these rules, have also been written (Nicholls, 1990 and Stanley and Russell, 1989, respectively). These programs were used in determining the most appropriate ratios for the samples discussed below.

In this section, Pearce Element Ratios are used with bulk rock compositions to test for comagmatism of the three flows and crystallization of the observed mineral assemblage of olivine pyroxene, oxides, leucite and nepheline. The residual glass compositions are also plotted in order to test whether despite the wide variation of chemical compositions, all the glass patches from the same rock could be said to have derived from crystallization of the same phases. For samples VM 01 and XE 05 as well as for VM 6C the analyses of residual glasses were plotted together with their bulk compositions to check for P conservation.

Data points in figures 4.5(a) and (b) through 4.7 are shown with their error ellipses. Each ellipse defines a contour of equal probability that the data point lies within that ellipse, according to the analytical uncertainties used for the variables in the ratios (Mayer, 1975). The analytical uncertainties in this case are those related to probe analyses (Nicholls and Stout, 1988).

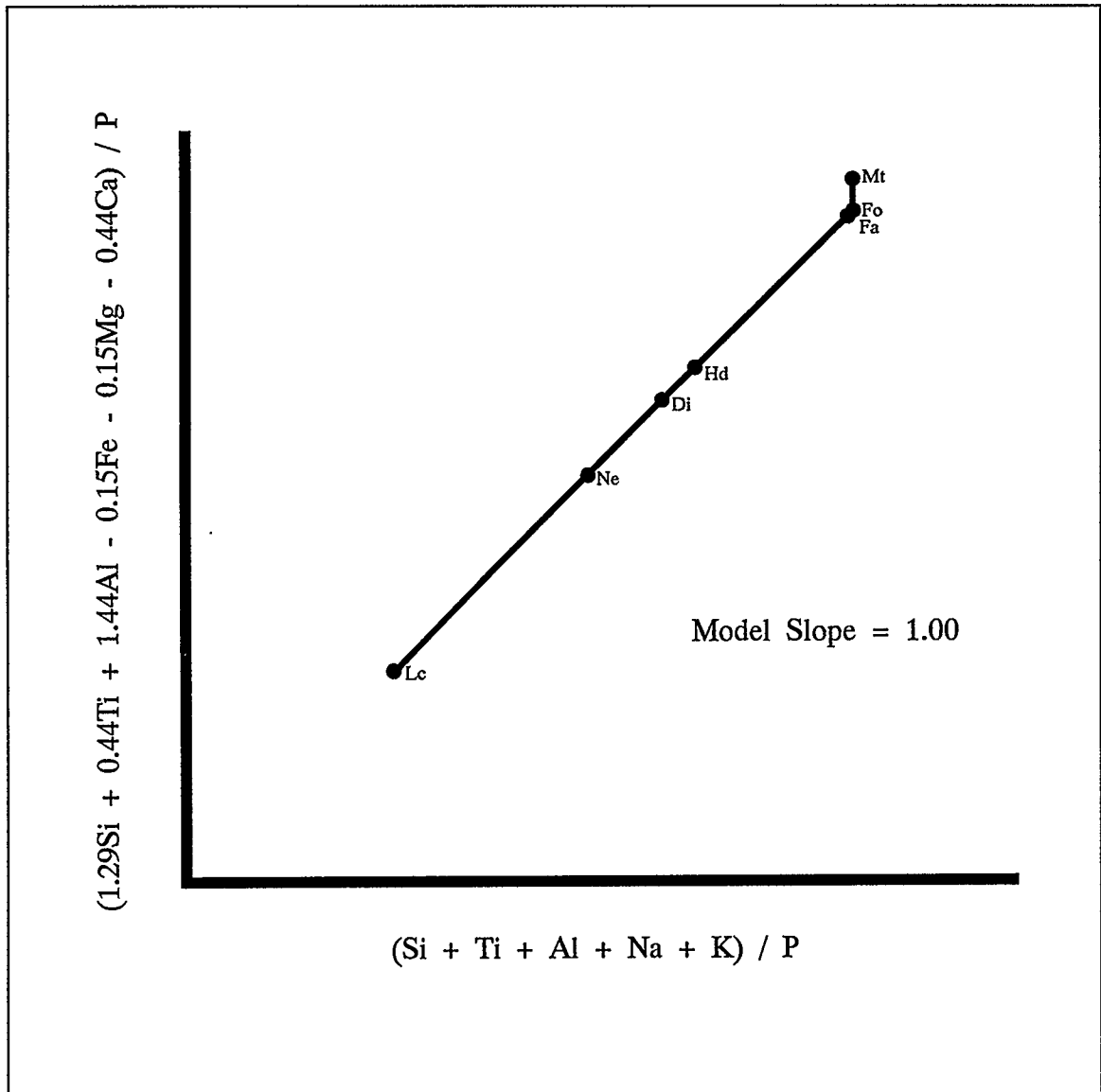


Figure 4.4

Phase displacement vector showing all constituent phases (except magnetite) falling on a line with a slope of 1.00. Numerator coefficients were generated by using the phase composition matrix of table 4.2.

	Si	Ti	Al	Fe	Mg	Ca	Na	K	P
CO	1.010	0.000	0.000	0.317	1.653	0.006	0.000	0.000	0.000
RI	1.015	0.000	0.000	0.442	1.512	0.011	0.000	0.000	0.000
P1	1.690	0.110	0.350	0.270	0.660	0.860	0.070	0.000	0.000
P2	1.810	0.070	0.230	0.240	0.730	0.870	0.050	0.000	0.000
AP	0.000	0.000	0.000	0.000	0.000	5.000	0.000	0.000	3.000
UP	0.000	1.000	0.000	2.000	0.000	0.000	0.000	0.000	0.000
MT	0.000	0.000	0.000	3.000	0.000	0.000	0.000	0.000	0.000
LC	1.978	0.023	0.941	0.068	0.015	0.023	0.019	0.938	0.000
NE	1.150	0.000	0.840	0.015	0.005	0.022	0.692	0.090	0.000

Table 4.2

Phase composition matrix used to produce figure 4.3. Only the phases used in the calculations are shown. The stoichiometric proportions of the mineral phases were taken from sample VM 7C, but using the cation ratios of other samples does not seem to affect the result appreciably. Abbreviations: CO: olivine composition in the core; RI: olivine composition in the rim; P1: high-Ti diopside; P2: low-Ti diopside; AP: apatite; UP: ulvöspinel; MT: magnetite; LC: leucite; NE: nepheline.

4.2.2 Whole rock plots

Because these glasses are the residual from crystallization of four or five phases (olivine, pyroxene, nepheline, leucite and oxides), the choice of conserved elements was limited to one, phosphorus, since no apatite could be positively identified in the samples analyzed by probing or by point counting techniques. Detection of apatite was made problematic because phosphorus was not analyzed when point counting, and thus spots with high calcium counts could be either calcite or apatite.

Figure 4.4 shows a "phase displacement vector" plot with all the crystallizing phases (except magnetite) falling on a line with a slope of 1. This

diagram illustrates the displacement of the unit molar vector caused by sorting of the minerals present in the lavas as groundmass or phenocrysts. The numerator coefficients were chosen so as to have all the phases plotting on a line with a set slope, in order to visualize immediately if the hypothesis tested (ie. the crystallization of those phases) was valid or not. The phase composition matrix used to produce figure 4.4, shown in table 4.2, takes into account the real average composition of the minerals present, in an attempt to reduce the scatter in data distribution produced when end member compositions are used.

A certain degree of scatter is observed in all the Pearce plots produced from the data available. The causes of such scatter are usually attributed to three main reasons (Nicholls, 1990): problems with mineral stoichiometry, analytical uncertainties, and the element in the denominator not being completely conserved. The phase displacement matrix was designed to minimize the problems with the stoichiometry, usually related to presence of complex solid solutions of several end members rather than simple solutions of two or three end members in the mineral phases. The error ellipses plotted around each data point should account for the scatter due to analytical uncertainties. Magnetite will cause vertical deviations from the model line, and this could contribute to the scatter, but the samples do not possess a high modal abundance of oxides. The only real reason for scatter in the residual glass plots is that phosphorus is not completely conserved.

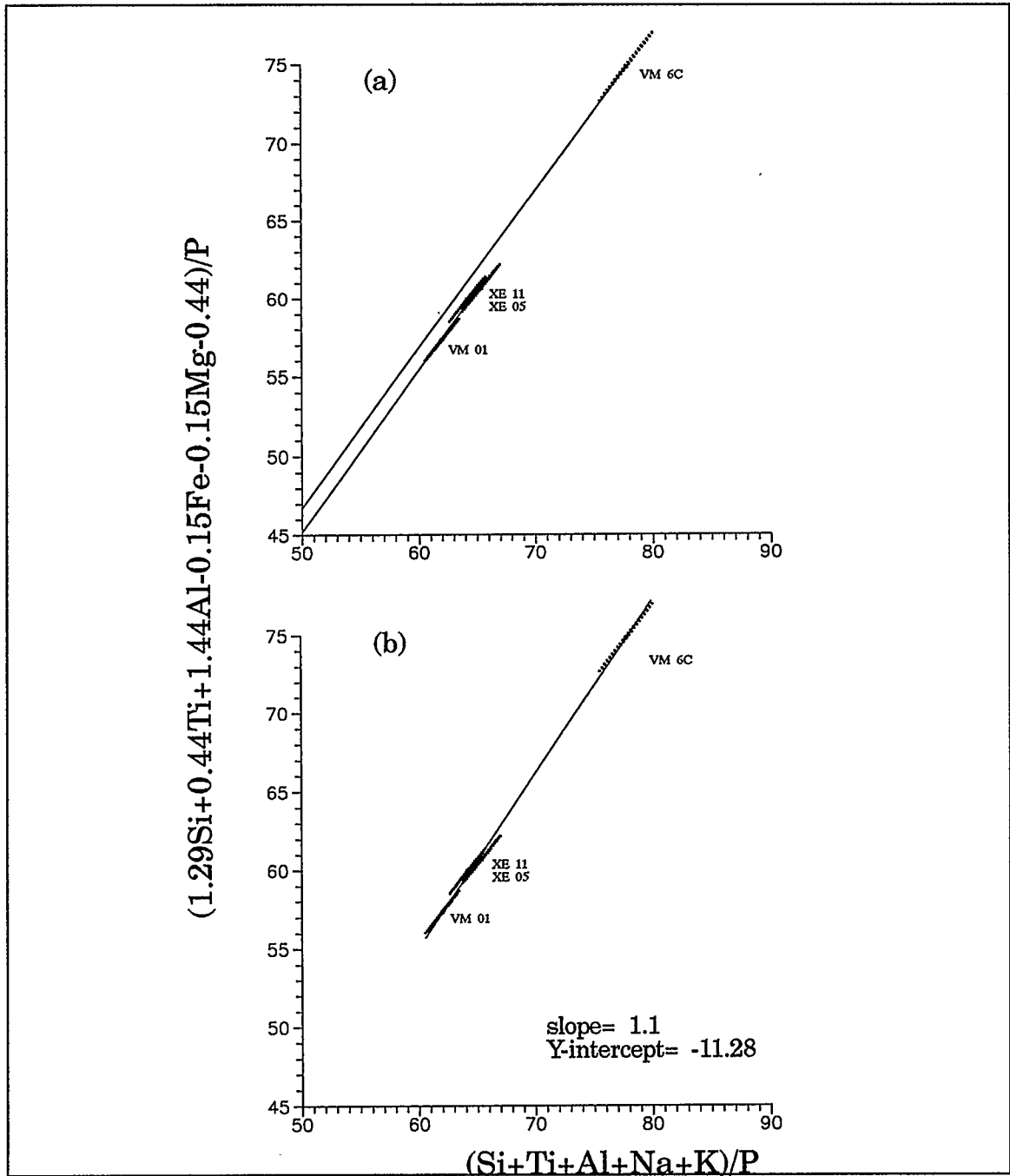


Figure 4.5

Crystal differentiation plots for rock compositions of samples VM 01, VM 6C, XE 05, and XE 11. 4.5(a) shows that a line with the slope of 1 through VM 6C does not intersect the other data points; 4.5(b) shows the same diagram with a best fit line with slope of 1.1 through all the points.

It was not possible to test for comagmatism in the rocks from the three different flows using a conserved element plot, so the rocks were plotted in a crystal differentiation plot as shown on figure 4.5(a) and 4.5(b). Figure 4.5(a) shows that a line with the slope of 1 through sample VM 6C does not intersect any other data point, and that the other three data points all lie on a line with the slope of one, parallel to that of VM-6C but with a different Y-intercept. Figure 4.5.(b) shows the same plot with a best-fit line through all the data points. This line has a slope of 1.1 and a Y-intercept of -11.28. From the examination of these two figures it is possible to suggest the following:

1. The plot in figure 4.5(a) indicates that we should reject the hypothesis that the youngest flow (containing VM 6C) belongs to the same magma batch as the others. The two older (and closer in age) flows can not be considered non-comagmatic, since the three analyses plot on the same line.

2. A difference of 0.1 between the slope of the 'expected' line and the best fit line, although it does not seem much, could only be caused by the presence of large modal amounts of magnetite, which constitutes 30-70% of the oxide phase (table 2.7); however, the modal abundance of oxides is about 6% (table 2.1), and that would not be enough to produce such a shift.

3. At any rate, all three flows appear to have crystallized the phases taken into account in the choice of numerators.

4. The youngest flow, represented by sample VM 6C, appears to be the least differentiated of the three.

In light of these considerations, it is reasonable to accept the hypothesis that only two of the three flows can be assumed to be comagmatic, because there is no explanation, in terms of Pearce Element Ratios or in terms of observed mineral phases present in the samples, that would justify a comagmatic hypothesis for all three flows, and at the same time mineral sorting that would produce a slope matching the best fit line of figure 4.5(b).

4.2.3 Residual glass plots.

Using the same element ratios indicated in figure 4.3, and used for the bulk compositions, residual glasses from seven samples were plotted separately. Only Pearce plots for samples VM 6C, XE 05, and VM 01 are shown as representative (fig. 4.6 and 4.7), even though Pearce Element Ratios were calculated for all samples with residual glass analyses (table 2.8). The model slope of 1 was usually plotted through the point with the highest coordinates which corresponds to the more 'primitive' composition. The purpose of studying the Pearce Element Ratios of the residual glasses was to test if it is possible to detect the same crystallization process in chemically different glass patches of the same sample. The only condition for this test to be possible is that phosphorus be conserved. In treating the bulk rock analyses, phosphorus can effectively be considered a conserved element, since, as mentioned before, no apatite could be positively identified in the samples analyzed. At the scale of the residual glass pockets, however, this assumption is a lot less likely. Because of their small size, it is possible that the patches

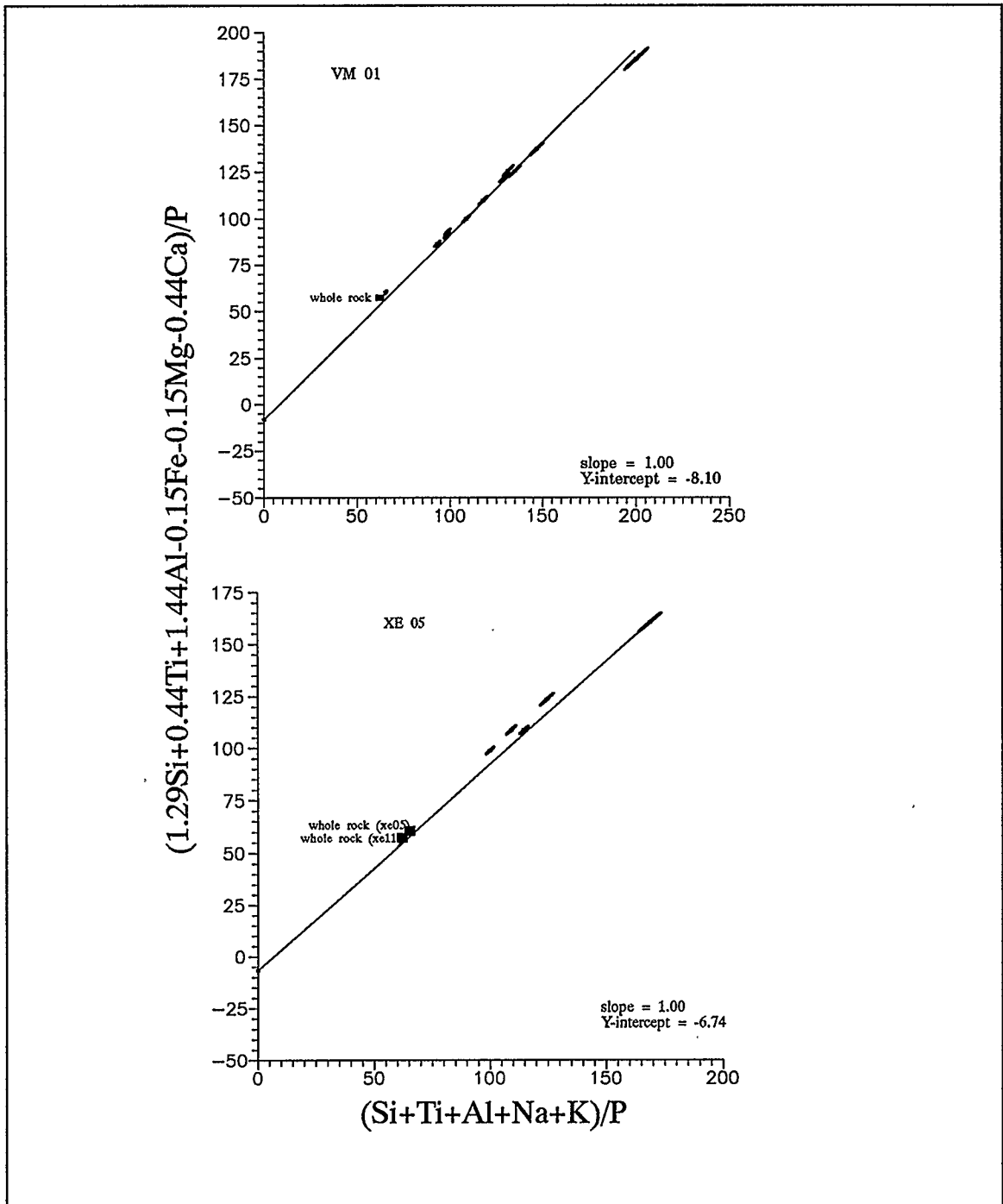


Figure 4.6

Crystal differentiation plots for samples VM 01 and XE 05.

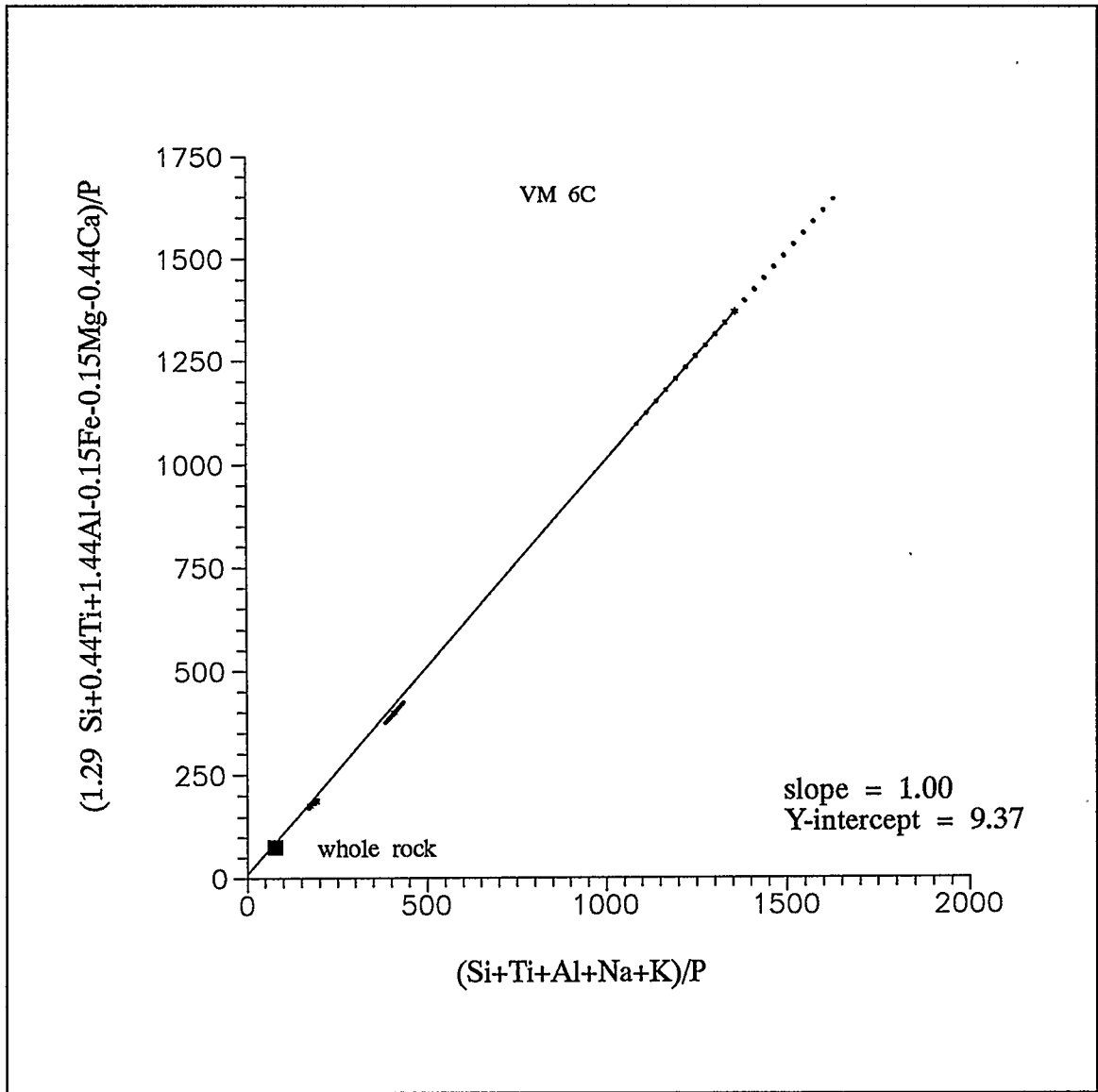


Figure 4.7

Crystal differentiation plot for sample VM 6C.

of residual glass may contain extremely small crystals of apatite that could not be detected by point counting or probing. Samples VM 6C, XE 05, VM 01 were plotted with their respective bulk rock compositions, to check if Pearce plots of the residual glasses are consistent with their parent rock composition. When the denominator is conserved, the bulk rock analyses plot further away from the origin than the residual composition and on the same line as the residua. It is obvious by looking at figures 4.6 and 4.7 that this is not the case, and for this reason, any further testing of hypothesis concerning the fractionation history of these residual glasses would be meaningless because phosphorus is no longer conserved at this stage.

4.1.3. Discussion

Due to the high number of phases in the mineral assemblage and to the non-glassy texture, Pearce Element Ratios of the nephelinites in this study have a more restricted scope than originally anticipated. The purpose of testing hypothesis with Pearce Element Ratios in these samples was to ultimately provide an independent complement to the thermodynamic model of the crystallization processes described in section 5. However, despite the lack of success at the glass patch level, some conclusions can be drawn about the chemistry of the lava flows, on a larger scale. The test for comagmatism shows that two of the three flows cannot be shown as non comagmatic, and that the youngest flow came from a different magma batch than the other two; all three

flows however, are sufficiently similar in chemistry that it is possible to use Pearce Element Ratios to show they crystallized the same phases. In the residual glasses, Pearce Element Ratios cannot provide a useful testing mechanism, because phosphorus is not a conserved element; different testing is then required to explain the crystallization and the chemical differences at this stage.

SECTION 5

INTRODUCTION

Describing igneous processes is the primary task of igneous petrology. The problem in finding an answer to the question "how did these rocks form?" stems from the fact that for multi-component igneous systems there is not a thermodynamic model with a unique solution for any given data set. In general, the more components in the system, the harder it is to develop a model that unequivocally explains all its observed characteristics. Both theoretical and experimental methods implemented to model the crystallization history of volcanic rocks seem to fit well only highly glassy rocks with few isolated phenocrysts, in textural equilibrium with the glass. Nevertheless, it is still possible to provide some guidelines concerning the sequence of crystallization (at least in the phenocryst assemblage), the pressure and temperature conditions, and the source material of rocks with higher degrees of crystallization.

In section four, Pearce Element Ratios were used in the test of two hypotheses: comagmatism in lavas from different flows, and the possibility that bulk rocks and residual compositions are linked by crystal sorting of the mineral phases present. Those tests were intended to provide some independent constraints for the formulation of the thermodynamic model developed in this section. The model consists of two parts: the first, based on

conservation of matter, is an attempt to explain the crystal fractionation histories of the residual glass patches, given the bulk compositions, the residual compositions, and the composition of the mineral phases; a second part, based on conservation laws embodied in the thermodynamic modeling, will provide some constraints on the liquidus temperature, the pressure, and sequence of crystallization. Discussion about depth of origin of the lavas and the implications for their possible parent source composition will conclude the section.

The program CXLFRAC (Stormer and Nicholls, 1978) was used to first determine what mineral phases should be subtracted and in what proportions, from an initial melt (corresponding to the whole rock composition) to produce the various residual glasses. Thermodynamic modeling of fractional crystallization in silicate liquids was done with the program MARK (Nicholls, 1991) which is based on the regular solution model constructed by Ghiorso *et al.* (1983).

5.1 CRYSTALLIZATION HISTORY OF VOLCANO MOUNTAIN LAVAS

5.1.2. Crystal fractionation

The glass patches observed in all samples are obviously the product of extreme fractionation of the original liquid. They are separate from each other and surrounded by or contain different proportions of mineral phases, and thus they can be thought of as small-scale chemical systems, related to each other by fractionation from a common precursor with the bulk composition of the

sample, but at the same time chemically different and spatially unconnected. The variations observed in the chemistry of the glasses can be attributed to this spatial separation, since each glass patch might have interacted differently with its own adjacent mineral phases.

Addition-subtraction calculations (Bowen, 1928) measure the variation of oxide components between rocks, and are used to test possible relations between lava types. These calculations have been performed on sample VM 6C to show the existence of a liquid line of descent between the initial liquid (represented by the bulk composition) and the residual glasses, expressed as a function of subtraction of varying proportions of the mineral phases to produce chemically different residuals. Sample VM 6C was chosen because a rock analysis, analyses of all the constituent phases, and a total modal analysis of the entire rock were available. It must be emphasized that these calculations do not carry any implications on the pressure and temperature conditions of crystallization, but they only offer an estimate of the possible variations in the mineral abundances around the residua upon crystallization, constrained by conservation of matter. The results of the subtraction (mass balance) calculations are reported on table 5.1. They are expressed as grams subtracted from 100 grams of starting material, and therefore they can be compared to the modal abundances.

	oli	pyx	ne	oxi
Glass 1	15.49	47.62	24.48	12.41
Glass 2	14.66	44.21	29.21	11.92
Glass 3	20.55	62.13	0.62	16.70
Glass 4	16.37	50.46	19.99	13.17
Glass 5	14.94	45.47	27.46	12.13

Table 5.1

Results of mass balance subtraction calculations for sample VM 6C. The numbers reported represent grams of phases subtracted from 100 gm. starting material. Compositions of residual glasses are listed on table 2.8. The whole rock composition is reported on table 4.1. Abbreviations: oli: olivine; pyx: pyroxene; ne: nepheline; oxi: oxide.

The total amounts of residual glass predicted by this calculation are between 5 and 10 % in volume (except for the patch labelled "glass 3", for which it is roughly 25%), values considerably higher than the actual modal estimate of 1.7 %. The relative proportions of olivine to pyroxene are higher for the calculated residual than found in the mode of VM 6C. This could be due to an inhomogeneous distribution of phases in the rock; consequently, the modal analysis of the rock may not reflect the abundances of the phases that crystallized to leave the residual glasses. The modal amount of pyroxene in the rock is approximately 66%, but to reach the calculated residual only 40 to 50% crystallization is required. Nepheline is the mineral phase whose modal abundance varies the most between glasses and differs the most from the modal estimate: this might be due to the presence of microlitic nepheline within the glass.

In sample VM 6C it was also possible to examine each glass patch in thin section to see whether the calculated mineral proportions correspond to the phases observed in and around the patch. The calculated results shown in table 5.1 compare well with a visual estimate of the relative abundances of olivine, pyroxene, oxides and nepheline in or around the patches of glass shown below in table 5.1 (a).

	Glass 1	Glass 2	Glass 3	Glass 4	Glass 5
pyx	50	50	65	50	40
oli	10	15	13	20	15
oxi	15	15	20	10	10
ne	25	20	2	20	35

Table 5.1(a)

Estimated modal distribution of mineral phases near the residual glasses of sample VM 6C.

In summary, the glass patches can be said to represent residua from a fractionation process with little or no interaction between crystals and melt. For these patches it is possible to demonstrate that each is the result of fractionation along a different liquid line of descent because the calculated amounts of phases subtracted from melt composition to obtain the glasses are not similar to those estimated by modal analysis of the melt and they vary for each patch. The estimated modal amounts in the immediate neighborhood of the residual glasses agree more with the calculated amounts, because the overall distribution of the minerals in the sample is inhomogeneous.

5.1.3 Liquid lines of descent

Part of the chemical variation along liquid lines of descent was modeled with MARK (Nicholls, 1991) for an initial bulk composition corresponding to that of sample VM 01 are shown on figure 5.1; also plotted in the diagram are the compositions of residual glasses from all the samples. The range in the liquid lines of descent of the other samples for which a bulk composition was available is given by the shaded areas. These curves represent the earliest stages of crystallization. The curves were calculated at 3.3 and 10 kilobars to show the effect of pressure. At 10 kilobars the fractionation curve is closer to the compositional field of the residual glasses. The position of the residual glasses with respect to the starting liquid composition is usually explained assuming a bend in the liquid line of descent caused by the later crystallization of oxides (see for example, Carmichael, 1964): this bend is outlined in figure 5.2, together with the trend in variation for the Thingmuli and Skaergaard (Wager and Brown, 1960) suites. It is however possible that in the case of the Volcano Mountain nephelinites, polybaric fractionation (discussed below in section 5.1.4) could have contributed to a shift in the liquid line of descent before oxide crystallization occurred.

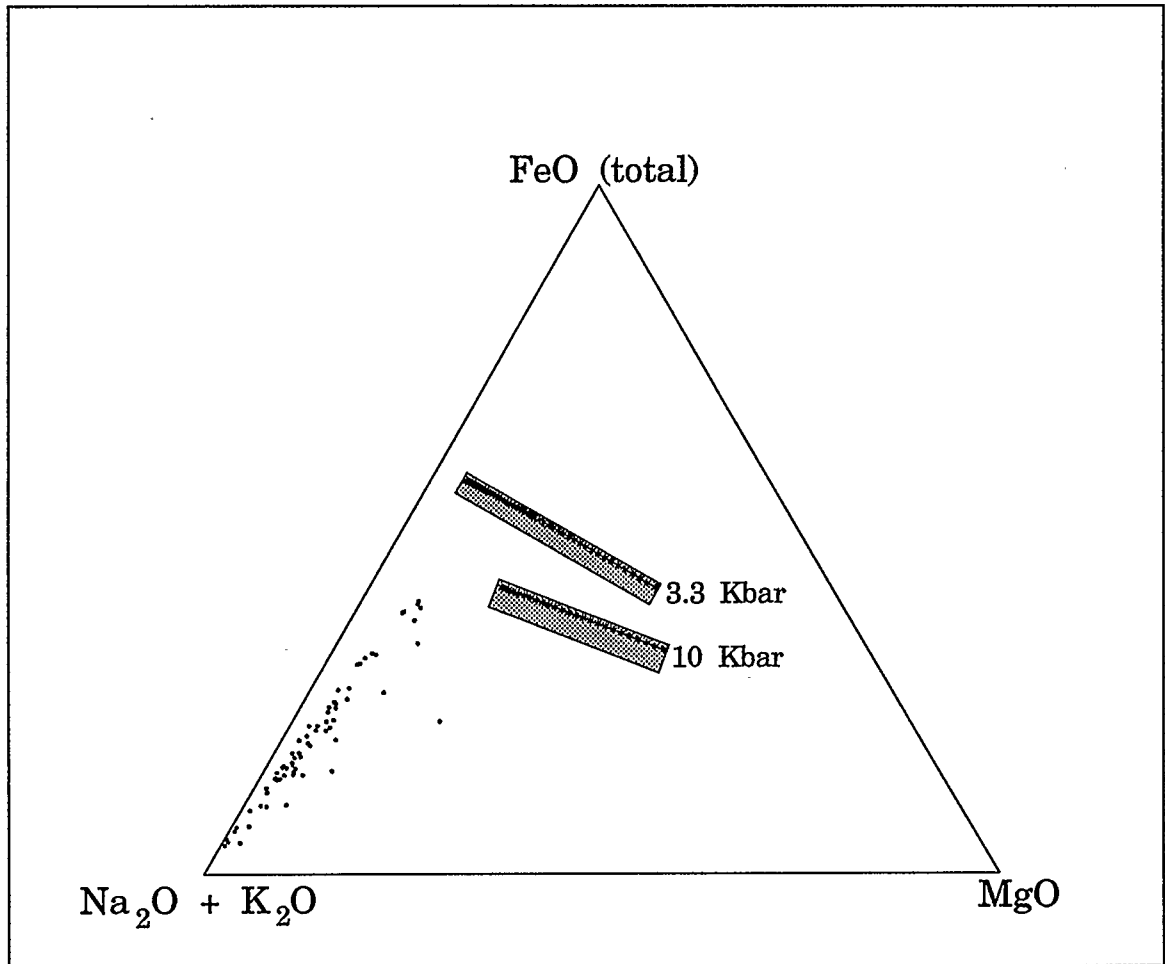


Figure 5.1

Liquid lines of descent modeled with the program MARK (Nicholls, 1991). The curves represent fractionation curves with an initial composition equal to that of sample VM 01. The shaded areas represent the range in liquid lines of descent obtained by using the other samples as starting compositions. The points are compositions of all the residual glasses analyzed (table 2.8).

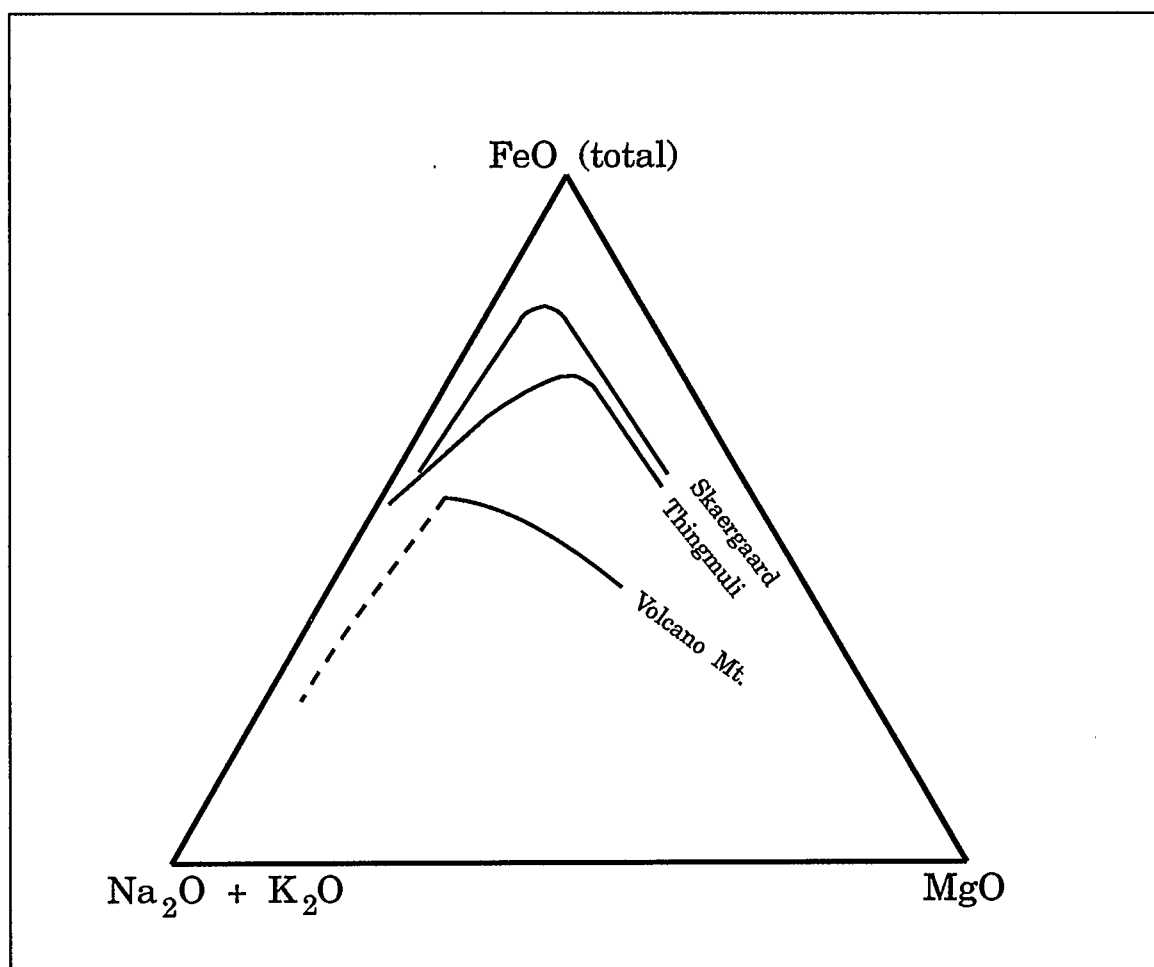


Figure 5.2

Variation diagram of total alkali ($\text{Na}_2\text{O} + \text{K}_2\text{O}$), total iron ($0.899\text{Fe}_2\text{O}_3 + \text{FeO}$), and magnesium, showing the fractionation trend for the Skaergaard (Wager and Brown, 1960) and the Thingmuli (Carmichael, 1964) suites. Also shown in this diagram is an analogous variation trend proposed for the Volcano Mountain nephelinites.

5.1.4. P-T paths.

Thermodynamic modeling of silicate melts was used to constrain the pressure-temperature path of crystallization. Assuming that the rock compositions correspond to the compositions of the original liquid, fractionation paths can be calculated for different boundary conditions. The paths that produce the observed mineral assemblage are possible paths for the melts.

Figure 5.3 shows two curves in a P-T diagram that constrain the pressure and temperature path, for the crystallization of the phenocryst phases. The curve on the right represents an isenthalpic decompression and cooling path, from 10 kilobar to ambient pressure. The shaded area represents the region where the same curve plots for the other samples. Olivine is the only phase that crystallizes during decompression, according to this model. Because clinopyroxene occurs as microphenocrysts, the path followed by the melt during crystallization could not have been perfectly isenthalpic. Varying the starting pressure between 8 and 15 kilobars does not shift the position of the isenthalpic curve, nor does it introduce pyroxene as part of the phenocryst assemblage in the calculations. The curve on the left was constructed by joining P-T points on isobaric fractionation paths where crystallization of olivine is joined by a second phase. The dashed line represents the pressure (3.3 kbar) below which which plagioclase is the first phase to crystallize, rather than clinopyroxene. Below this pressure, the curve marks a P-T path where

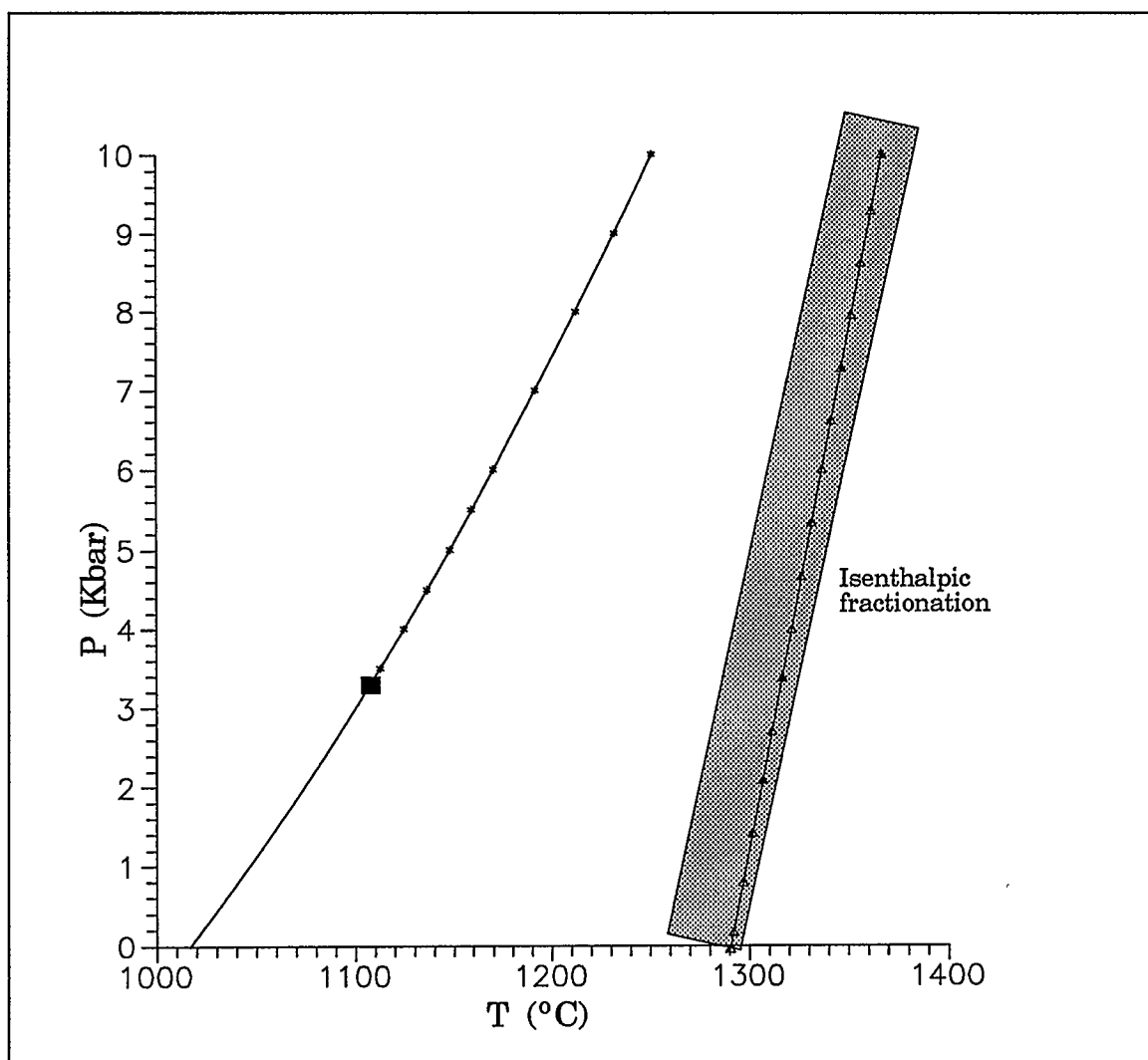


Figure 5.3

P-T curves constraining the crystallization path of Volcano Mountain nephelinites. The curve on the right represents isenthalpic cooling and decompression of sample VM 01; the shaded area is the region where the analogous curves plot for the other samples. The curve on the left was constructed by joining pressure and temperature points of isobaric fractionation paths where olivine is joined by a second phase. The solid square represents the boundary pressure below which plagioclase rather than pyroxene is the second phase to crystallize in this type of path.

plagioclase crystallizes after olivine. This point constrains the P-T path the lava must have followed, because no plagioclase is present in the phenocryst assemblage or in the groundmass. The temperature range of the fractionation path is taken to be between 1300 and 1100°C.

Figure 5.4 shows the compositions of the olivine phenocrysts expected under the isobaric fractionation model, expressed as mole fraction of forsterite in sample VM 01. The expected and the observed values are compared for samples VM 01, VM 6C and VM 2C and are shown on table 5.2; the temperature range of the calculated values was that estimated for the fractionation path (between 1300 and 1100°C). Rim compositions can be compared to low P-T values, and core compositions to the high P-T values.

VM 01 (C)	86.9
VM 01 (G)	83.8
VM 2C (C)	79.7
VM 2C (R)	77.6
VM 6C (C)	82.9
VM 6C (R)	75.6
calc. @ 1100°C	84.5-85.2
calc. @ 1300°C	88.1-88.5

Table 5.2

Mole fraction of forsterite in three nephelinites from Volcano Mountain, and calculated values for sample VM 01 using the curves in figure 5.4. The range in composition is given for pressures between 3.3 (left) and 10 (right) kilobars. C: core, G: groundmass, R: rim.

Differences between the observed and the expected values are more noticeable in sample VM 6C and VM 2C, perhaps because differences in bulk composition might affect the composition obtained with modeling. The difference between

calculated and observed values in the core of VM 01 seems to be less than that of its groundmass composition. Some of the discrepancies in this comparison can be attributed to the fact that the values reported for the cores of olivine phenocrysts might not represent the true center of the grain, depending on its orientation in the thin section slice. As for the groundmass and rim compositions, they could well represent a much later stage in the cooling process.

The composition of clinopyroxene (X_{Di}) obtained with the isobaric modeling does not seem to match the observed values of the samples; table 5.3 shows how some of the observed X_{Di} values compare with those obtained in the thermodynamic calculations as the first appearance of clinopyroxene in isobaric fractionation (figure 5.3).

VM 01	96.7
VM 01	98.8
VM 2C	96.8
VM 2C	94.2
VM 6C	97.1
VM 6C	95.5
calc. @ 3.3 kbar	82.4
calc. @ 10 kbar	84.7

Table 5.3

Observed and calculated pyroxene compositions in terms of mole fraction of diopside. The whole rock analysis used to obtain the calculated values was VM 01. The temperature of first appearance of pyroxene is 1107.9°C for 3.3 kbars and 1251°C for 10 kbars.

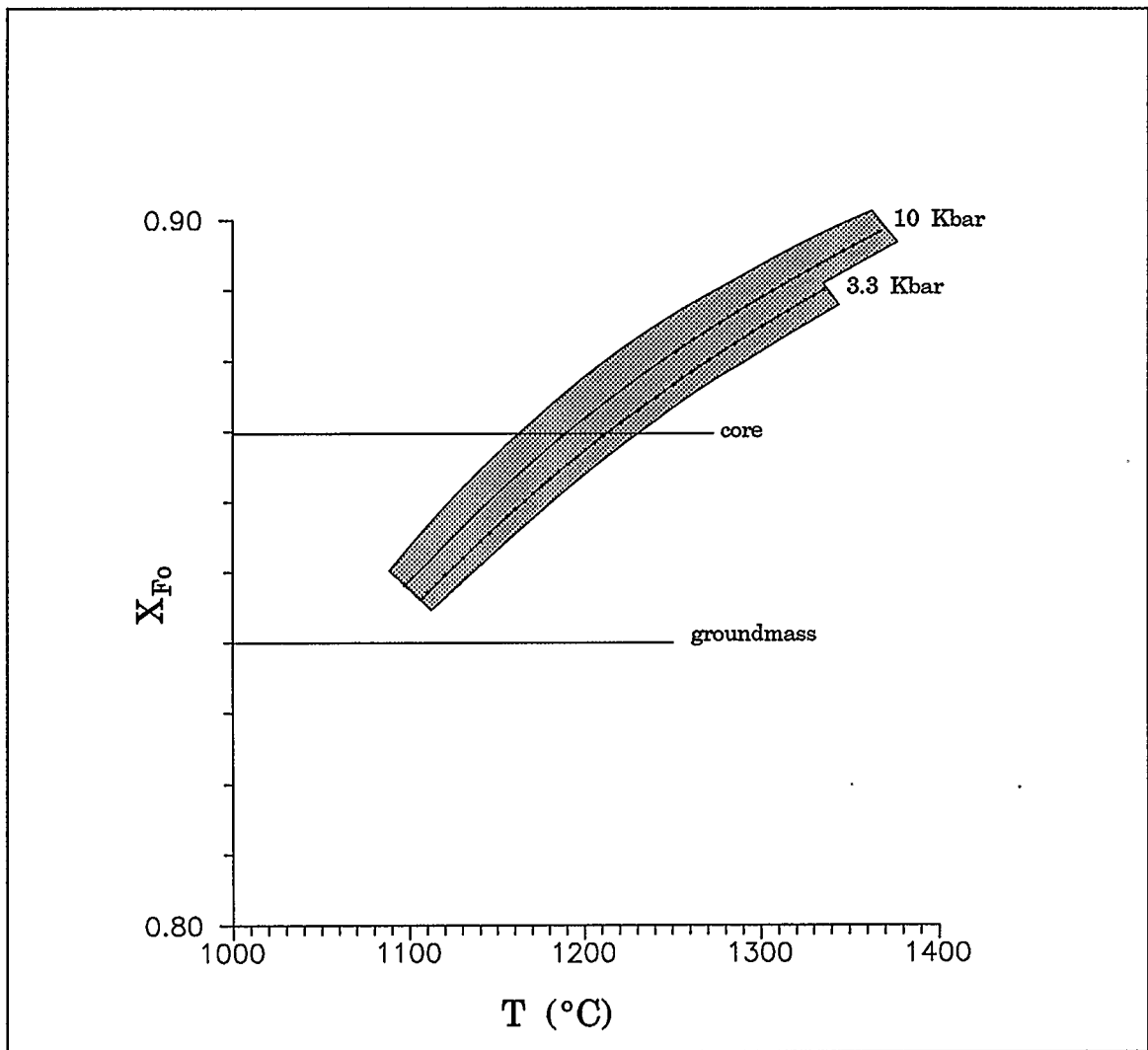


Figure 5.4

Expected compositions of olivine phenocrysts, expressed as mole fraction of forsterite, modeled for sample VM 01. Shaded areas indicate the region where the same curves plot for the other samples. The lines labeled "core" and "groundmass" represent the actual composition of the olivine in VM 01.

The calculated pyroxene compositions are very different from the observed values. Such discrepancy can be explained by the choice of solution model for clinopyroxene (Ghiorso *et al.*, 1983), which is confined to components in the quadrilateral and does not account for other elements such as Ti, Al, Na in the solid solution. In the nephelinites, the pyroxene phenocrysts are very small compared to the olivine phenocrysts, suggesting that fractionation could have happened throughout the ascent of the magma under conditions close to isenthalpic. Rapidly decreasing pressure would not allow clinopyroxene to crystallize large phenocrysts. If crystallization had occurred under isobaric conditions, there would be some indication of it in the larger size of the clinopyroxene phenocrysts, or in their composition. This interpretation for the compositional difference in the pyroxenes, supported by textural evidence, would then imply that fractionation occurred under polybaric conditions. In this case, the calculated pyroxene compositions shown in table 5.3 are not a valid comparison with the observed values.

An independent estimate of crystallization depth was obtained by plotting the CIPW normative composition on the ternary diagram by Sack *et al.* (1987), shown in figure 5.5. The low pressure cotectic shown in this diagram is well constrained by experimental data and it is defined for alkaline lavas saturated with plagioclase, crystallizing at one bar and under equilibrium crystallization conditions. The other cotectic curve was derived from published high pressure studies on crystallization of alkaline lavas and is not as well

constrained as the one at ambient pressure. According to Sack *et al.* (1987), rocks with crystallization pressures higher than 8 kilobars should show a distinct signature in the diagram depicted in figure 5.5, by plotting on or below the cotectic curve labeled "8 kbar".

From the closer proximity of the samples to the low pressure cotectic, the pressure of crystallization would seem closer to 1 bar than 8 kilobars, although it is not possible to give an exact quantitative estimate of their crystallization pressure by using this diagram alone. In combination with the P-T path constraints discussed earlier, however, 8 kilobars could be taken as the starting pressure of crystallization. If polybaric fractionation was in fact the process of crystallization, then it is possible that the melt started crystallizing around 8 kilobars and 1300°C, and continued crystallization through its ascent. This would be consistent with the smaller size of the clinopyroxene phenocrysts, and more generally with the smaller grain size of the groundmass, and paucity of glass.

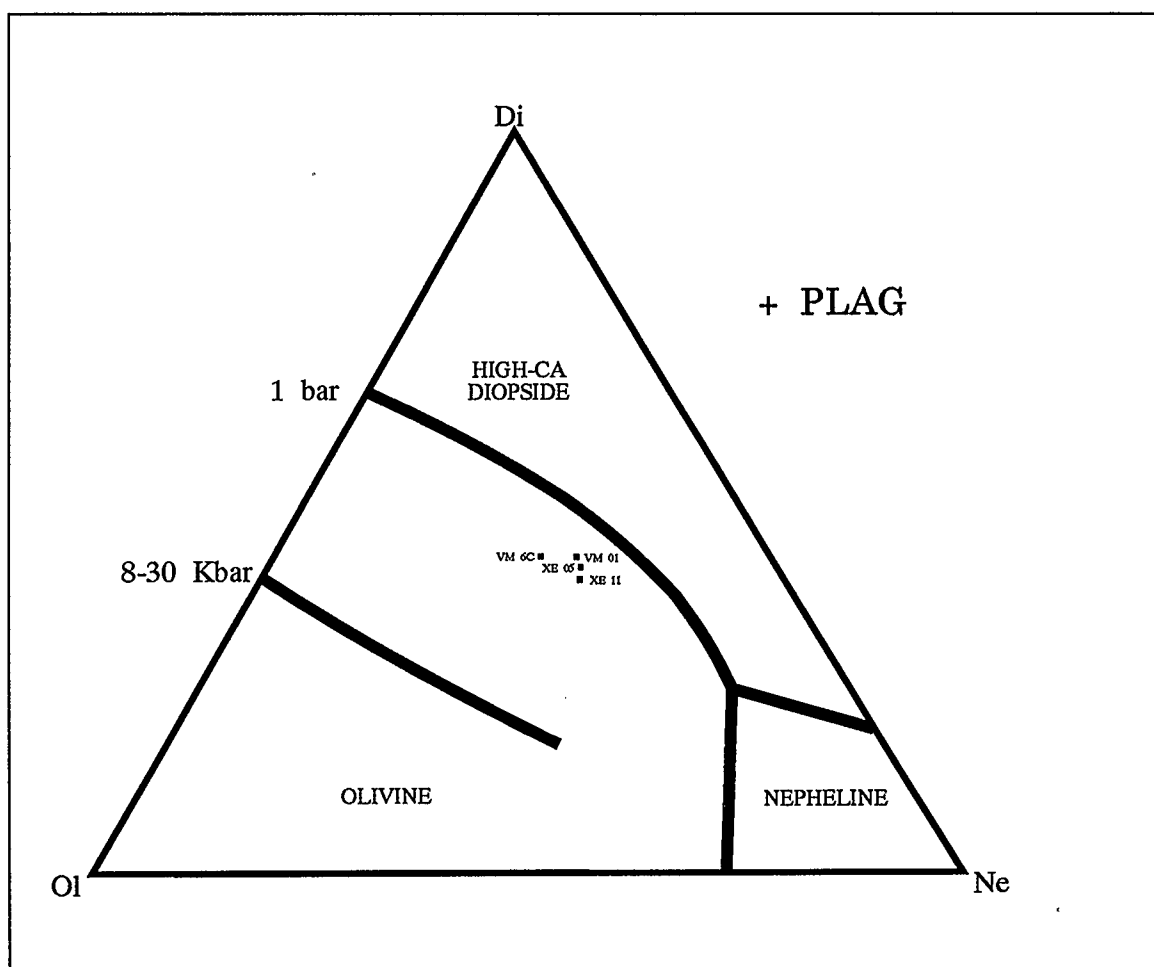


Figure 5.5

Olivine + high calcium pyroxene + plagioclase cotectic for melts at one atmosphere or 8-30 kbars (after Sack *et al.*, 1987). End members (ol, ne, di) correspond to projections of normative compositions saturated with plagioclase.

5.2 DEPTH OF MELT SEPARATION

Thermodynamic modeling of silicate melts can be used to calculate the activity of silica in the melt; this in turn can be used to estimate the depth of equilibration of basic magmas with an anhydrous mantle containing olivine and pyroxene. The petrogenetic grid constructed by Ghiorso and Carmichael (1989) is shown on fig 5.6 and consists of a temperature versus activity of silica in the melt diagram with superimposed isobars for the $Fo + SiO_2(melt) \Rightarrow En$ equilibrium. The assumptions made in this estimate are that after separation of the melt, the residuum will still contain some orthopyroxene, and that the activity of silica in the melt of isochemical systems is only a function of temperature, not pressure (Ghiorso and Carmichael, 1989). If these assumptions are correct, then given the temperature range estimated for the nephelinites in this study, it is possible to obtain a range in activity of silica in the melt and thus a range in pressure. This range is illustrated on figure 5.6, and it was found to be between 15 and 25 kilobars, corresponding approximately to a depth of 45 to 75 kilometers. The depth of melt separation obtained in this case must be considered a minimum. Because of the uncommon bulk composition of these rocks, one cannot rule out a residuum consisting only of olivine, rather than both olivine and orthopyroxene.

The minimum depth of melt separation can further be constrained by the pressure estimates for the ultramafic nodules. The range in depth given by

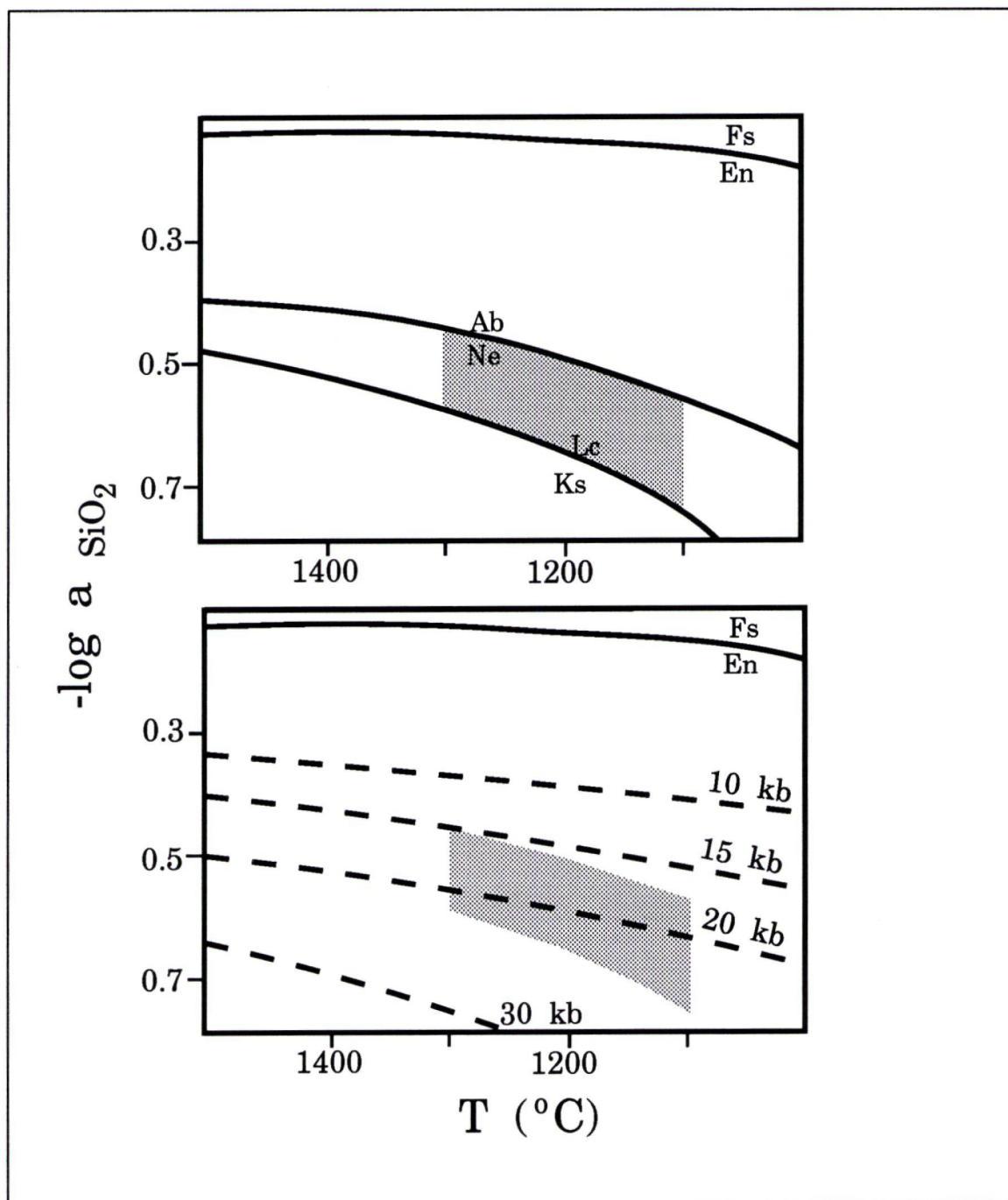


Figure 5.6

Log a_{SiO_2} versus temperature diagrams (after Ghiorso and Carmichael, 1990). The top diagram shows the two buffer reactions (at 1 bar) constraining the activity of silica in the melt: the presence of leucite and nepheline in the samples brackets the activity of silica as shown. The temperature range is constrained by the P-T paths. The bottom diagram illustrates the position of the En-Fo buffer at a minimum pressure between 15 and 25 kbar.

thermobarometry of the xenoliths within the lavas is between 60 and 135 kilometers: clearly, this eliminates the possibility that the lavas originated at different pressures and the pressure range of the nephelinites, given the range in silica activity.

This consideration brings up another important point concerning the relationship between the xenoliths and their host lavas. It seems that there is some overlap in the estimated depths of origin of the lavas and of the xenoliths, which would indicate the possibility that the xenoliths may represent pieces of the refractory residuum, or of an area of the mantle very close to it. This hypothesis can be tested by using a variation of the addition-subtraction calculations described in section 5.2. The starting composition was taken as that of an average pyrolite (Green and Ringwood, 1967; Stout and Nicholls, 1977) from which the rock composition was subtracted. With this method however, it was not possible to find a liquid line of descent which would yield a residuum comparable in composition to any of the xenoliths. This means that the nephelinites came from partial melting of a different mantle composition, perhaps more uniform than the compositional range exhibited by the xenoliths and which might have contained CO₂-rich fluids (which would explain the presence of calcite). In any case, the assumption that the xenoliths carried within the lavas are from the same part of the mantle as the source rocks for the lavas cannot be supported.

SECTION 6

6.1 CONCLUSIONS

The lavas from Volcano Mountain are one of the few reported occurrences of Recent nephelinites in the Canadian Cordillera. These lava flows contain exclusively olivine and pyroxene in the phenocryst assemblage, microlitic nepheline and leucite in the groundmass. Their crystallization was estimated to have started between 1300 and 1100°C, at a pressure between 3.3 and 10 kilobars. Most of the mineral phases must have crystallized prior to extrusion, as the glass is very sporadic and restricted to micron-size pockets.

Modeling crystal fractionation paths using mass-balance subtraction calculations shows that different liquid lines of descent can exist for the same bulk composition, if different amounts of the same mineral phases are subtracted, and that the residual glasses can be thought of as a product of this type of fractionation.

The minimum depth for the magma source was estimated to be at 60 km.

The Volcano Mountain nephelinites are host to ultramafic xenoliths, mostly dunites, whose temperature and pressure of origin have been estimated by geothermobarometry to be 930-1350°C and 20-45 kilobars. These values would suggest an overlap between the source rock depth of the nephelinites and the mantle level of the xenoliths. Mass balance calculations however, show

that the xenoliths cannot be considered to be the residuum from separation of a liquid of nephelinitic composition.

Nephelinites are usually associated in continental settings with carbonatites, and they are found in or near rift zones, although some examples from South Africa are found in tectonically inactive settings (Best, 1982). It does not appear that carbonatites exist in the area near Volcano Mountain, and there is no evidence for the presence of an incipient rift. More detailed work needs to be done on the many Recent cinder cones in central Yukon, before conclusions can be drawn on the tectonic association of the rocks studied.

REFERENCES CITED

Armstrong, 1988, Mesozoic and Cenozoic magmatic evolution of the Canadian Cordillera, Geological Society of America Special Paper 218, p. 55-91.

Bence, A.E., and Albee, A.L., 1968, Empirical correction factors for the electron microanalysis of silicates and oxides, *Journal of Geology*, **76**, p. 382-403.

Berman, R.G., 1988, Internally consistent thermodynamic data for minerals in the system $\text{Na}_2\text{O}-\text{K}_2\text{O}-\text{CaO}-\text{MgO}-\text{FeO}-\text{Fe}_2\text{O}_3-\text{Al}_2\text{O}_3-\text{SiO}_2-\text{TiO}_2-\text{H}_2\text{O}-\text{CO}_2$, *Journal of Petrology*, **29**, no.2, p. 445-522.

Bostock, H.S., 1936, Carmacks District, Yukon, Geological Survey of Canada Memoir 189, 65 p.

Bowen, N.L., 1928, *The Evolution of the Igneous Rocks*, Princeton University Press, 332 p.

Brearley, M., Fujii, T., and Scarfe, C.M., 1982, The petrology and geochemistry of ultramafic nodules From Summit Lake, Prince George British Columbia, *in*: GAC-MAC joint annual meeting Program with abstracts, p.40.

Buddington, A.F., and Lindsley, D.H., 1964, Iron-Titanium Oxide Minerals and Synthetic Equivalents, *Journal of Petrology*, 5, no. 2, p. 310-357.

Carmichael, I.S.E., 1964, The Petrology of Thingmuli, a Tertiary volcano in eastern Iceland, *Journal of Petrology*, 5, no.2, p. 435-460.

Cebria-Gomez, J.M., 1990, PX: a program for pyroxene classification and calculation of end members, *American Mineralogist*, 75, p. 1426-1427.

Deer, W.A., Howie, R.A. and Zussman, J., 1966, *An Introduction to the Rock-Forming Minerals*, Longman, 528 p.

Donnay, G., 1957, Synthetic nephelines, Carnegie Institution of Washington, Annual Report Dir. Geophysical Laboratory, 1956-7, p. 237-250.

Fiesinger, D.W., 1975, Petrology of the Quaternary volcanic centers in the Quesnel Highlands and the Garibaldi Provincial Park areas, British Columbia, Unpubl. PhD. Thesis, University of Calgary.

Fowler, A.D., 1990, Rock alteration: a further application of Pearce diagrams and related techniques, *in*: Theory and application of Pearce Element Ratios to Geochemical Data Analysis, Geological Association of Canada Short Course vol. 8, J.K. Russell and C.R. Stanley editors.

Fudali, R.F., 1963, Experimental studies bearing on the origin of pseudoleucite and associated problems of alkalic rock systems, Geol. Soc. Am. Bulletin, 74 p. 1101-1126.

Fujii, T. and Scarfe, C.M., 1982, Petrology of ultramafic nodules from West Kettle River, Southern British Columbia, *Contrib. Mineral. Petrol.*, **80**, p. 297-306.

Ghiorso, M.S., Carmichael, I.S.E., Rivers, M.L., Sack, R.O., 1983, The Gibbs Free Energy of mixing of natural silicate liquids: an expanded regular solution approximation for the calculation of magmatic intensive variables, *Contrib. Mineral. Petrol.* **84**, p. 107-145.

-----, and Carmichael, I.S.E., 1989, Modeling magmatic systems: petrologic applications, *in*: Thermodynamic modeling of geological materials: minerals, fluids and melts, Mineralogical Society of America Reviews in Mineralogy, I.S.E. Carmichael and H.P. Eugster editors, p. 467-497.

-----, and Carmichael, I.S.E., 1980, A FORTRAN IV computer program for evaluating temperatures and oxygen fugacity from the composition of iron-titanium oxides, *Computers and Geosciences*, **7**, p.123-129.

Green, D.H., and Ringwood, A.E., 1967, The genesis of basaltic magmas, Contrib. Mineral. Petrol. 15, p.103-190.

Hahn, T., and Buerger, M.J., 1955, The detailed structure of nepheline, Zeit Kristallographie, 106, p.308-320.

Herzberg, C.T., 1978, Pyroxene geothermometry and geobarometry: experimental and thermodynamic evaluation of some subsolidus phase relations involving pyroxenes in the system CaO-MgO-Al₂O₃-SiO₂, Geochemica et Cosmochemica Acta, 42, p. 945-957.

Irvine, T.N., and Baragar W.R.A., 1971, A guide to the chemical classification of the common volcanic rocks, Canadian Journal of Earth sciences, 8, p. 523-548.

Jackson, L.E., and Stevens, W., 1992, A recent eruptive history of Volcano Mountain, Yukon Territory, Geological Survey of Canada Current Research 92-1A, p. 33-39.

Lindsley, D.H., 1983, Pyroxene thermometry, *American Mineralogist*, 68, p. 477- 493.

-----, and Andersen, D.J., 1983, A two-pyroxene thermometer, Proceedings of the thirteenth Lunar and Planetary Conference, Part 2, *Journal of Geophysical Research*, 88, Supplement, A887-A906.

MacDonald , G.A., and Katsura, T., 1970, Chemical Composition of Hawaiian lavas, *Journal of Petrology*, 5, no.1, p. 82-133.

Mac Gregor, I.D., 1967, Mineralogy of model mantle compositions, *in* Ultramafic and related rocks, P.J. Wyllie editor, John Wiley and Sons, 464 p.

Meyer, S.L., 1975, Data analysis for scientists and engineers, John Wiley and Sons, 513 p.

Mori, T., 1977, Geothermometry of spinel lherzolites, *Contrib. Mineral. Petrol.*, **59**, p.261-279.

Morimoto, N., 1989, Nomenclature of pyroxenes, *Canadian Mineralogist*, **27**, p.143-156.

Nicholls, J., 1990, Principles of thermodynamic modeling of igneous processes, *in: Modern methods of Igneous Petrology: understanding magmatic processes*, J.Nicholls and K. Russell eds., Mineralogical Society of America *Reviews in Mineralogy* **24**, p. 1-23.

-----, 1990, Stoichiometric constraints on variations in Pearce Element Ratios and analytical uncertainty in hypothesis testing, *in: Theory and application of Pearce Element Ratios to Geochemical Data Analysis*, Geological Association of Canada Short Course vol. 8, J.K. Russell and C.R. Stanley editors.

-----, 1977, The Calculation of Mineral Compositions and Modes of Olivine-Two Pyroxene-Spinel Assemblages, *Contrib. Mineral. Petrol.*, **60**, p.119-142.

-----, and Stout, M.Z., 1988, Picritic melts in Kilauea: evidence from 1967-1968 Halemaumau and Hiiaka eruptions, *Journal of Petrology*, **29**, p. 1031-1057.

-----, and Stout, M.Z., 1986, Electron beam analytical instruments and the determination of modes, spatial variations of minerals and textural features of rocks in polished thin sections, *Contrib. Mineral. Petrol.*, **94**, p.395-404.

-----, Fiesinger, D.W. and Ethier, V.G, 1977, FORTRAN IV programs for processing routine electron microprobe data, *Computers and Geoscience*, **3**, p.49-83.

-----, Stout, M.Z., and Fiesinger, D.W., 1982, Petrologic variations in Quaternary Volcanic Rocks, British Columbia, and the nature of the Underlying Upper Mantle, *Contrib. Mineral. Petrol.*, **79**, p. 201-218.

Ross, J.V., 1983, The nature and rheology of the Cordilleran Upper Mantle of British Columbia: inferences from peridotite xenoliths, *Tectonophysics*, **100**, p.321-357.

Russell, J.K., and Halleran, A.D., 1990, Trace elements formulated as Pearce Element Ratios (PER) I: insights into magmatic differentiation, *in*: Theory and application of Pearce Element Ratios to Geochemical Data Analysis, Geological Association of Canada Short Course vol. 8, J.K. Russell and C.R. Stanley editors.

-----, and Nicholls, J., 1988, Analysis of petrologic hypothesis with Pearce Element Ratios, *Contrib. Mineral. Petrol.*, **99**, p. 25-35.

Sack, R.O., Walker, D., and Carmichael, I.S.E., 1987, Experimental petrology of alkalic lavas: constraints on cotectics of multiple saturation in natural basic liquids, *Contrib. Mineral. Petrol.*, **96**, p. 1-23.

Simkin, T., and Smith, J.V., 1966, Minor element distribution in olivine, Geological Society of America Special Paper 101, p.203.

Sinclair, P.D., Tempelman-Kluit, D.J., and Medaris, L.G. Jr., 1977, Lherzolite nodules from a Pleistocene cinder cone in central Yukon, Can. Jour. Earth Sciences, 15, p. 220-226.

Stanley, C.R., and Russell, J.K., 1989, Petrologic hypothesis testing with Pearce element ratio diagrams: derivation of diagram axes, Contrib. Mineral. Petrol., 103, p.78-89.

Stormer, and Nicholls J., 1978, XLFRAC: a program for the interactive testing of magmatic differentiation models, Computers and Geosciences, 4, p.143-159.

Stout, M.Z., and Nicholls, J., 1977, Mineralogy and petrology of Quaternary lavas from the Snake River Plain, Idaho, *Can. Jour. Earth Sciences*, **14**, p. 2140-2156.

Ulmer, G.C., Grandstaff, D.E., Weiss, D., Moats, M.A., Buntin, T.J., Gold, D.P., Hatton, C.J., Kadik, A., Koseluk, R.A., Rosenhauer, M., 1987, The mantle redox state: an unfinished story?, *in*: Mantle metasomatism and alkaline magmatism, Geological Society of America Special Paper 215, E.M. Morris and J.D. Pasteris editors, p. 5-21.

Wager, L.R., Brown, G.M., and Wadsworth, 1960, Types of igneous cumulates, *Journal of Petrology*, **1**, p. 73-85.

Wells, P.R.A., 1977, Pyroxene thermometry in simple and complex systems, *Contr. Mineral. Petrol.*, **62**, p. 129-139.

Wilshire, H.G., Meyer, C.E., Nakata, J.K., Calk, L.C., Shervais, J.W., Nielson, J.E., Schwartzman, E.C., 1988, Mafic and ultramafic xenoliths from

volcanic rocks of the Western United States, U.S. Geological Survey Professional Paper, **P1443**, 179 p.

Wyllie, P.J., 1984, Sources of granitoid magmas at convergent plate boundaries, *Physics of the Earth and Planetary Interiors*, **35**, p. 12-18.

APPENDIX A

Formula for detection limits on microprobe data.

$$DL = \frac{3 (BG * t)^{1/2}}{t} * FACT$$

where:

DL = Detection Limit

BG = Background (counts/second)

t = counting time

FACT = oxide factor

Detection limits for mineral phases in this study

CaO	TiO₂	Al₂O₃	Cr₂O₃	NaO
0.01	0.02	0.04	0.03	0.03
SiO₂	FeO	MgO	P₂O₅	K₂O
0.09	0.04	0.02	0.02	0.02